THE UNIVERSITY OF CHICAGO

SEARCH FOR NEW PHENOMENA IN DIJET TOPOLOGIES FROM PROTON-PROTON COLLISIONS AT $\sqrt{S} = 13$ TEV

A DISSERTATION SUBMITTED TO
THE FACULTY OF THE DIVISION OF THE PHYSICAL SCIENCES
IN CANDIDACY FOR THE DEGREE OF
DOCTOR OF PHILOSOPHY

DEPARTMENT OF PHYSICS

BY

JEFFREY ROGERS DANDOY

CHICAGO, ILLINOIS

DECEMBER 2016

For my family

TABLE OF CONTENTS

LIST OF FIGURES

LIST OF TABLES

ABSTRACT

A search for non-standard-model resonance signals decaying into pairs of jets is presented. The search is performed with the ATLAS experiment using 3.6 fb^{-1} of proton-proton collision data at a center-of-mass energy of 13 TeV from the Large Hadron Collider. The calibration and performance validation of high-p_{T} jets are explored. Local excesses in the invariant mass spectrum of jet pairs are studied for compatibility with a data-driven background estimate. No evidence of anomalous excesses are found within a mass range of 1.1 to 6.9 TeV. Lower mass limits are set at a 95% credibility-level on the production of excited quarks below 5.2 TeV, heavy W' bosons below 2.6 TeV, and quantum black holes below 8.3 (5.3) TeV for six (one) extra-dimensional models. Limits are also set on the production of a dark matter mediator Z' for various values of the standard model coupling and on model-independent generic resonance forms.

CHAPTER 1
INTRODUCTION

A search for new physics is presented using data produced by proton-proton collisions at a center-of-mass energy of 13 TeV at the Large Hadron Collider (LHC) [1] and recorded by the ATLAS detector [2]. The standard model (SM) encompasses our current understanding of elementary particle physics, but theoretical inconsistencies point to new physics beyond the standard model (BSM). Potential BSM physics may be produced by the interactions of quarks and gluons within the colliding protons. This thesis presents a search for new BSM resonances with large invariant masses that decay into dijet systems [3].

Previous searches in dijet distributions from lower-energy proton-proton collisions at the SPS [4–6], Tevatron [7, 8], and LHC [9–17] found no evidence of BSM physics. However the cross section for generating any massive BSM particles increases greatly with the center-of-mass energy of the colliding protons, as can be seen in the production cross section ratio between 13 TeV and 8 TeV in Figure 1.1. Any BSM physics that couples to gluons is particularly sensitive to this enhancement, with a 10-fold increase in cross section for hypothetical particles with a mass of $\sim$2 TeV. Searches involving dijet distributions are therefore among the most important early searches when a new energy frontier is reached by a hadron collider.

This thesis describes the first search for BSM physics at 13 TeV using the ATLAS detector. Our current understanding of QCD dijet production and the motivation for several BSM physics models is presented in Chapter 2. The LHC experiment and the ATLAS detector are described in Chapter 3. The Monte Carlo (MC) simulation, detailed in Chapter 4, provides a theoretical prediction of QCD background processes and BSM physics signals. Details on jet reconstruction and performance at 13 TeV are given in Chapter 5. The analysis event selection and comparisons with MC simulation predictions are presented in Chapter 6, while analysis strategies including background estimation, search strategies, and limit setting are detailed in Chapter 7. The search results and limits set on BSM physics models are presented in Chapter 8 alongside the conclusion of these studies.

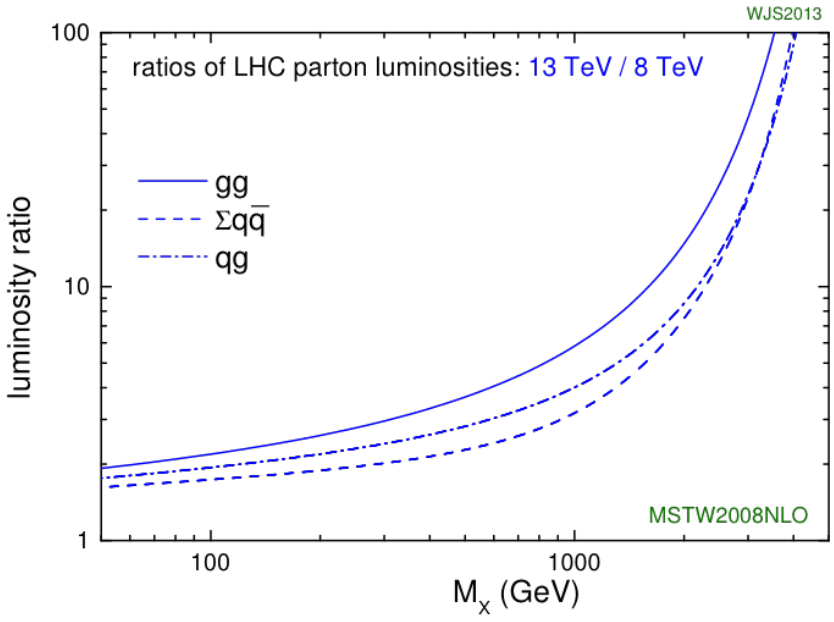

(a)

Figure 1.1: The predicted increase in production cross section of potential BSM resonances between 13 TeV and 8 TeV. New physics is modeled by the MSTW2008NLO Monte Carlo generator, and presented as a function of potential resonance mass M_X for gg, $q\bar{q}$, and qg processes. Plot from W.J. Stirling [private communication].

CHAPTER 2
THE STANDARD MODEL

The standard model (SM) is the most comprehensive theory of particle physics today. It encompasses all of our current knowledge of basic particles and their interactions into a single, concise model, represented by Figure 2.1. Two distinct classes of particles, quarks and leptons, form the basis of all visible matter in the Universe. A third class of elementary particles, gauge bosons, convey the fundamental interactions between particles and are referred to as force carriers. Particles are grouped according to their quantum attributes and interactions through the strong, electroweak, and gravitational forces. The SM has been uniquely successful in predicting and explaining experimental results up to the present day.

The search presented in this thesis focuses on the strong interaction. The strong force interacts with quarks via gluon bosons and is responsible for binding quarks into composite hadrons and mesons. Quarks and gluons, collectively referred to as partons, have a unique attribute called color charge which dictates their interaction through the strong force. Color charge occurs in three flavors labeled red, green and blue. Each flavor may be positive or negative.

The interplay between the three color charges leads to the unique characteristic that the strong force does not weaken with increasing distance. As a consequence quarks interact via the strong force at a short range limited to femtometers and cannot typically separate from one another, an effect called color confinement. Attempts to energetically separate two particles interacting via the strong force will instead pair-produce two new particles that will each strongly interact with one of the original particles. At smaller distances or higher energies the strong force becomes asymptotically weaker to the point that two partons are barely interacting, a phenomenon known as asymptotic freedom. These unique properties of the strong force lead to remarkable interactions between partons that are of great interest at hadron colliders.

2.1 Quantum Chromodynamics

Quantum chromodynamics (QCD) is the quantum field theory describing the strong force. The predictions of QCD follow calculations of a gauge invariant Lagrangian that defines

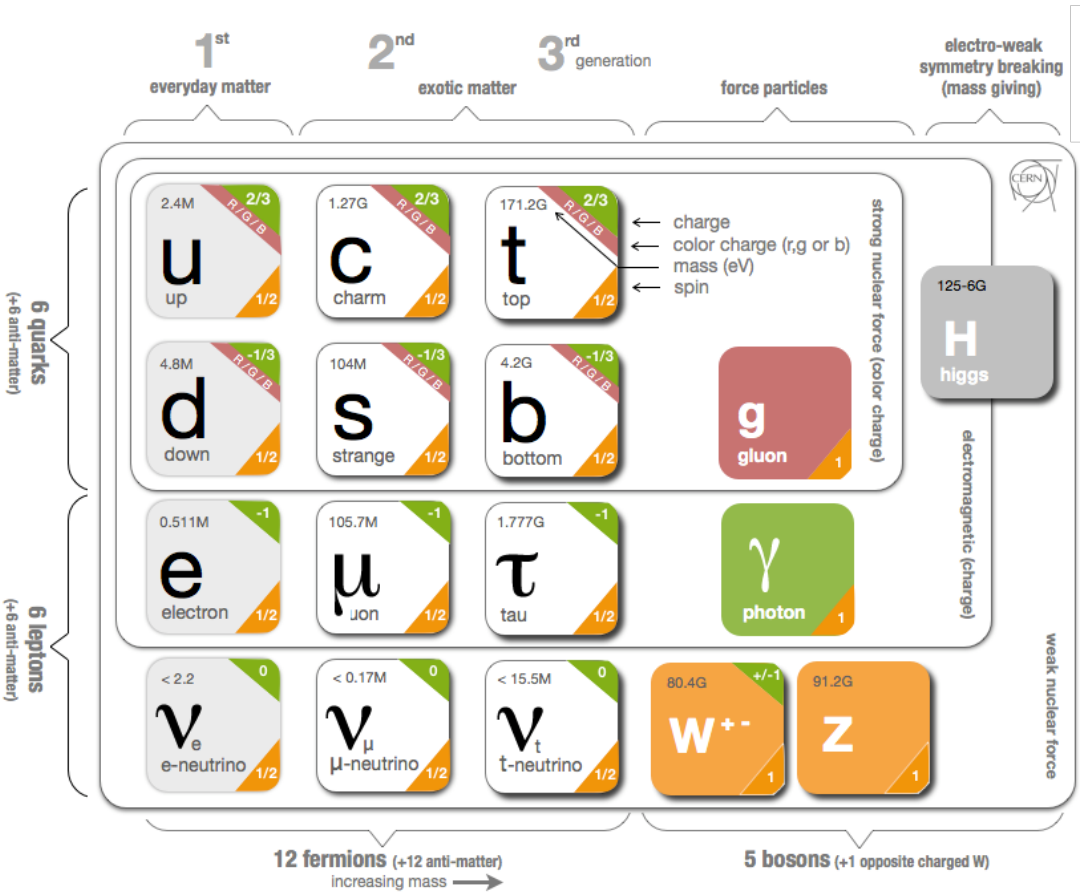

(a)

Figure 2.1: The standard model of elementary particles encompassing three generations of quarks, leptons, and neutrinos as well as the five force carrying bosons [18].

the evolution of particles as they interact strongly. Any number of interactions may follow from a single initial state, but as the final state increases in complexity its probability of occurring is reduced. The probability of any one interaction can be ascribed a value according to the transition amplitude given by S-matrix theory. The transition amplitude for complex interactions may be solved through the summation of multiple matrix elements for each interaction. QCD matrix element calculations become complex and tedious as more interactions are included but may be solved through simple Feynman diagrams. Created by Richard Feynman to simplify QCD calculations and facilitate their visualization, Feynman diagrams reduce the QCD calculations into a set of pictorial representations, one for each interaction allowed by QCD theory.

A set of Feynman diagrams representing basic strong force interactions is shown in Figure 2.2. The probability of any given Feynman diagram is determined by the product of the probabilities of each interaction point, with each individual probability proportional to the strong coupling constant (α_S). Only one interaction occurs in each of the Feynman diagrams shown in Figure 2.2, and each type of interaction has a theoretically calculated probability. The probability of an interaction is the same regardless of the orientation of the Feynman diagram, as with the rotated diagrams of Figure 2.2(a) and Figure 2.2(b). Rotating a Feynman diagram is equivalent to altering the time-ordering of the interaction.

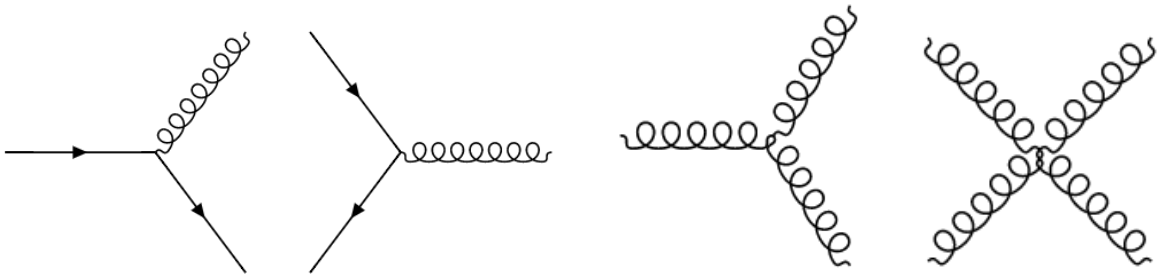

Figure 2.2: Feynman diagrams of basic QCD interactions including (a) gluon radiation, (b) quark anti-quark annihilation, (c) gluon splitting, and (d) gluon self-coupling. The matrix element, and therefore probability, is independent of the time-ordering, as with (a) and (b).

Feynman diagrams are not limited to straightforward interactions at a single point. Interactions of greater complexity are allowed involving multiple interactions points for any given particle, the inclusion of more initial and final state particles (tree-level contributions), and the introduction of virtual particles that are created and annihilated within the interaction, corresponding to a loop to the Feynman diagram. While the complexity of the Feynman diagram grows the dependence on α_S grows to higher orders. As an infinite number of diagrams exist a threshold on the maximum order of α_S used in calculations must be taken.

The simplest $2 \rightarrow 2$ scattering processes are calculated to $\mathcal{O}(\alpha_S^2)$ and are referred to as leading order (LO) matrix element calculations. More complex interactions of $2 \rightarrow 3$ scattering processes including tree-level interactions and virtual particles require terms up to $\mathcal{O}(\alpha_S^3)$ in the perturbative calculation, referred to as next-to-leading order (NLO) matrix element calculations. At each order the accuracy of the calculation is improved to a fraction

of the previous order. Calculations beyond NLO are possible but grow in mathematical complexity and computer processing intensity.

At any order of the matrix element calculation the integral over the infinite possible momenta of the emitted particles can lead to divergences. Divergences arise due to the inclusion of an infinite number of soft gluons or the emission of collinear particles in the tree-level diagrams. Loop diagrams of virtual particles will suffer from similar ultraviolet divergences, leading to unphysical probabilities. At any given order of the matrix element calculation the divergences of the tree-level and loop contributions are found to exactly cancel. However higher order contributions may still produce divergences which need to be suppressed.

Renormalization is a procedure by which the finite set of parameters of QCD are made dependent on the length or energy scale of the calculations to counteract the divergent contributions The magnitude of α_S is sensitive to the scale probed by the interaction, a phenomenon referred to as the running of the coupling. Renormalization of the interaction probability through the renormalization scale μ_{R} can solve the ultraviolet divergence that would occur from summing infinite low energy interactions. Similarly the value of α_S may be tuned to account for infrared divergences that would occur from runaway soft interactions at the factorization scale μ_{F}. The factorization scale defines the distance at which short-distance and long-distance strong interactions occur, and is essential for separating out the convoluted effects of the interactions, as detailed below. It is important to note that the renormalization is not a physical effect but accounts for the limited knowledge used in LO calculations.

A single outgoing parton will ultimately form a collection of energy deposits in the detector known as a jet. The evolution of an LHC collision event from the initial proton collision to the final collection of measured jets can be broken into three consecutive steps: hard scattering, parton showering, and hadronization. These steps are shown together for an example interaction in Figure 2.3.

2.1.1 Hard Scatter

The hard scatter of a proton-proton collision consists of the highest energy interaction in the event. The two highly energetic final state particles are the result of the position and relative

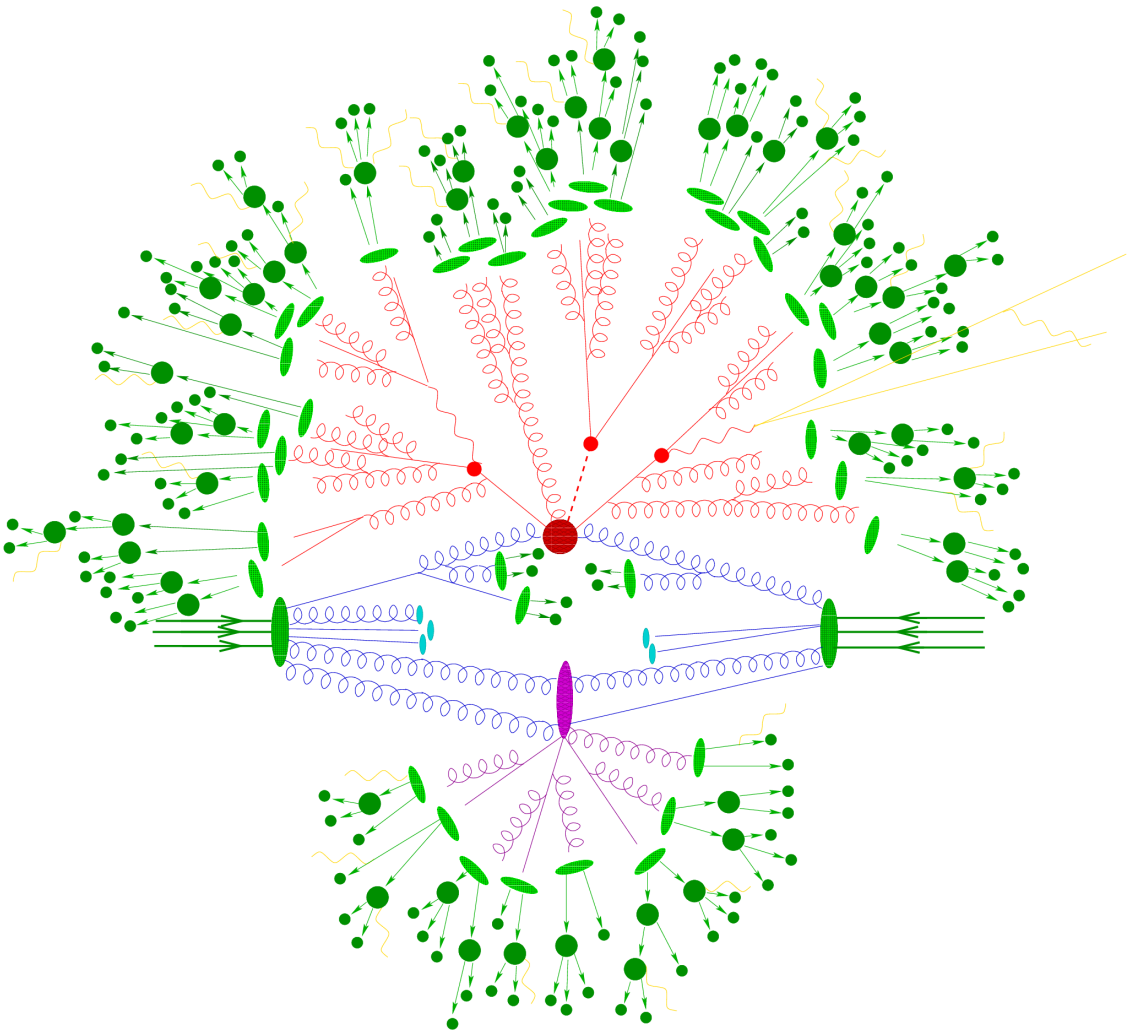

Figure 2.3: A typical proton-proton collision at the LHC [19]. Interactions may consist of large momentum transfers in the primary hard scatter interaction (red) leading to the most energetic final state particles. Secondary interactions involving smaller momentum transfers will lead to decay products of less interest, forming the underlying event (purple). At large energies partons will shower (red) according to perturbative QCD through processes such as gluon splitting. At smaller energies the partons will hadronize (green) into various baryons and mesons.

momentum of the interacting initial state partons and their $2 \rightarrow 2$ scattering interaction. While the scattering interaction may be calculated perturbatively through matrix element calculations of the relevant processes, the behavior of the partons within the proton cannot. However these two features can be separated into high-scale perturbative and low-scale non-perturbative components following the Factorization theorem [20].

Due to the QCD principle of asymptotic freedom, the strong force that binds quarks and gluons becomes asymptotically weaker at high energies and small distances. Accelerating protons, and their constituent partons, to large energies will therefore allow them to be treated as relatively free from one another. The probability that a parton will carry a specific fraction of the hadron's momentum x_q^h when measured at the momentum scale μ^2 GeV^2 is modeled by a parton distribution function (PDF) $f_q^h(x_q^h, \mu^2)$. The probability that two partons a and b of specific energies will scatter into a final state n is given by $\hat{\sigma}_{ab\to n}$. The total cross section for a collision process $ab \to n$ may therefore be derived by integrating over all possible initial state momentums for a and b and weighting them according to their PDF at a given momentum as in Eq. 2.1.

$$\sigma = \sum_{a,b} \int_0^1 \mathrm{d}x_a \mathrm{d}x_b \int f_a^{h_1}\left(x_a, \mu^2\right) f_b^{h_2}\left(x_b, \mu^2\right) \mathrm{d}\hat{\sigma}_{ab\to n} \tag{2.1}$$

PDFs are calculated using a set of renormalization group equations following DGLAP formalism [21]. They are used to calculate the probability that a parton will carry a specific momentum faction x_q^h at a measured interaction scale μ^2. Example PDFs are shown in Figure 2.4, describing the probability for various parton flavors to carry a fixed fraction of the proton's momentum. They are derived from global fits to multiple datasets from various collider and deep inelastic scattering experiments, each probing the PDF at a fixed scale. The PDFs of Figure 2.4 come from the NNPDF2.3 set [22, 23] which includes previous data collected at the LHC and which are calculated to NNLO, accounting for terms up to order α_S^3 in the DGLAP equations. In general the order of the PDF calculation should be equivalent or better than the order of the matrix element calculation.

A factorization scale μ_F must be introduced in the use of the Factorization theorem to specify a cutoff above which collinear radiation is directly treated and below which it is absorbed into the PDF definition. Ultimately the PDFs, representing measurable quantities, must be independent of this arbitrary μ_F, and extrapolations will introduce an uncertainty due to the factorization scale.

Given the PDF of the interacting partons, the scattering cross section can be calculated using a matrix element approach to determine $\hat{\sigma}_{ab\to n}$ of Eq. 2.1, which is dependent on both the μ_F and μ_R scales. QCD scattering is dominated by a momentum exchange between initial state partons, typically through the exchange of a gluon. The exchange of momentum

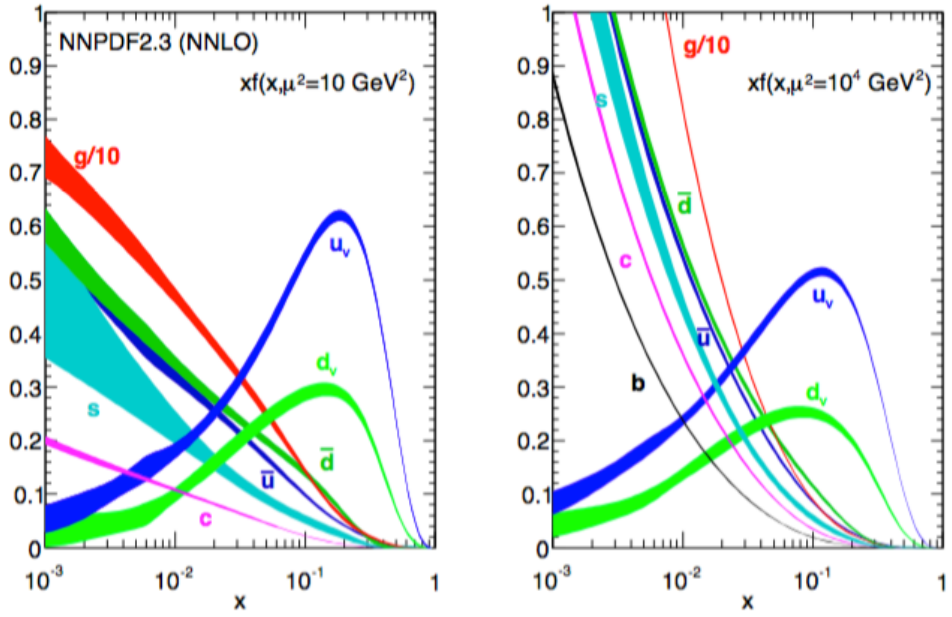

Figure 2.4: The PDF for various parton flavors calculated as a function of fractional parton momentum x at a scale of 10 GeV^2 (left) and 10^4 GeV^2 (right). Results from previous experiments are collected into the NNPDF2.3 set [22, 23].

is usually a small fraction of the total momentum, causing a slight change to the parton trajectory. Such exchanges are referred to as t-channel processes due to the dominance of the S-matrix theory Mandelstam variable t, and an example t-channel Feynman diagram is shown in Figure 2.5(a). Direct collisions of partons may also lead to the formation of distinct intermediate particles which then decay into two new particles of balanced momentum. Such exchanges, shown in Figure 2.5(b), are more likely to produce outgoing particles with momentum perpendicular to the initial state partons, and are referred to as s-channel processes.

Multiple-parton interactions may occur between the constituent partons of two colliding protons, with the highest energy interaction forming the hard scatter. The other interactions

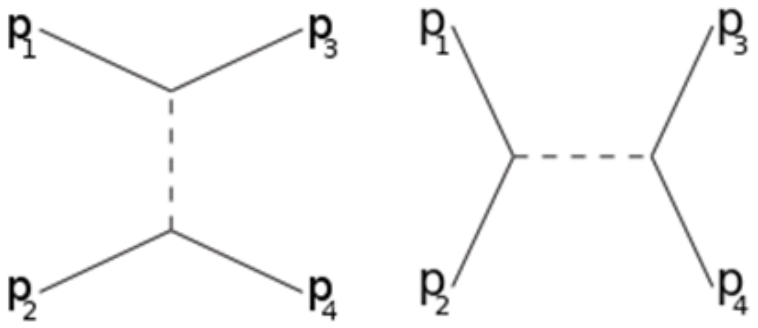

(a) (b)

Figure 2.5: Feynman diagram of a t-channel process (a), describing momentum exchanges, and a s-channel process (b), describing intermediate particle formation.

are typically of lower energy and uninteresting to analyses, commonly referred to as the underlying event. Background interactions may also arise from additional proton-proton collisions referred to as pile-up, a consequence of the large number of colliding protons at the LHC as described in Section 3.1. Both pile-up and multiple-parton interactions are simulated through the overlay of additional interactions in an event, with hard scatter correlations conserved in the case of multiple-parton interactions. Analyses usually attempt to reject or mitigate the contributions of pile-up and multiple-parton interactions in data.

2.1.2 Parton Shower

The highly energetic partons coming from the hard scatter will undergo the QCD radiation of gluons and the EM radiation of photons, as shown by the red and yellow lines in Figure 2.3. As gluons themselves carry color charge they can further radiate, leading to showers of particles known as jets. At high energies where QCD perturbation theory is valid the showering of a parton is approximated through a recursive splitting function. The probability of a single parton to split into two daughter particles is dependent on their relative final energies and the scale μ^2. The scale also provides a time-ordering of the cascade, and the probability of any given splitting is integrated over intervals of scale evolution $d\mu^2$ according to DGLAP formalism. The splitting function will continue on each of the daughter particles until their energies are low enough for confinement at a scale μ^2_{min} of ~ 1 GeV^2.

2.1.3 Hadronization

At low energies and large distances perturbation theory becomes invalid and quark confinement occurs. Individual partons begin to hadronize into colorless baryons and mesons. The energetic quarks within hadrons may separate, stretching the bonds of the strong force and causing gluons to split into $q\bar{q}$ pairs, leading to the proliferation of hadrons. Decays of excited hadrons to many lower-energy states will also occur.

Hadronization is typically calculated through either the cluster model [24] or the Lund string model [24, 25]. The cluster model begins with the non-perturbative splitting of gluons into color-singlet $q\bar{q}$ pairs, as shown in the left-hand side of Figure 2.6. Color-singlet combinations then form clusters which are individually analyzed to predict daughter hadrons based on the density of states and quantum properties. While fairly straightforward, the cluster model becomes inaccurate for increasingly massive clusters.

The Lund string model instead describes the color flux between the stretched $q\bar{q}$ pair, as shown in the right-hand side of Figure 2.6. Gluons are produced as kinks along the string and hadrons are produced according to the intensity of the color field lines. The model requires extra parameters to define the transverse momentum distribution and heavy particle suppression but provides a superior accuracy in meson and baryon production. The Lund string model is used in the simulation of hadronization for this analysis.

2.2 Motivation for New Physics

The SM provides a strong theoretical foundation to our understanding of high energy physics and agrees remarkably well with experimental results. However discrepancies exist which point to the possibility of BSM physics. An example is the hierarchy problem, described simply as a theoretical inconsistency between the relative strengths of the gravitational and electroweak forces. The differences can only be accounted for through very fine-tuned cancellations of force couplings against quantum corrections, an overly arbitrary and unlikely scenario.

Experimental evidence for BSM physics is also mounting. Analysis of galactic rotation curves [26] and gravitational lensing [27] point to discrepancies between the mass of galaxies as calculated through gravitational predictions and through extrapolations of the aggregate stellar luminosity. This discrepancy points to the existence of massive clusters of dark

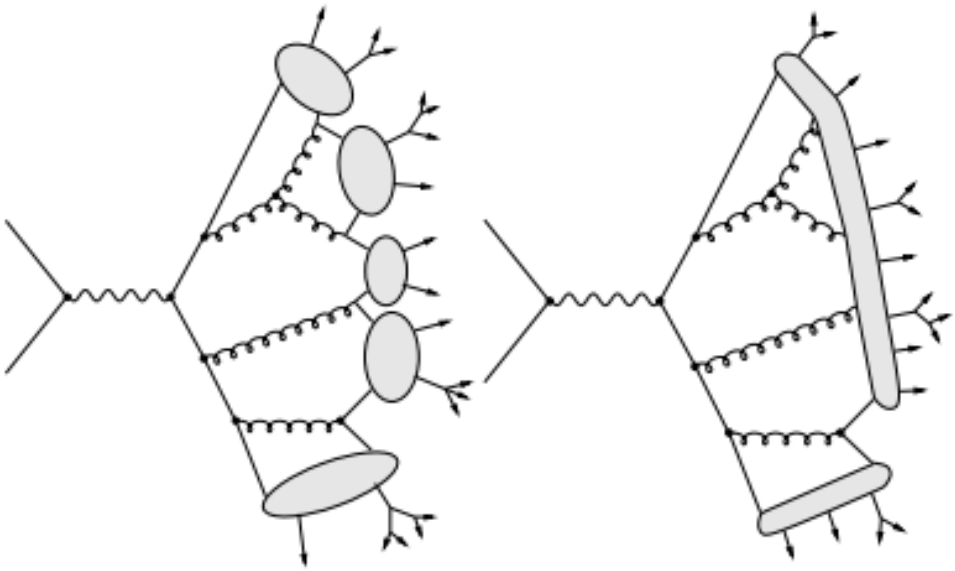

Figure 2.6: Cartoon of the cluster hadronization model (left), which treats individual color-singlets separately, and the Lund string hadronization model (right) which propagates field lines representative of color flux [24].

matter. Many cosmological observations, including the measurement of the cosmic microwave background [28], point to a universal composition of 5% matter, 27% dark matter, and 68% dark energy, another unknown form of energy.

Proton-proton collisions at a new energy frontier of 13 TeV have the potential to create new, heavy particles that are not predicted by the SM. New particles can be described by s-channel Feynman diagrams, with consequences for the kinematic behavior of the decay products. They decay products will, on average, appear differently in a detector than the dominant t-channel production of QCD scattering, offering a potential method of discrimination between BSM physics and SM processes. If a new particle couples to the SM it may be created by parton collisions at the LHC and can therefore subsequently decay into partons, leaving evidence of its existence.

Dark Matter is predicted to interact with the SM only weakly, or not at all. However many theories predict that there exists a second mediating particle Z' which couples to both dark matter and to SM particles [29]. An additional $U(1)$ gauge symmetry may extend the

SM such that some SM particles are charged under this new group. The Z' Lagrangian will contain parameters proportional to the dark matter particle mass, the Z' mass, and couplings to both the dark matter fermions and SM particles. Only the Z' mass and couplings to SM particles will be relevant in a dijet search, with the former determining the mass of the resonance and the later driving its width. A spin-1 mediator Z' of interest was identified in the joint ATLAS-CMS Dark Matter Forum Report [29].

The existence of higher-dimensional quantum black holes (QBH) [30, 31] at the TeV mass scale would provide a solution to the hierarchy problem. Several models of new physics predict the existence of extra dimensions in our universe through which only the gravitational force may interact. The leeching of the gravitational force outside of our four dimensions may account for its relative weakness, with the true scale of the gravitational force, the Planck scale M_D, smaller than currently measured. One such model developed by Arkani-Hamed, Dimopoulos, and Dvali [30] predicts the existence of 6 large, flat extra dimensions. A similar model proposed by Randall and Sundrum [31] predicts the existence of a single warped extra dimension.

If the energies probed by the LHC reach this new M_D it may manifest itself as the creation of QBHs above some threshold mass $M_{Th} > M_D$. If M_{Th} is roughly equal to M_D a QBH will quickly decay into two SM particles while obeying quantum conservation properties. If the scale of M_{Th} is much larger than M_D the QBH will thermally decay before reaching the M_D limit, likely producing numerous partons in a high multiplicity final state. A QBH would couple to SM particles gravitationally with a democratic probability to decay into partons, leptons, neutrons, or bosons. The large number of parton flavors leads to a relatively large branching ratio with respect to other SM particles. The flavor of the colliding partons also provide constraints on the created QBH, further favoring parton decays with branching ratios above 96%.

Many models of new physics are also driven by previous experience with the SM. The W and Z bosons are heavy particles which were first discovered by the S$\bar{\text{p}}$pS collider at CERN [32–35]. Sequential standard model theories [36] predict a continuation of the SM with the existence of heavier bosons with similar properties to the known W and Z. Other models predict that quarks are not fundamental particles, but are themselves made up of smaller particles. A quark substructure could explain the purpose of the three generations of quarks as well as their various masses and behaviors under weak interactions. Through

high energy collisions it may be possible to excite the constituents of a quark, leading to a decay system in which a single excited quark q^* decays into a quark and a gluon via gauge interactions [37].

New physics is not limited to these models but may appear in unexpected places with an unexpected form. In the dijet resonance search extra attention is given to each of the models above. However the search is ultimately model independent and is sensitive to any localized excess which may be caused by any BSM process.

CHAPTER 3
THE ATLAS EXPERIMENT

3.1 The Large Hadron Collider

The Large Hadron Collider (LHC) [1] is a circular accelerator designed to accelerate and collide protons at a center-of-mass energy of 14 TeV. Located 100 m beneath the border between France and Switzerland, the LHC occupies a 27 km long circular tunnel previously constructed for the Large Electron-Positron Collider (LEP) [38]. The LHC tunnel contains superconducting magnets and RF cavities designed to steer, focus, and accelerate protons to 7 TeV. Collisions between two counter-rotating beams of protons occur in 4 fixed positions around the circular tunnel, each holding a unique experiment: ALICE [39], ATLAS [2], CMS [40], and LHCb [41].

The LHC accelerator complex (Figure 3.1) consists of several increasingly powerful machines to accelerate bunches of protons to high energies. Hydrogen atoms are first ionized in an electric field and the resulting protons are sent through the linear accelerator LINAC2 where they are collected into bunches of roughly 1.15×10^{11} protons and accelerated to 50 MeV. The proton bunches are then sequentially accelerated to 1.4 GeV by the proton synchrotron BOOSTER, to 25 GeV by the proton synchrotron (PS), and to 450 GeV by the super proton synchrotron (SPS), after which they are injected in the LHC to be further accelerated to their final energies. To accelerate a single bunch from rest to 450 GeV requires approximately 17 seconds, with all bunches injected into the LHC beam over approximately 20 minutes. Over the next 30 minutes the proton bunches are further accelerated, squeezed into a condensed beam, and validated for physics readiness. Collisions commence once beams are stable and continue until the beam luminosities have decreased by roughly 50%, potentially up to 24 hours later. At this point the bunches have lost a significant portion of their protons and the reduced data collection rate justifies a new fill. Collisions may also end abruptly due to accelerator malfunctions or unexpected beam loss.

An indicator of the productivity of the beam, measuring the yield of high energy collisions, is quantified by the term luminosity. The luminosity ($\mathcal{L}$) is proportional to the number of interactions per second; it's integral over time proportional to the total number of interactions. The integrated luminosity defines the amount of data collected and is measured

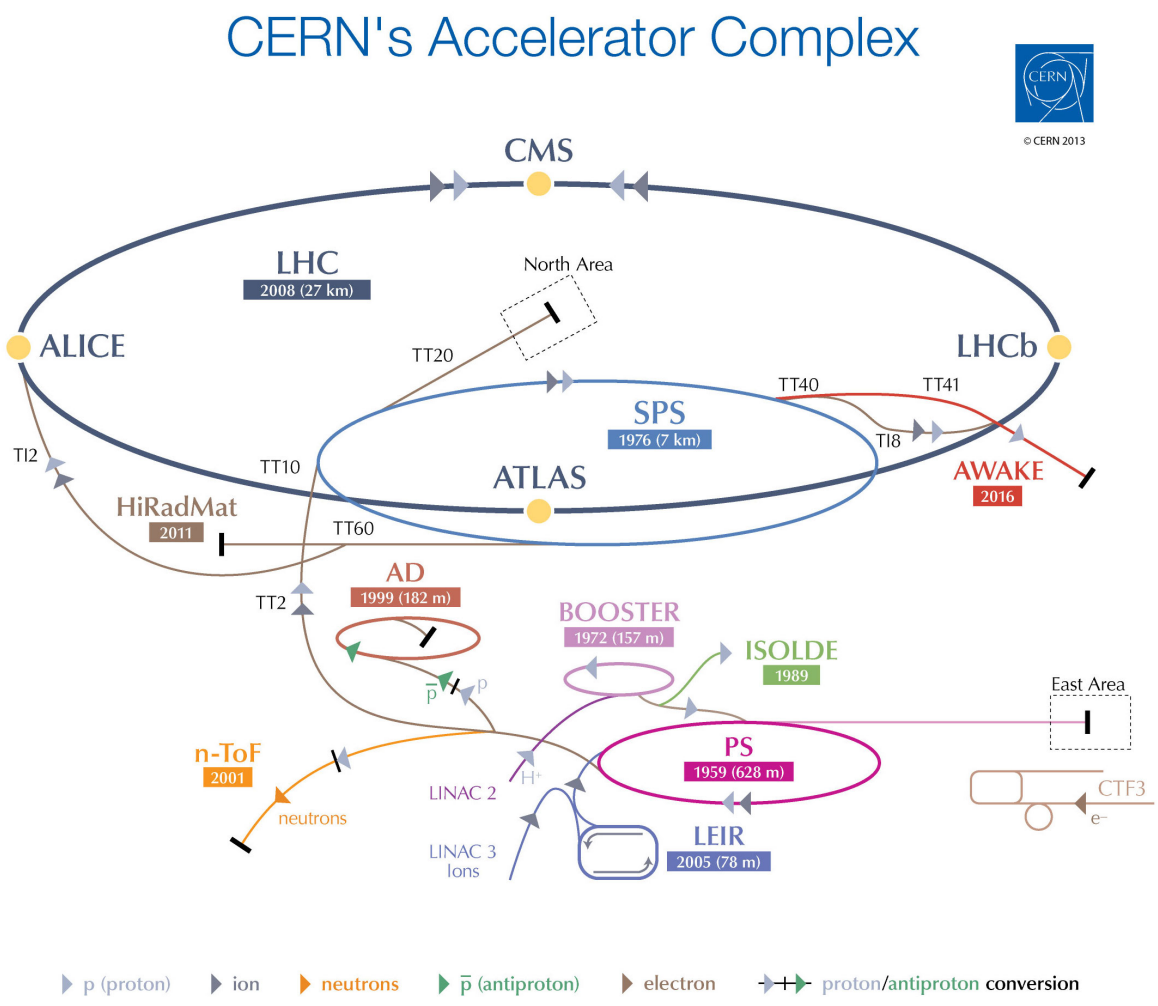

Figure 3.1: Cartoon of the CERN accelerator complex including the LINAC2, BOOSTER, PS, SPS, and the LHC [42].

experimentally by both the ATLAS detector [43] and the specialized standalone detector LUCID [44]. The integrated luminosity is cross-checked with independent measurements by the CMS experiment [45].

The luminosity may also be calculated as a function of beam parameters according to Eq. 3.1.

$$\mathcal{L} = \frac{N_b^2 F}{4\pi\beta^*}\frac{\gamma}{\epsilon_n} n_b f_{rev} \tag{3.1}$$

Here N_b is the number of protons per bunch (assumed to be equal in both beams), n_b

the number of bunches injected at the LHC revolution frequency f_{rev} of 11.2 kHz, and γ the relativistic factor of protons near the speed of light. The normalized transverse beam emittance ϵ_n reflects the average spread of partons in position-momentum phase space. The geometric luminosity reduction factor F serves as a small correction factor to account for the crossing angle between beams at the interaction point and is roughly calculated to be 85% during 2015 operation [46]. A measure of the envelope of the beam at the interaction point, β^*, is minimized by focusing magnets. In 2015 β^* was constrained between 40 and 80 cm.

3.1.1 LHC Operation

The planned operation of the LHC is broken down into distinct runs, each lasting several years and separated by long shutdowns for substantial repairs and upgrades. Three runs are planned for the current iteration of the LHC spanning between 2009 and 2023. The first run, formally named Run 1, occurred between 2009 and 2013 and marked the first operation of the LHC. It was operated conservatively at half the design luminosity, collecting 5.08 fb^{-1} at 7 TeV and 21.3 fb^{-1} at 8 TeV. Run 1 was an immense success, resulting in over 500 ATLAS publications and the discovery of the Higgs boson.

Run 2 began in 2015 with the purpose of collecting roughly 150 fb^{-1} of data at energies close to the design limit of 14 TeV. An integrated luminosity of 4.2 fb^{-1} was delivered by the LHC to the ATLAS detector at a center-of-mass energy of 13 TeV between May and November of 2015, shown in Figure 3.2(a). Run 2 will continue at 13 or 14 TeV through 2018, after which a 2 year-long shutdown will be used to repair and upgrade the LHC and detector experiments in anticipation of Run 3.

Proton bunches at the LHC are organized consecutively into groupings called bunch trains. Each bunch train includes 36 bunches separated by a bunch spacing of 25 ns. Each bunch has a length of about 1.1 ns such that bunches are well separated. The 25 ns bunch spacing defines the smallest unit of time, and therefore distance, that separates consecutive bunch sites, witheach assigned a unique bunch crossing identification (BCID). Bunch spacings are assigned a BCID whether they are filled with protons or are empty. Bunch trains are generally separated by only a few empty BCIDs. A single larger gap of roughly 300 empty BCIDs ($\sim 7\ \mu s$) allows for quick detector calibrations during data-taking.

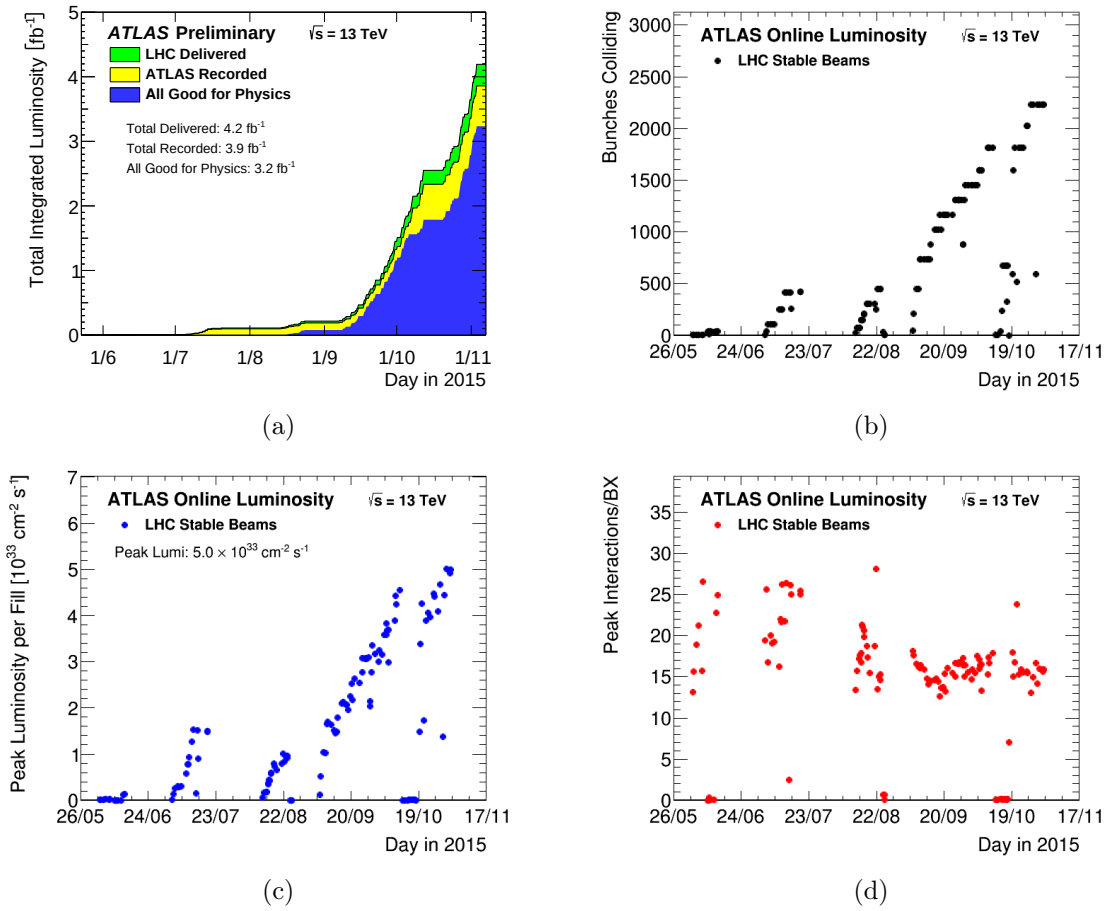

Figure 3.2: Online histograms of ATLAS luminosity: (a) The luminosity delivered (green), recorded (yellow), and suitable for physics (blue) in the ATLAS detector; (b) The number of bunches collided on each day; (c) The peak instantaneous luminosity on each day; (d) The peak number of interactions per bunch crossing on each day.

The first operation of the LHC at 13 TeV required a slow, controlled startup to test and gain experience with the cryogenics, SPS injection, and magnet and RF cavity operation. During early tests several unidentified falling objects (UFOs) and unidentified lying objects (ULOs) consisting of dust or foreign objects were observed within the beampipe. These objects interfered with normal operation, causing interactions within the path of the beam and leading to particle showers that heat the superconducting magnets and lead to beam losses. The number of UFOs was found to decrease over time, shown in Figure 3.3, allowing for stable runs with more injected bunches. The number of injected bunches was slowly increased up to 2244 by the end of data-taking, as shown in Figure 3.2(b).

Under Run 2 conditions the instantaneous luminosity recorded by ATLAS reached $5 \times 10^{33}\text{cm}^{-2}\text{s}^{-1}$, shown in Figure 3.2(c). This corresponds to an average of ~ 16 collisions per bunch crossing, shown in Figure 3.2(d).

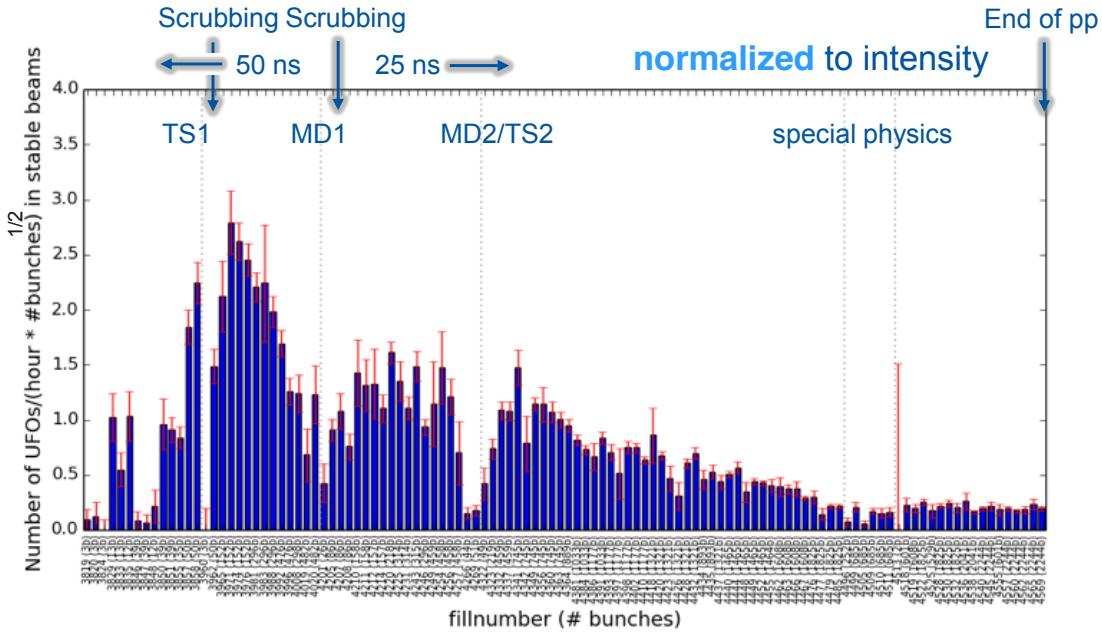

Figure 3.3: Number of UFOs detected as a function of time, normalized to beam intensity. Plot from Bernhard Auchmann [private communication].

3.2 The ATLAS Detector

ATLAS is a multipurpose, hermetic detector of nearly 4π[1] radians of solid angle coverage around the central interaction point. The detector has been designed to identify particles produced by proton collisions and accurately measure their kinematic properties over a wide range of energies and to a high resolution. ATLAS consists of several subdetectors, shown in Figure 3.4, arranged in concentric layers about the beam axis. Each is uniquely designed

1. The ATLAS reference system is a Cartesian right-handed coordinate system, with the nominal collision point at the origin. The anticlockwise beam direction defines the positive z-axis, while the positive x-axis is defined as pointing from the collision point to the centre of the LHC ring and the positive y-axis points upwards. The azimuthal angle ϕ is measured around the beam axis, and the polar angle θ is measured with respect to the z-axis. Pseudorapidity is defined as $\eta = -\ln[\tan(\frac{\theta}{2})]$, rapidity is defined as $y = 0.5 \ln[(E + p_z)/(E - p_z)]$, where E is the energy and p_z is the z-component of the momentum, and transverse energy is defined as $E_T = E \sin\theta$.

to detect the energy signature of passing leptons, photons, and hadrons, as visualized in Figure 3.5. All together the detector weighs approximately 7000 tons and has a cylindrical profile 25 m in diameter and 44 m in length.

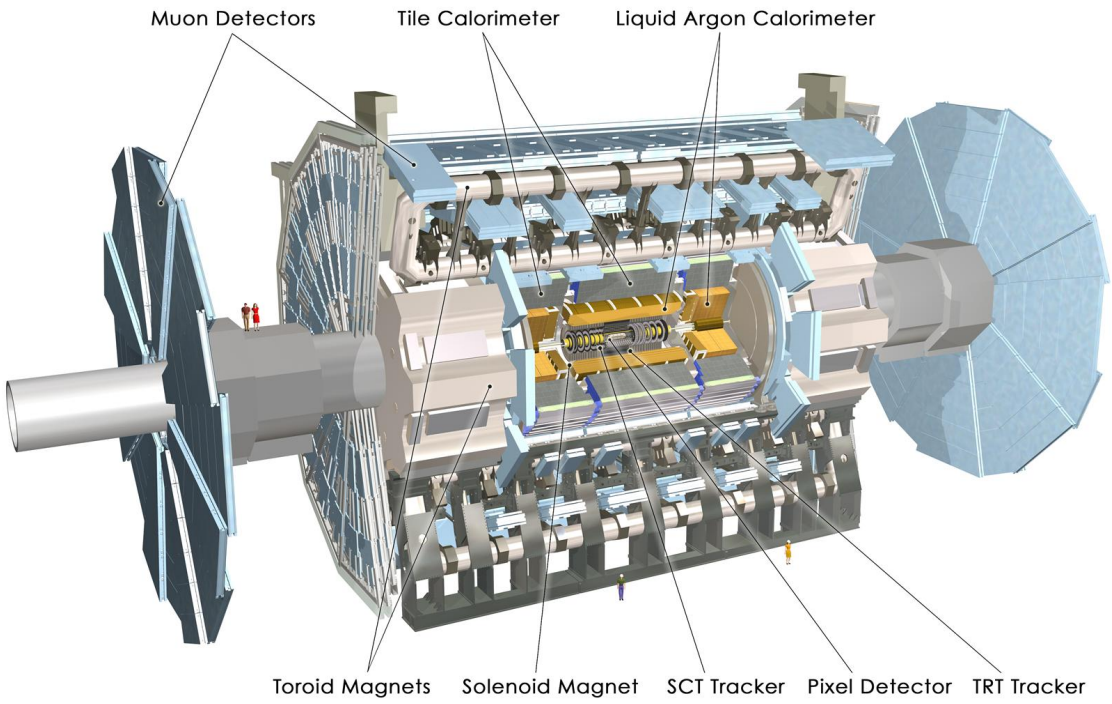

Figure 3.4: Image drawn to scale of the ATLAS detector showing the Inner Detector (Pixel, SCT, TRT), the Liquid Argon Calorimeter, the Tile Calorimeter, the Muon Detectors, and the Toroid and Solenoid magnets.

Charged particle tracks are reconstructed in the inner detector (ID), composed of 3 subdetectors: a silicon pixel tracker closest to the beam, a micro-strip silicon tracker, and a straw-tube transition radiation tracker furthest from the beam. The ID is surrounded by a thin solenoid providing an axial magnetic field of 2 T that bends the trajectory of charged particles, allowing for the measurement of their momenta. Neutral and charged particles leaving the ID are absorbed and measured in the sampling electromagnetic (EM) and hadronic calorimeters. The muon spectrometer surrounds the ATLAS calorimeters and measures the position and energy of charged muon tracks. Three large air-core toroids surround the muon spectrometer with a magnetic field to allow the measurement of muon momenta.

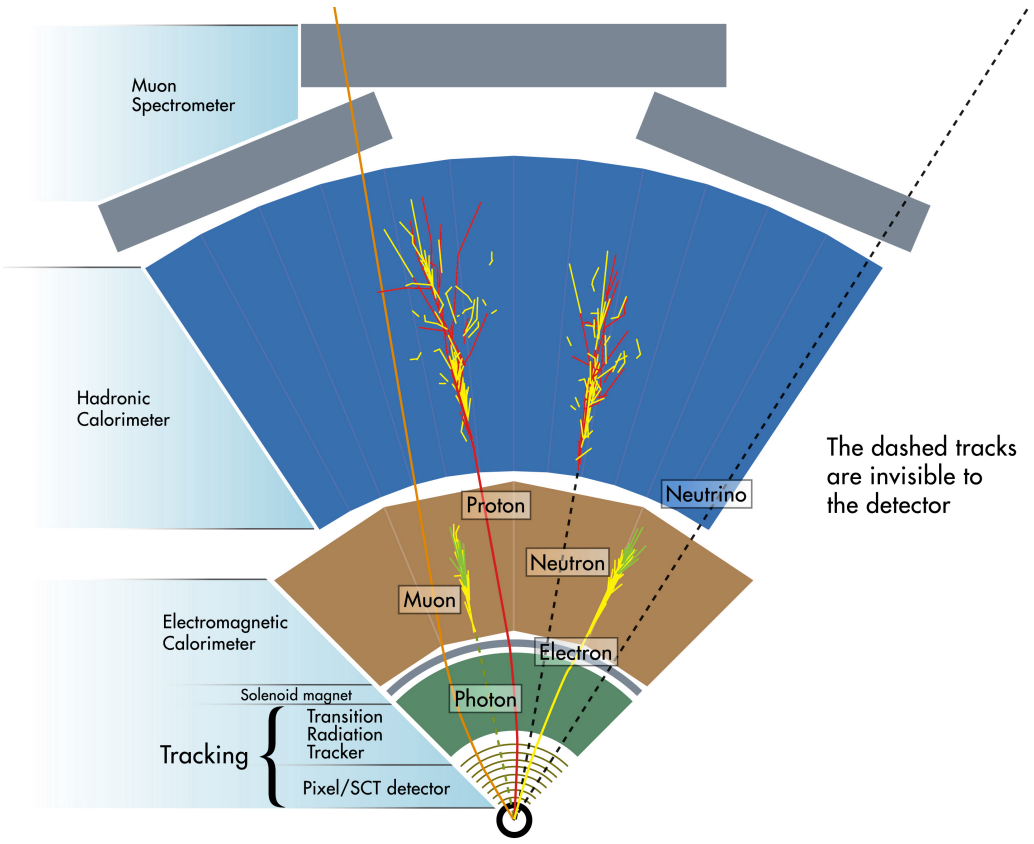

Figure 3.5: A cross section of the detector showing subdetectors and their interaction with basic particles. Solid lines signify energy deposited by a single charged particle, groups of lines signify particle showers, and dotted lines signify no interaction with the subdetector.

3.2.1 Inner Detector

The ID performs precision tracking of charged particles of $p_{\mathrm{T}} > 0.1$ GeV over the pseudo-rapidity range $|\eta| < 2.5$. Three independent subsystems at various radii cover this phase space between 3.3 and 101.6 cm away from the beam axis. Each subdetector is split into cylindrical concentric barrel modules covering the central region, shown in Figure 3.6, and into disk-shaped end-cap modules covering the forward regions, shown in Figure 3.7.

Pixel Detector

The Pixel detector consists of 4 barrel and 2×3 end-cap layers of silicon semiconductor pixel sensors which locate spatial hits and measure the energy deposited by ionizing particles. The barrel layers cover a radii between 3.3 and 15 cm. Each end-cap consists of three disks which

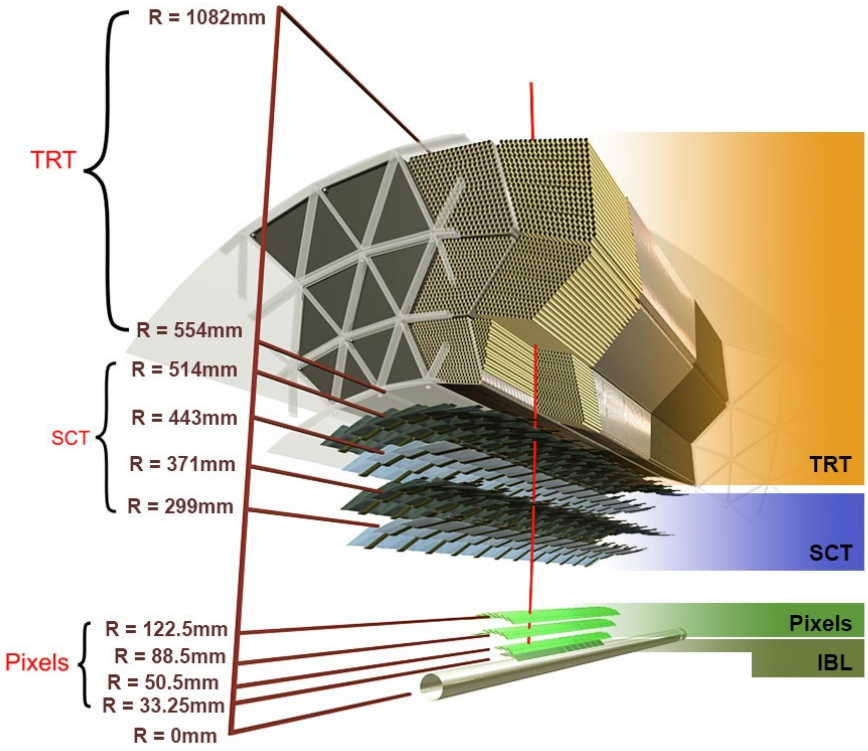

Figure 3.6: Cartoon of the central region barrel of the ATLAS inner detector including the Pixel layer (including IBL), SCT, and TRT [47]. Distance of concentric layers from the beam axis are drawn to scale and labeled.

extend coverage to $|\eta| < 2.5$. The ∼75 million pixels used in the 3 outer layers (3 disks) of the barrel (end-cap) region provide a spatial hit resolution for a point on a charged particle's trajectory of 10 μm in the R-ϕ plane and 115 μm along the z (R) axis. For Run 2 a fourth, innermost layer was installed in the barrel region, the insertable B-layer (IBL) [49], at a radial distance of 3.3 cm. The IBL provides additional 8 million pixels covering over 12 ϕ sectors close to the beam line, with each pixel providing a spatial hit resolution of 8 μm (R-ϕ) and 40 μm (z). This new addition improves the track reconstruction, vertex measurement, and the identification of b-quarks which typically decay beyond the IBL radius [50, 51].

Semiconducting Tracker

The semiconducting tracker (SCT) lies outside the Pixel detector and is similarly composed of silicon semiconductor sensors segmented into strips rather than pixels. A hit along a strip is accurate to within 17 μm (R-ϕ) and 580 μm (z). Two individual layers of strips are closely

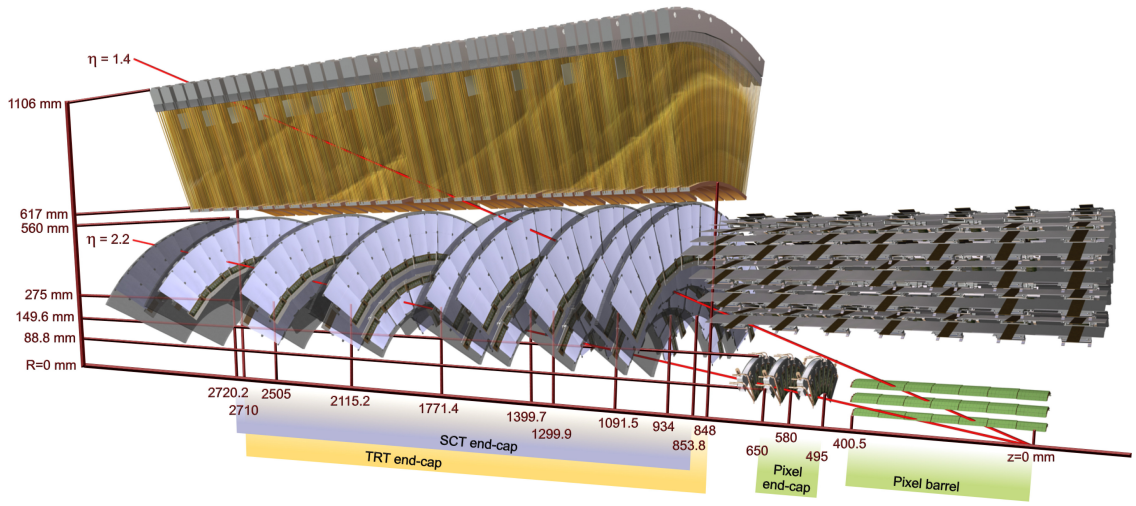

Figure 3.7: Cartoon of the forward region end-cap of the ATLAS inner detector including the Pixel layer, SCT, and TRT [48]. The IBL is not shown. Distance of disks from the beam axis are drawn to scale and labeled.

laid at a slight angle to form a double layer, creating a stereo-pairing resulting in an improved 17 μm resolution in z. The barrel region consists of 4 double layers covering radii between 29.9 and 56.0 cm, providing four spatial measurements for tracks in the central region. Nine disks of double layer strips cover each end-cap region, extending coverage to $|\eta| < 2.5$.

Transition radiation tracker

The transition radiation tracker (TRT) is composed of straw tubes measuring 144 cm in length and 4 mm in diameter. They are filled with a gas mix consisting of 70% Xe, 27% CO_2, and 3% O_2. During 2015 the xenon was replaced by argon in regions of substantial gas loss to reduce operational costs [52]. A single gold-coated tungsten wire, 31 μm in diameter, is stretched down the center of each straw tube and serves as an anode kept at ground potential. The walls of each straw tube serves as a cathode and are kept at a negative potential of roughly -1.5 kV. As charged particles cross a straw tube they ionize the gas mixture, causing electrons and positive ions to drift apart in the electric field and providing a signal proportional to the energy deposited by the particle. Each straw tube can provide a spatial hit resolution of 130 μm in a plane perpendicular to the wire.

The barrel region consists of 72 layers of 144 cm long straw tubes running parallel to the beam axis, covering a radius of 56.3 to 106.6 cm. The end-cap regions each consist of 160

layers of 36 cm long tubes, radially oriented on 18 wheels. A total of 350,848 straw tubes are used to to improve the tracking resolution up to $|\eta| < 2.5$. The space between TRT layers is also filled with a polypropylene radiator to provide discrimination between electrons and heavier charged particles. Electrons passing through the radiator will release a significantly larger amount of transition radiation than heavier charged particles, such as pions.

All three tracking subdetectors are immersed in a 2 T axial magnetic field provided by a superconducting solenoid held at 4.5 K by liquid helium. The solenoid consists of superconducting NbTi cables and a light weight aluminum cylinder, minimizing the amount of non-active material in the detector. The strong magnetic field bends charged particles within the ID, allowing their momenta to be accurately measured through the curvature of their tracks.

A charged particle of $p_{\mathrm{T}} > 0.5$ GeV traversing the ID barrel will typically produce 4 pixel hits, 8 SCT hits, and more than 30 TRT straw hits. Hits in all layers of the ID are combined into a single particle track through track finding algorithms. In 2015 the track reconstruction efficiency for charged particles of $p_{\mathrm{T}} = 0.5$ GeV was 77%, increasing to 88% for particles of $p_{\mathrm{T}} = 40$ GeV. During ID commissioning the relative track momentum resolution was measured to be $\sigma_p/p = (4.83 \pm 0.16) \times 10^{-4}$ GeV$^{-1} \times p_{\mathrm{T}}$ [53].

3.2.2 Calorimetry

The ATLAS calorimeters are used to absorb particles exiting the ID and accurately measure their energy. The calorimeters, shown in Figure 3.8, envelop the ID and extend out to $|\eta| < 4.9$. They are segmented into towers in η and ϕ which point towards the center of the detector. ATLAS calorimeters are sampling calorimeters [54] consisting of alternating layers of passive and active material which induce particle showers and measure their energy, respectively.

The active material reacts to passing charge particles and consists of either plastic scintillators or liquid argon. In plastic scintillators the electromagnetic particles produce light through photoelectric absorption, Compton scattering, and pair production. The number of photons produced is proportional to the energy deposited by the incident particle and is guided to photomultiplier tubes (PMTs) by optical fibers. In the liquid argon medium the incident charged particles ionize the liquid, causing electrons and positive ions to drift

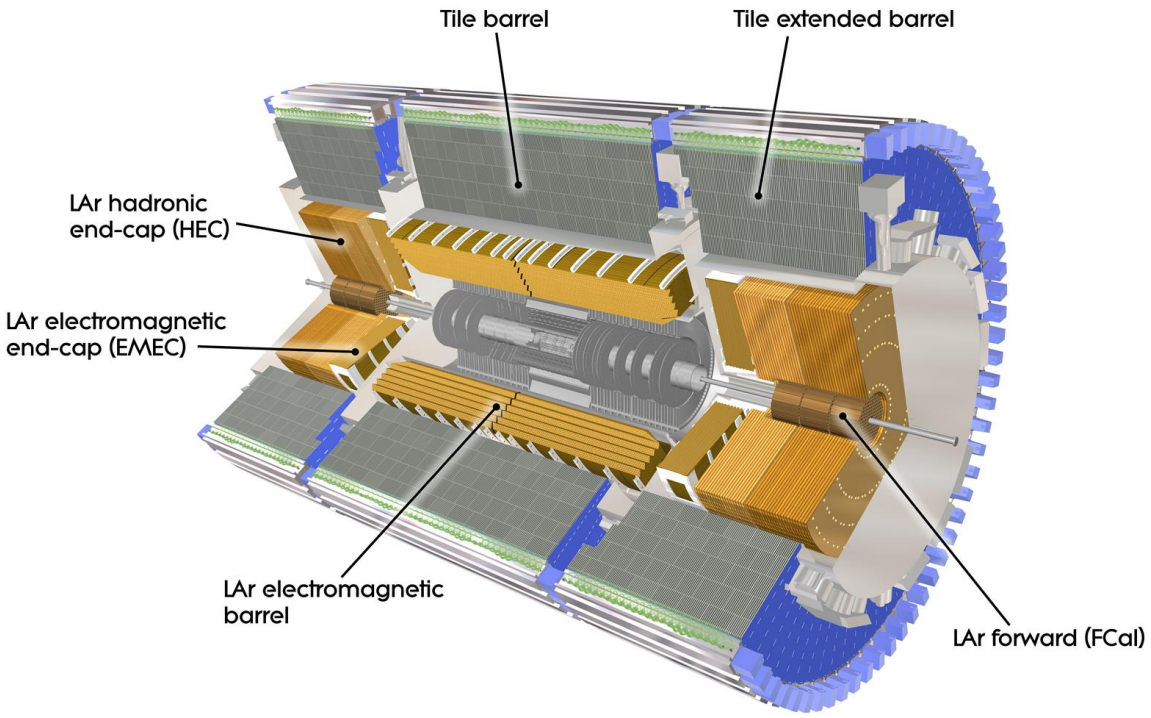

Figure 3.8: Image of the ATLAS detector to scale with a focus on the calorimeters, including the Tile barrel, Tile extended barrels, EMB, EMEC, HEC, and FCal. [2]

towards electrodes which measure the deposited charge.

Passive material consists of heavy absorber material which interacts with both charged and neutral particles but which does not measure the deposited energy. Incident particles may interact with the material through several mechanisms. Charged particles can radiate photons through bremsstrahlung, which may pair-produce electrons and positrons that may themselves radiate further photons. Hadron-nucleon scattering can produce strongly interacting particles which can further interact with both the active and passive materials, again causing a shower of particles. Through this process the energy of charged and neutral particles may be measured and contained within the calorimeter.

Electromagnetic calorimeters focus on measuring the energy of electrons and photons, while hadronic calorimeters focus on measuring the energy of strongly interacting particles, as described in Figure 3.5. Muons deposit a relatively small amount of energy in the calorimeters as they are not strongly interacting and are more massive than electrons. Neutrinos do not

interact with the calorimeters at all, appearing only as a momentum imbalance inside the detector.

Minimizing the resolution of the energy response is essential to providing an accurate measurement of particle energy. The fractional calorimeter resolution as a function of energy is described as

$$\frac{\sigma_E}{E} = \frac{N}{E} \oplus \frac{S}{\sqrt{E}} \oplus C \tag{3.2}$$

where N is a measurement of the noise, dominant at low energies, arising from background and electronics, S parameterizes the stochastic uncertainty due to the random sampling of the active and passive materials, and C is a constant term, dominant at higher energies, arising from non-uniformities in the detector. These terms are added in quadrature ($\oplus$) to derive the fractional resolution. Experimental values for these constants are listed below for each calorimeter.

3.2.3 Electromagnetic Calorimeters

The EM calorimeters detect electrons and photons within $|\eta| < 3.2$. It is the closest calorimeter to the interaction point, requiring a high radiation tolerance and fine granularity in η and ϕ to measure the narrow showers of light EM particles. The ATLAS EM calorimeters use liquid argon (LAr) as the active material due to its high radiation tolerance and uniformity. Argon is held in a liquid state at 89 K through the use of cryostats.

Lead absorbers are used in the EM barrel (EMB) and the EM end-cap (EMEC). The EMB is layered in concentric shells, covering a radial distance between 1.25 and 2.05 m over $|\eta| < 1.475$ and sampling with a transverse granularity of 0.025×0.025 $(\eta - \phi)$. The EMEC consists of two coaxial wheels on either side of the detector, covering $1.375 < |\eta| < 3.2$ with a granularity of 0.025×0.1 $(\eta - \phi)$. A presampler (PS) consisting of thin segments of LAr without absorbers are placed before the instrumentation in front of the EMB and EMEC. The barrel PS covers $|\eta| < 1.475$ while the end-cap PS covers $1.5 < |\eta| < 1.8$.

Both the EMB and EMEC are segmented radially into three read-out layers to allow for measurement of longitudinal shower profiles, as shown in Figure 3.9. Within each layer are lead plates organized into an accordion structure that allows for uniform sampling across the full ϕ coverage and eliminating the need for servicing gaps. The effective thickness for electrons and photons in each layer is shown in Figure 3.10. It is measured in terms

of radiation lengths (X_0) and varies as a function of η. The total radiation length varies between 22 and 33 X_0, ensuring that the energy of electrons and photons is mostly contained within the EM calorimeters.

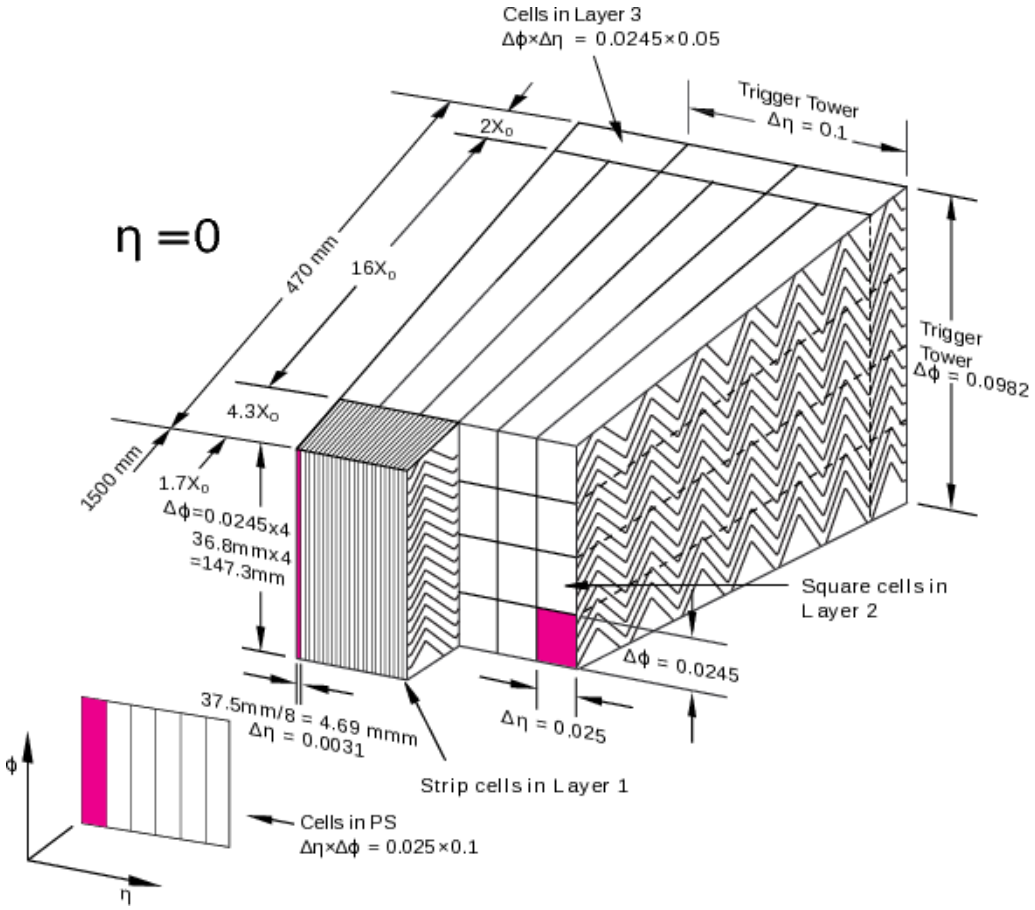

Figure 3.9: A slice of the PS and EMB showing the size, thickness in radiation lengths, and granularity in η and ϕ of cells in each of the 3 layers.

Readout electrodes are placed between absorber plates and are held at 2 kV to collect charge from the ionized LAr. The average drift time of electrons is roughly 450 ns, leading to long analog signal pulses shown by the solid line in Figure 3.11. The signal is shaped to have a long negative tail used to restore the signal baseline and to reduce the sensitivity to pile-up [55]. The pulses are sampled digitally every 25 ns with four samples used to extract the signal pulse shape for amplitude and timing measurement. Five samples had been used to extract the pulse shape during the 2012 data-taking period but offered no substantial improvement over four samples. The four signal samples are converted to an energy

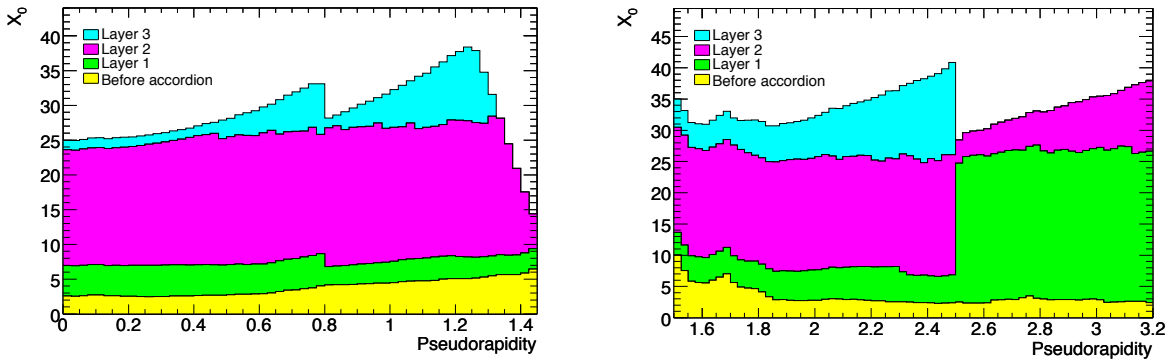

(a) (b)

Figure 3.10: Cumulative radiation length (X_0) before and within the EMB (a) and EMEC (b) as a function of η.

measurement using constants calculated through test-beam data and dedicated calibration runs [2, 56]. The response resolution (Eq. 3.2) of the stochastic and constant terms were measured to be

$$\frac{\sigma_E}{E} = \frac{10\%}{\sqrt{E}} \oplus 1\% \tag{3.3}$$

3.2.4 Hadronic Calorimeters

The hadronic calorimeters contain and measure the energy of hadron showers within $|\eta| < 3.2$. Hadron showers will deposit a fraction of their energy in the EM calorimeters but usually extend past its 2 nuclear interaction lengths (λ). The hadronic calorimeters extend this by up to 10 λ, fully containing most high energy hadron showers. The hadronic calorimeters consist of the central Tile Calorimeter and the forward hadronic end-cap calorimeter. A separate forward calorimeter covers the region $3.1 < |\eta| < 4.9$ where no dedicated EM calorimeter exists.

The Tile Calorimeter (TileCal) consists of plastic polystyrene scintillator tiles with steel absorbers incorporated in the barrel ($|\eta| < 0.8$) and extended barrel ($0.8 < |\eta| < 1.7$) regions. There are four regions which each consists of 64 wedge-shaped modules in ϕ that contain the scintillator, steel, and read-out electronics, shown in Figure 3.12. The electronics are housed in steel support structures furthest from the beamline to reduce radiation exposure. Alternating steel and polystyrene are segmented radially into three read-out layers, allowing

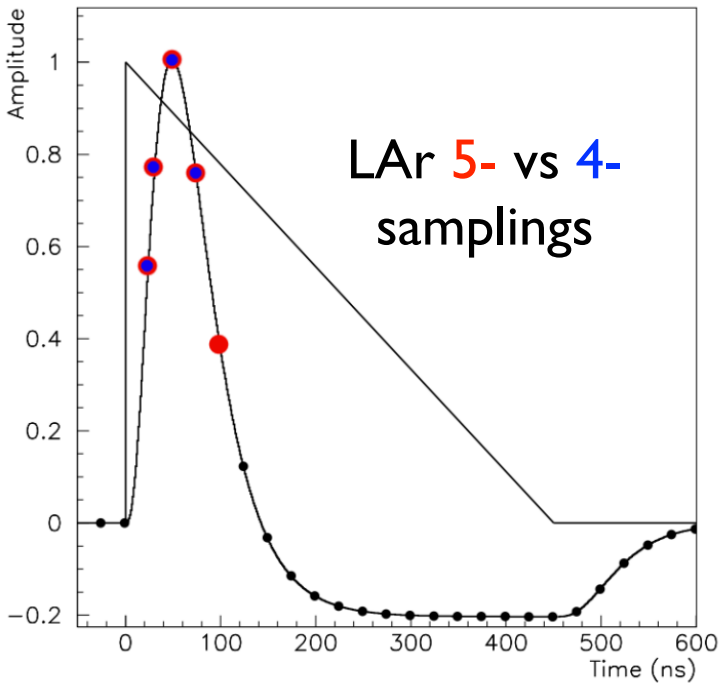

Figure 3.11: The triangular signal shape of LAr signal amplitude versus time (solid line) compared to the shaped bi-polar pulse of the readout electronics (circles). Four samplings (blue) are used to measure the pulse amplitude and time in contrast to five (red) in 2012.

for the measurement of longitudinal shower profiles. The layer thickness in terms of λ are shown in Figure 3.13, with roughly 1.5, 4.1, and 1.8 in the barrel and 1.5, 2.6, and 3.3 in the extended barrel.

Wavelength shifting fibers connect the polystyrene plates to photomultiplier tubes (PMTs). The PMTs convert the ultraviolet light produced in the scintillator due to passing charged particles into an electrical signal. The scintillators are grouped into cells of 0.1×0.1 in $\eta - \phi$ in the first two layers and 0.2×0.1 in $\eta - \phi$ in the 3rd layer. Each cell is read-out on both sides by two PMTs, requiring a total of 9,852 PMTs to service the whole detector. Individual scintillators in the gap between the barrel and the extended barrel serve a similar purpose to that of the EM presampler.

Readout electronics located in steel girders are used to shape, amplify, and sum PMT signals. Narrow signals are shaped into pulses with a full width half maximum of 50 ns. The shaped pulses are amplified at two complementary gain scales (1:64) to fully cover cell energies from roughly 220 MeV to 1.4 TeV and are subsequently digitally sampled at 40 MHz.

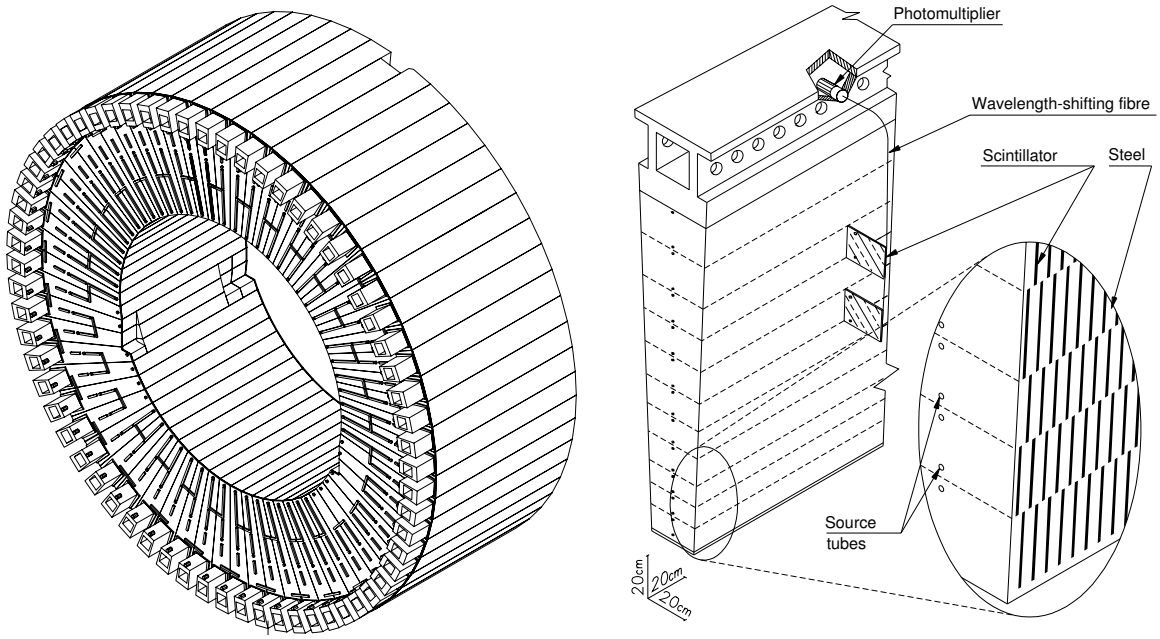

Figure 3.12: Sixty-four wedges (left) completely cover the beamline in ϕ. Individual wedges (right) are formed from layers of steel and scintillator connected to PMTs by waveguides. Also shown are holes for source tubes used to deliver the cesium source for calibrations.

Seven samples of the shaped pulse are fit with optimal filter coefficients [57] to extract the signal magnitude and timing. The steel girders also house low-voltage power supplies and infrastructure used to distribute high voltage to the PMTs.

Several calibration procedures are used to correct the measured energy to the EM scale. Calibrations are used to derive initial conversion factors and to account for changes in the scintillator response over time or in the gain of individual PMTs over time, caused by light and radiation exposure as well as temperature fluctuations. The individual calibrations target different stage of the measurement, and are described as follows.

Single Particle

The electromagnetic and hadronic response of the Tile Calorimeter was measured in a test beam [58] prior to installation in ATLAS. Tests were performed on 11% of the

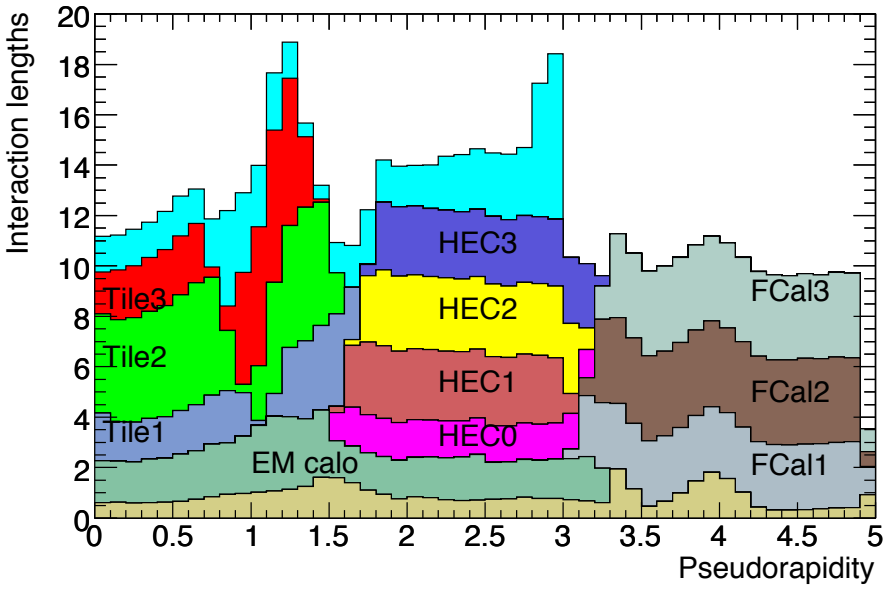

Figure 3.13: Cumulative interaction length (λ) of various ATLAS subdetectors as a function of η. Individual calorimeters are shown and labeled, as well as the total interaction length before the calorimeters (brown) and within the muon spectrometer (cyan).

TileCal modules and the response in each was probed using electron, muon, and hadron beams of various energies between 3 and 350 GeV. The variation in the response over many modules and rapidities was found to be 2.4% for electrons, 2.5% for muons, and 1.4% for hadrons. The test beam provided an overall calibration C_{TB} of particle energy (MeV) to PMT response (pC).

Cesium and Minimum Bias Systems

The Cesium (Cs) scan system propagates a ^{137}Cs source through a negative pressure water transportation system, releasing 0.662 MeV photons into the scintillators. A special slow integrator readout measures the PMT signal with a time constant of $\tau = 90\ ms$, allowing a relative calibration of the scintillator and PMT responses (C_{Cs}). Cs scans are generally taken once per month to derive new values of C_{Cs} for each cell and are accurate to within 0.3%.

The slow integrator is also used to measure the response of the scintillator+PMT system to beam-beam interactions. Minimum bias events are selected from data in a randomized manner, selected proportionally to the instantaneous luminosity, such that

soft parton interactions are favored. These events are used to monitor the integrated current over time.

LASER

The LASER calibration system corrects for changes in the response of PMTs by guiding light of adjustable intensity directly into the PMTs and measuring their gain + electronics response (C_{LASER}). Calibrations are taken concurrently with data collection during the 7 μs gap of each orbit between the last and first bunch trains. After a Cs scan the constant C_{LASER} is equal to 1 by definition. The subsequent drift in PMT gain over the next month is generally less than 0.5%.

Charge Injection

The charge injection system (CIS) derives a calibration factor C_{CIS} between the PMT current and the number of counts measured by an analog-to-digital converter (ADC). Electric pulses of a range of known charges are injected into the electronics. CIS calibrations are performed twice per week during data-taking. Calibration factors are stable to within 0.02% overall, with less than 1% of channels requiring recalibration above the CIS systematic error of 0.7%.

The calibration of distinct regions in TileCal allows detector problems to be quickly identified and corrected. The measured energy (E) is derived from the digital readout counts (A) as a combination of the calibration constants:

$$\mathrm{E[MeV]} = \mathrm{A[ADC]} \times C_{CIS} \left[\frac{\mathrm{pC}}{\mathrm{ADC}}\right] \times C_{TB} \left[\frac{\mathrm{MeV}}{\mathrm{pC}}\right] \times C_{LASER} \times C_{Cs} \tag{3.4}$$

The variation in response between a cell close to the beamline (A13), subject to greater radiation, and a more distant cell (D5) over the course of 2015 data-taking can be seen in Figure 3.14. The response variation grows as luminosity is collected and is primarily driven by drift in the PMT, reaching 2.5%. A minor separation of 0.5% appears between the LASER calibration and the scintillator-sensitive minimum bias and cesium calibrations during periods of largest integrated luminosity gain in late October.

Overall the TileCal provides a linear response to jets down to energies of 20 GeV. In test beams [58] the response resolution (Eq. 3.2) for the TileCal stochastic and constant terms

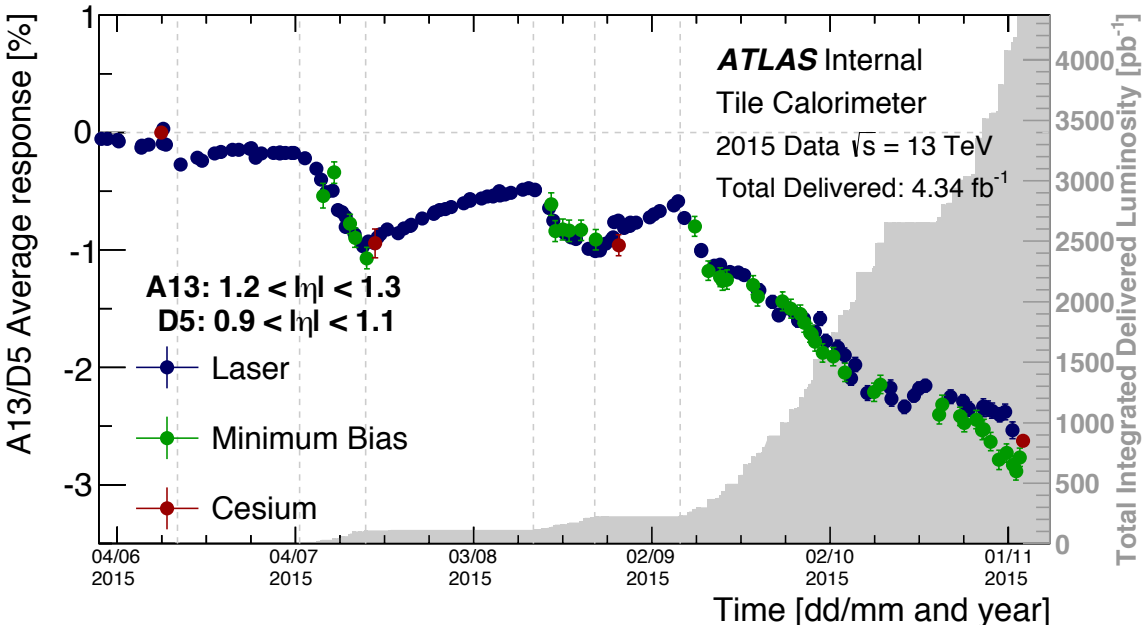

Figure 3.14: Variation in the response of cell A13 ($1.2 < |\eta| < 1.3$) and D5 ($0.9 < |\eta| < 1.1$) during Run 2 as measured by the LASER (blue circles), cesium (green squares), and minimum bias (red squares) systems, showing good agreement across calibration methods.

were measured, revealing an energy resolution of the form

$$\frac{\sigma_E}{E} = \frac{52.9\%}{\sqrt{E}} \oplus 5.7\% \tag{3.5}$$

Hadronic end-cap calorimeters (HEC) extend the range of the hadronic calorimeter between $1.5 < |\eta| < 3.2$. Each end-cap is composed of 2 wheels with copper plate absorbers oriented perpendicular to the beam line. Similar to the EM calorimeters, LAr is used as the active material with readout electrodes gathering ionization charge. The HEC has a granularity of 0.1×0.1 $(\eta - \phi)$ in the first wheel and 0.2×0.2 $(\eta - \phi)$ in the second.

The forward calorimeter (FCal) [59] covers $3.1 < |\eta| < 4.9$ and is instrumented with LAr to handle the high radiation. It contains three wheel segments of copper and tungsten absorber interspersed with readout electrodes to gather the ionization charge.

3.2.5 Muon Spectrometer

The muon spectrometer (MS) surrounds the calorimeters and is the outermost subdetector of ATLAS. It is dedicated to measuring the position and momenta of muons that pass through the ID and calorimeters. The MS was designed to measure the momentum of muons above 5 GeV and to provide a resolution of 3% at 100 GeV. It consists of 3 concentric cylinders in the barrel region from a radius of 5 m to 10 m with a small gap at $|\eta| = 0$ for service cables. Four wheels cover the end-cap, extending coverage up to $|\eta| < 2.7$. Within the spectrometer a magnetic field of between 0.5 and 1 T bends charged particle tracks and allows an accurate measurement of muon momenta.

Two types of precision chambers are used to measure position and momenta: the monitored drift tubes (MDT) [60] and the cathode strip chambers (CSC) [61]. The MDT covers most of the MS pseudorapidity range and consists of 3 cm diameter drift tubes containing a mixture of 93% argon and 7% CO2. A single tungsten-rhenium wire operated at a voltage of 3 kV lies within each tube and facilitates measurement of the drift time of the ionization charge produced by incident particles. The spatial hit resolution of a single tube is below 100 μm and is extended to approximately 50 μm through the use of either 3 or 4 layers of tubes in each chamber, depending upon its position in the detector.

The CSC is a multi-wire proportional chamber with a higher precision than the MDT in the region of $2 < |\eta| < 2.7$, where the background is larger. The radially oriented wires are held 2.5 mm away from each strip cathode and are held at a potential of 1.9 kV. The CSC detector offers a tracking resolution in the bending plane of 60 μm and is used as the first layer of the MS due to its higher radiation tolerance.

The precision chambers have a relatively long charge collection time, reaching 700 ns for the MDT and 40 ns for the CSC. Two dedicated trigger chambers therefore provide fast measurements for use in trigger decisions. Resistive plate chambers (RPC) [62] provide finer spatial resolution and are used in the barrel region of $|\eta| < 1.05$. The RPC consists of parallel electrode plates 2 mm apart and filled with a gas mixture of $C_2H_2F_4$. They are operated at a potential difference of 9.8 kV, resulting in a timing resolution better than 2 ns. Thin gap chambers (TGC) [63] provide better radiation hardness and are used in the end-caps up to $|\eta| < 2.4$. The TGC consists of multi-wire proportional chambers with a gas mixture of CO_2 and n-C_5H_{12}. While similar to the CSC, the anode wires are held only 1.4 mm away from

each strip cathode and held at a potential of 2.9 kV, providing a timing resolution of about 4 ns.

The toroid magnets provide a magnetic field of 0.5 to 1 T in the azimuthal plane, bending muons in the R-ϕ plane. Eight rectangular coils in the barrel cover $|\eta| < 1.6$ and eight coils in each end-cap cover $1.4\,|\eta| < 2.7$. The coils consist of a mixture of aluminum, copper, niobium, and titanium and are cooled with liquid helium to 4.5 K. The non-uniformity of the magnetic field limits the muon p_{T} resolution of the MS [64].

3.2.6 Data Acquisition

The high luminosity of the LHC produces far more interactions than can be recorded and requires a sophisticated system for selecting and reconstructing events. The Trigger and Data Acquisition system recognizes and saves only the most interesting events, typically with large E_{T}, through a sequential series of increasingly strict filters [65].

The ATLAS trigger system begins with a hardware-based level 1 (L1) trigger using coarse measurements from the calorimeters and muon systems. It accepts events at a 100 kHz rate and is built for speed rather than precision measurements. A combination of calorimeter and MS information is used to identify events with high energy leptons, photons, and jets as well as large momentum imbalances indicative of missing transverse energy. Muon triggers at L1 are based on a coincidence of hits among several layers of the trigger chambers. Electrons and photons are triggered on energy deposits in the EM calorimeter, limited to its fine segmentation in $|\eta| < 2.5$. Jet candidates are constructed at L1 from coarse calorimeter towers made of trigger-elements using a sliding window algorithm. A trigger-element is defined as a sum of cells in a 0.2×0.2 $(\eta - \phi)$ region, and the sliding window examines the total E_{T} against a trigger threshold value in a 4×4 region of trigger-elements.

The L1 is followed by the software-based high-level trigger (HLT) operating at 1 kHz. During Run 1 the HLT consisted of the level 2 (L2) trigger followed by the event filter. The L2 trigger performed similar measurements as the L1 trigger but with a finer granularity and ID measurements for regions of interest. The event filter fully reconstructed the event, including offline tracking and jet reconstruction, and applies stricter criteria for passing events. During Run 2 the L2 trigger and event filter were merged into a single architecture, simplifying development and reducing the CPU and network consumption [66].

Various criteria are used to decide which events pass the L1 and HLT triggers, such as the p_{T} and η of reconstructed objects or the calculated missing E_{T} of an event. For each set of criteria a unique trigger exists. If the number of events passing a specific trigger is expected to be larger than the allocated bandwidth the trigger is prescaled and only a specific fraction of the passing events are saved. Triggers that are more stringent in their selection are unprescaled and are able to save all passing events.

Event reconstruction is performed using the ATLAS Athena control framework [67]. Most events passing the HLT are written to the "main" analysis stream, while a few events which require a larger processing time are saved to a "debug" stream for future reprocessing. Data is periodically reprocessed to reflect increased understanding of detector conditions or to conform with software updates. Recorded events are analyzed for data quality and those occurring during periods of subdetector malfunction are flagged for removal from analysis.

The luminosity of the proton beams decreases as collisions progress, causing data collection conditions to vary as a function of time. Data is therefore collected in time intervals of 1 minute, referred to as lumi-blocks. Luminosity blocks are each assigned an integrated luminosity depending upon detector conditions averaged over that lumi-block. They are also useful for isolating problematic data which may have been taken while a subdetector was inoperative, allowing their easy rejection during data analysis.

CHAPTER 4
EVENT SIMULATION

A search for new physics requires a description of what is expected given the current understanding of particle physics. An accurate understanding of both SM processes and the detector response to SM particles is vital for identifying inconsistencies. Simulated data can be used to predict the outcome and sensitivity of an analysis, identifying the most promising analyses given a set amount of data. These fake datasets can help inform the parameter space of interest without biasing a study by using real data. They allow analysis techniques to be developed and adjusted before they are applied to real data. Simulated data also provides a comparison for ensuring that the reconstruction and calibration methods for physics objects are sensible.

While information on the momentum, quantum numbers, and particle type must be inferred in data from the detector response, it can be directly assigned in MC simulation as an extra layer of variables called the truth information. Truth information is useful for directly calculating the efficiency and accuracy of particle identification and measurement methods. Simulated data, while not a flawless reproduction of data, is essential for finding any inconsistencies in the analysis methods and data processing while providing benchmarks for analysis expectations.

Simulated data is derived through the Monte Carlo (MC) method which generates data based on a random sampling of SM expectations. The SM expectations are derived from current theoretical knowledge as well as extensive fine-tuning using data from similar experiments or previously collected by ATLAS. A good MC simulation will cover all aspects of particle evolution detailed in Section 2.1, including matrix element calculation, hadronization and showering of final states, and simulation of detector geometry and response.

The dominant background in the dijet analysis is simulated according to QCD theory. A QCD MC simulation was used to inform and practice the data-driven background estimation strategies, as described in Section 4.1. The procedures used to identify any new physics or set limits on its existence require the MC simulation of benchmark signals models, described in Section 4.2. Uncertainties in the simulation are quantified and propagated to the final result, as described in Section 4.3. MC simulation was used extensively to ensure a high level of data quality and good performance of the calibrated physics objects, as is later described

in Section 6.3.1.

4.1 QCD Simulation

An accurate understanding of QCD processes is integral to a large number of analyses in hadron collider physics, and a great deal of attention is paid to proper simulation. Unfortunately QCD is challenging to model, requiring higher order perturbative corrections and extensive tuning to data. Even with higher order corrections the PDF and scale uncertainties are large as a function of jet p_{T} [68], unnecessarily reducing sensitivity to possible new physics at high masses. For this reason the QCD background is modeled using data-driven background estimate, detailed later in Section 7.1. A proper understanding of the QCD background is nonetheless essential for performing data quality cross-checks and informing analysis decisions before any data is collected.

4.1.1 The Pythia Generator

The simulation of QCD processes is performed with Pythia 8.186 [69], a leading order MC generator which performs many of the steps of MC simulation. The PDF of colliding partons is determined according to the NNPDF2.3 LO PDF set [23], a parametrization of the expected PDF at 13 TeV that has been tuned using previous hadron collider data, including 36 pb^{-1} of ATLAS inclusive jet data at 7 TeV. Hard scatter QCD processes are calculated according to leading order perturbative matrix elements. They are therefore exactly calculated for $2 \to 2$ interactions, with interactions involving third partons simulated at the next step of parton evolution.

The evolution of the partons is then simulated, focusing on the parton showering of the initial and final states. For the QCD samples the renormalization and factorization scales are equated to the average p_{T} of the two leading jets. The showering of partons into complex final states is modeled through simple parton branchings following DGLAP evolution formalism [70] and calculated for individual partons sequentially according to their p_{T} ordering. Parton showering also includes effects from multiple parton interactions within the colliding hadrons and preserves the correlations between p_{T}, flavor, and color of beam remnants, the partons not directly participating in collisions.

Hadronization follows the Lund string fragmentation model [25] and is followed by the

decay of unstable particles. Due to the relatively low energy scale at which partons hadronize the calculations are practically non-perturbative and rely heavily on tuning to previous data. Parameters involved in the modeling of parton showering, hadronization, and multiple parton interactions have been tuned to previous data collected by ATLAS at $\sqrt{s} = 7$ TeV. The tuning focuses on jet-based observables including the underlying event, jet structure, and jet emissions and is collected into the A14 tune [71].

The response of subdetectors to particles is simulated using the GEANT4 toolkit [72,73]. The GEANT4 toolkit simulates the interaction of particles with all parts of the detector, including readout electronics, accounting for the various interaction lengths of detector material as well as the lifetime and branching ratio of incident particles. The exact description of geometry and material in the detector is tuned using initial test beam data [58], secondary interactions [74], and alignment methods based on collisions and cosmic muons [75,76]. The ATLAS Simulation Infrastructure [77] interfaces the MC generation and simulation packages and facilitates validation and performance checks.

In-time and out-of-time pile-up consisting of lower energy interactions that occur simultaneous to the hard scatter of interest is modeled through the overlay of minimum bias events. Pile-up events are randomly drawn following a Poisson distribution about the average number of collisions per bunch crossing ($\langle\mu\rangle$) expected in 2015 data-taking conditions. To accurately model the pile-up conditions, the events in the MC samples should be reweighted according to μ in each event, such that the final μ distributions are identical. Pile-up often consists of jets below 50 GeV that may increase the jet multiplicity of an event or deposit extra energy near higher p_{T} jets from the hard scatter, increasing their measured energy. The jets used in this analysis are of sufficiently high p_{T} that the effects of pile-up are negligible, and pile-up reweighting is not performed.

The NLO MC generator Powheg+Pythia 8.1 was also explored for use in background estimation and performance checks. As the matrix element is calculated to NLO precision it is expected to perform as well or better than the LO Pythia 8.1 generator, especially in events where the third jet carries a significant fraction of the total momentum. However large mismodeling in the response of subleading jets was found, as shown in Figure 4.1, and the use of Powheg+Pythia 8.1 was subsequently abandoned for this analysis. After future tuning of Powheg+Pythia 8.1 it will likely be used as default for future iterations of the dijet search.

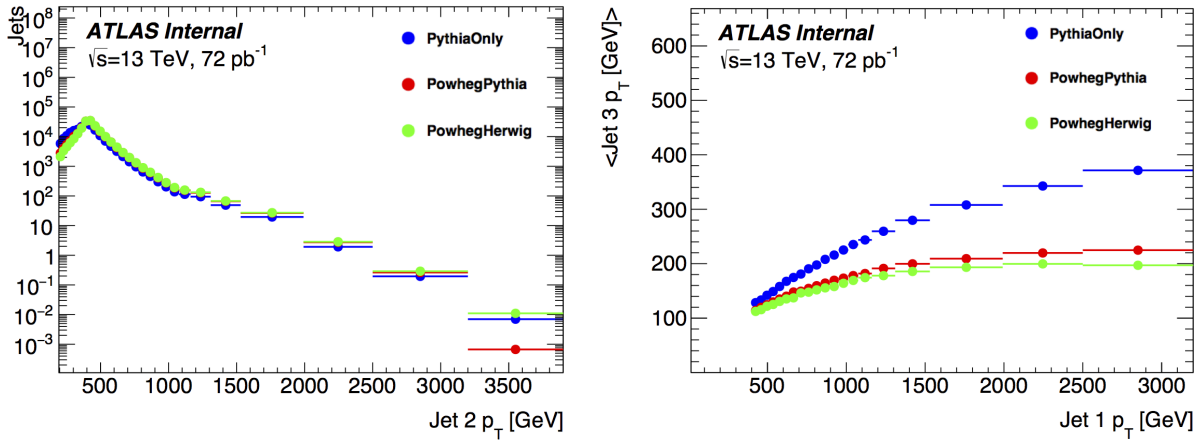

(a) (b)

Figure 4.1: Mismodeling seen in the POWHEG generator when showered with either PYTHIA 8.1 (red) or HERWIG++ (green) for the p_{T} spectrum of the second jet (a) and the profile of the 3rd jet's p_{T} as a function of the leading jet p_{T} (b). Data was shown to be in good agreement with the PYTHIA 8.1 only results (blue).

4.1.2 Monte Carlo Production

QCD samples generated at 13 TeV span a large range in cross section over the spectrum of relevant jet p_{T}. To allow for a suitable statistical precision over the full p_{T} range the generation of samples is split into slices according to the p_{T} of the leading jet [78]. Previous slicing performed on Run 1 samples were too wide and had an undesirable drop in differential cross section across the width of individual slices. For Run 2 the number of p_{T} slices has been increased and their boundaries refined, improving generator performance and statistical precision in low p_{T} slices. Ten slices, detailed in Table 4.1, are independently generated, reweighted, and combined, providing a smooth and accurate QCD prediction of the dijet invariant mass spectrum.

The production of PYTHIA 8.1 samples according to the expected detector conditions of Run 2 is referred to as MC15a. Two independent sets of MC15a samples were generated with a bunch spacing of 25 ns and 50 ns, with the former used for early analysis studies. A third configuration of MC15a samples generated with a bunch spacing of 25 ns and larger beam size (β^*) was created to match LHC beam conditions for the first week of data collection. The primary difference between samples arises from the level of pile-up, which typically affects the number and kinematics of jets below 50 GeV. High-p_{T} jet distributions are fairly

Sample Name	Leading Jet p_{T} Range [GeV]	Cross-section [fb]	Effective Luminosity [fb^{-1}]
JZ0W	0 to 20	7.84E+13	2.49E-08
JZ1W	20 to 60	7.84E+13	3.79E-05
JZ2W	60 to 160	2.43E+12	2.46E-03
JZ3W	160 to 400	2.65E+10	2.09E-01
JZ4W	400 to 800	2.55E+08	1.48E+00
JZ5W	800 to 1300	4.55E+06	4.74E+02
JZ6W	1300 to 1800	2.58E+05	8.24E+03
JZ7W	1800 to 2500	1.62E+04	3.12E+05
JZ8W	2500 to 3200	6.25E+02	3.14E+05
JZ9W	3200 to 3900	1.96E+01	8.45E+06

Table 4.1: PYTHIA 8.1 dijet samples are simulated at different cross sections within a series of p_{T} intervals for the leading jet. The effective luminosity corresponds to the number of events generated for a given sample and is inversely proportional to the cross section.

insensitive to pile-up, and no significant discrepancies were expected, or seen, between 25 ns MC15a, 50 ns MC15a, and 25 ns large β^* samples.

4.2 Signal Models

Dedicated MC generators are used to simulate events for the various signal model benchmarks presented in Section 2.2. Signals are used to inform analysis decisions and set limits on BSM physics models which may vary in their predicted cross section, signal shape, and p_{T} region of interest. The following sections detail the MC simulations used for each signal model.

4.2.1 Excited Quark

Excited quark (q^*) [37] production could arise as a consequence of quark substructure and has served as a traditional benchmark model in dijet resonance searches for many decades. PYTHIA 8.1 is used for the event generation of samples using the A14 tune [71] and NNPDF2.3 PDF set [23]. Light flavor (u, d) and heavy flavor (b) quarks are simulated at a compositeness scale set to the q^* mass and quark-like SM couplings are assumed. All possible final states are allowed, including qg, qγ, qW, and qZ. Mass points are generated at 0.5, 0.6, 0.8, 1, 2, 2.5, 3, 3.5, 4, 4.5, 5, 5.5, 6, 6.5, and 7 TeV. The cross section and acceptance for each generated mass point are shown in Figure 4.2. The behavior of the

acceptance is driven by the analysis selections detailed in Section 6.1, with a turn-on at low masses due to the single jet p_{T} selection and a plateau below 100% due to the y^* selection (Eq. 6.1 of Section 6.1).

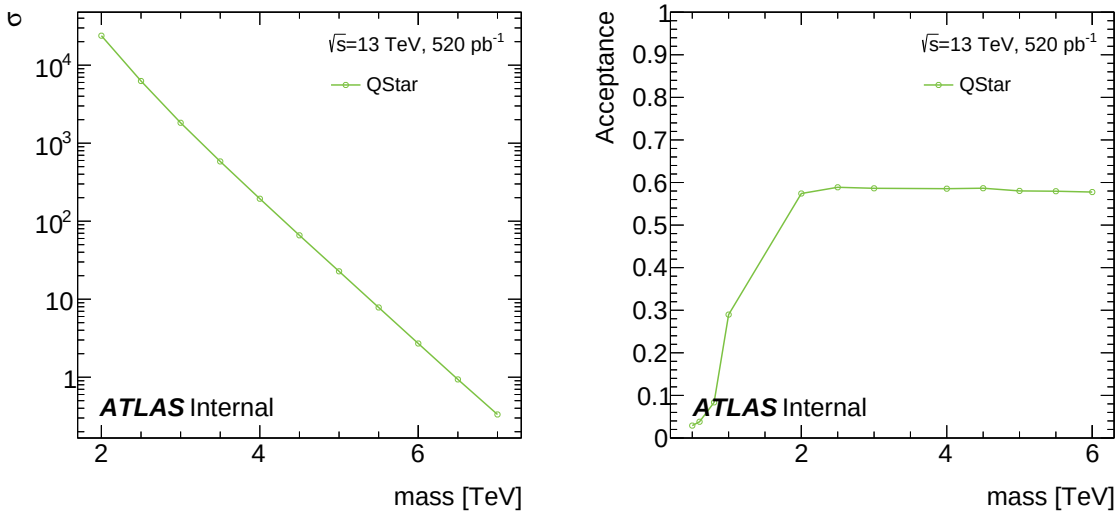

(a) (b)

Figure 4.2: Cross-section (a) and analysis acceptance (b) for excited quark samples at various mass points. Analysis acceptances are after the full event selection described in Section 6.1.

4.2.2 Dark Matter Mediators

The existence of dark matter is experimentally well motivated and is a leading candidate for BSM searches. While dark matter particles may not interact directly with the SM, mediators may provide a link between the dark matter and SM groups. The signal model studied by this analysis is of a spin-1 leptophobic particle Z' [79] that mediates interactions between SM partons and Dirac fermion dark matter particles through axial-vector couplings, extending the SM with a simple U(1) gauge symmetry. Both the mediator Z' and SM partons are assumed to have charges under this new group. The model is particularly interesting for dijet final states which cover the parameter space where Z' decays to invisible particles are kinematically suppressed [80]. This parameter space cannot be probed by typical missing E_{T} analyses which search for missing energy from the invisible decay.

The parameters of interest in the Z' model are the mass of the mediator ($M_{Z'}$), the mass

of the dark matter fermion (M_{DM}), and the coupling of Z' to dark matter fermions (g_{DM}) and to quarks (g_q). Both M_{DM} and g_{DM} have second order effects on the Z' decays and are held at $M_{DM} = 10$ TeV and $g_{DM} = 1.5$. More relevant are the mediator mass $M_{Z'}$, which drives the location of the excess, and the SM coupling g_q, determining the intrinsic cross section and width of the resonance.

The choice of $M_{Z'}$ and g_q values used in MC simulation were determined through sensitivity studies using early 80 pb^{-1} results. Z' samples from 1 to 3.5 TeV, in steps of 0.5 TeV, were initially generated with $g_q = 0.1$. Distributions for stronger couplings were estimated by scaling the sample cross section by g_q^2. The smallest value of g_q that was predicted to be excluded by the full luminosity was found, and samples were generated at this value as well as ± 0.1 and ± 0.2 about this value. Masses above 3.5 TeV were not used as the required coupling of g_q reached unity, leading to large widths on the order of 40% $M_{Z'}$ and introducing significant interference effects with the SM that were not properly simulated. The list of relevant $M_{Z'}$ and g_q values used in signal generation is found in Table 4.2.

Cross section and analysis acceptances as a function of $M_{Z'}$ for several values of g_q are shown in Figure 4.3. A slight downturn in acceptance for higher mass samples is evident and is due to the steeply falling PDF which causes significant off-shell production and introduces low mass tails. For these higher mass samples the probability of collisions between lower momentum partons is significantly larger below the production threshold, more than offsetting the reduced cross section of off-shell Z' production.

$M_{Z'}$ [GeV]	g_q				
1500	0.1	0.2	0.3		
2000	0.1	0.2	0.3	0.4	
2500	0.1	0.2	0.3	0.4	0.5
3000	0.1	0.2	0.3	0.4	0.5
3500	0.1	0.2	0.3	0.4	0.5

Table 4.2: Z' samples generated in g_q and $M_{Z'}$

4.2.3 Heavy Boson

A heavy charged gauge boson W' can arise in Sequential SM theories and are motivated by recent searches reporting 2.5 σ excesses in the effective mass spectrum of pairs of gauge bosons [81]. W' signal samples are generated with PYTHIA 8.1 using the A14 tune [71]

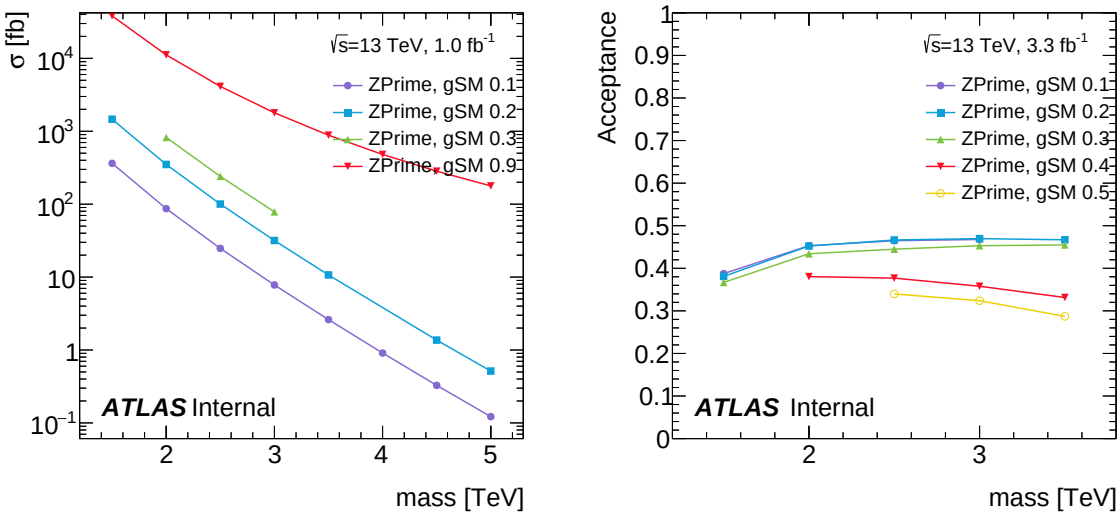

(a) (b)

Figure 4.3: Cross-section (a) and analysis acceptance (b) for Z' samples at several g_q and at various mass points. Analysis acceptances are after the full event selection described in Section 6.1.

and NNPDF2.3 PDF set [23]. The signal is assumed to have SM-like V-A couplings with decays restricted only to quarks of any flavor. Signal samples are generated in 0.5 TeV steps between 1 and 6.5 TeV with additional samples generated at 1.2 and 1.7 TeV to provide better accuracy in the region of previous limits. Cross section and analysis acceptances are shown in Figure 4.4. Similar to the Z' model, PDF effects induce a large low mass tail in high mass samples, leading to reduced acceptances.

4.2.4 Quantum Black Holes

Models of BSM physics associated with large extra dimensions were tested using QBH signals. Both the one extra-dimensional and six extra-dimensional theories were explored. QBH signals were generated with $M_D = M_{Th}$ at masses between 4 and 10 TeV, sampled at steps of 0.5 TeV. The six extra-dimensional theory was tested with two separate MC generators which vary the details of QBH production and decay, BlackMax and QBH.

The BlackMax generator [82] simulates two-body decays of QBHs according to the available degrees of freedom, similar to the semi-classical kinematics of black hole decay. The decay products are chosen by integrating over black-body distributions, giving the ap-

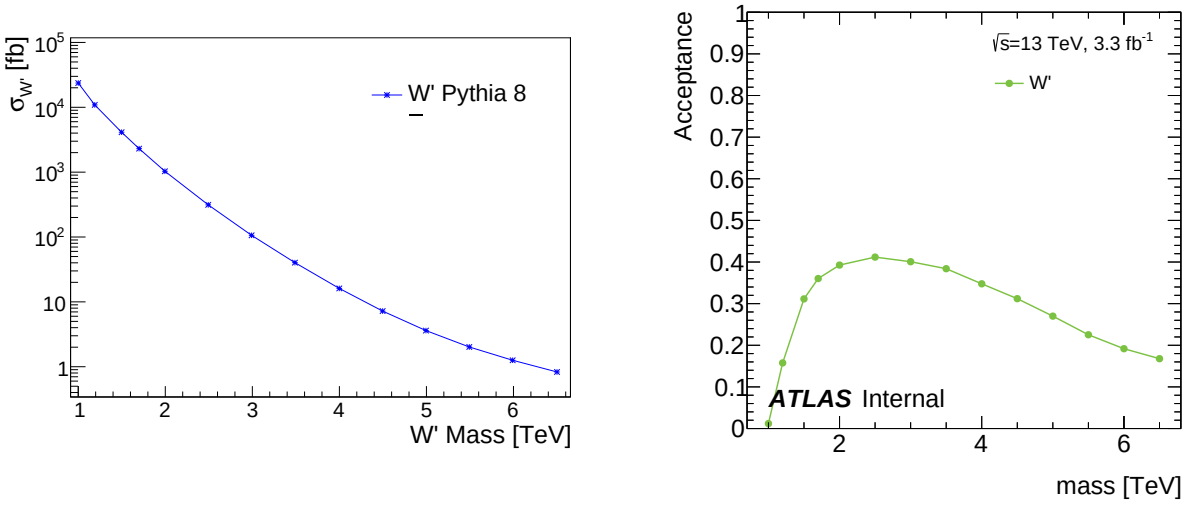

(a) (b)

Figure 4.4: Cross-section (a) and analysis acceptance (b) for W' samples at various mass points. Analysis acceptances are after the full event selection described in Section 6.1.

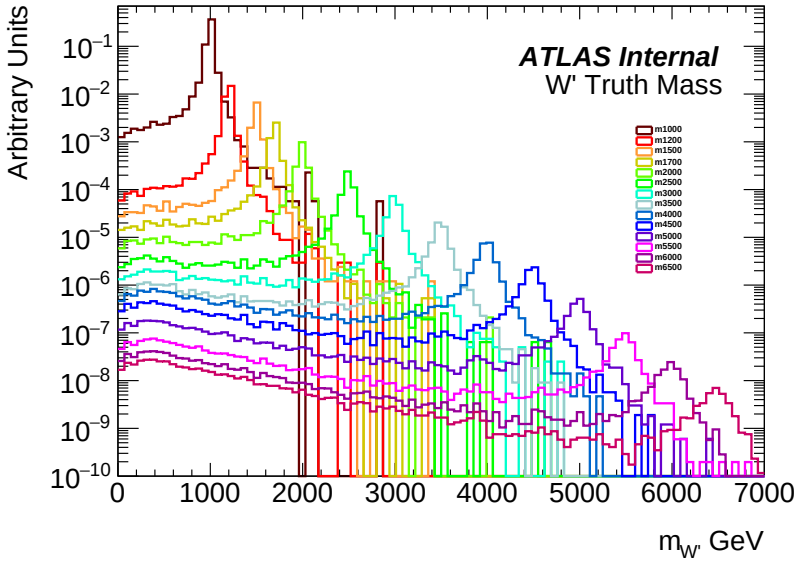

Figure 4.5: Truth level mass of W' events for various mass points. The long low mass tails of large mass points is caused by off-shell production, leading to reduced acceptance seen in Figure 4.4(b).

propriate fractions of decay into fermions and bosons. The generator provides a realistic model of QBHs at hadron colliders by accounting for the rotation of the black-hole, fermion

splitting, non-zero brane tension, and black hole recoil. QBH production begins at energies above the M_D mass threshold and does not include interference effects with QCD. BlackMax uses the CT10 [83] PDF set and interfaces to Pythia 8.1 for showering and hadronization.

The qbh generator [84] treats QBH decays non-thermally, assigning decay probabilities according to charge, color, and spin representations. Branching fractions for decay particle types are therefore calculated in advance and hard-coded into the generator. qbh also allows for multijet final states, which BlackMax explicitly rejects, but which are suppressed by this analysis through the simulation constraint $M_D = M_{Th}$. qbh uses MSTW2008LO [85] PDF sets and also interfaces to Pythia for showering and hadronization. The one extra-dimensional model is also generated with qbh.

A comparison of the BlackMax and qbh generator invariant mass distribution for several mass points is shown in Figure 4.6. The shape of the invariant mass of the two MC generators are in strong agreement, and therefore only BlackMax is used for limit setting. The cross section and analysis acceptance for the various QBH theories and generators are shown in Figure 4.7. The shape of the cross section as a function of mass is similar for all signal samples, with only differences in overall magnitude. The magnitude of the cross section is roughly 50% larger for qbh than BlackMax, primarily due to the arbitrary choice of QCD scale which is not constrained by the six extra-dimensional theory. The large difference in cross section between the one and six extra-dimensional models is driven by the difference in n_{dim}. The analysis acceptance is consistent across generators and theories and is driven by the y^* selection detailed in Section 6.1. A detailed comparison between generators is given in Appendix A.2 of Reference [86].

4.3 Monte Carlo Uncertainties

Systematic uncertainties are introduced by the Monte Carlo simulation predictions to account for limited knowledge and accuracy in simulating the physics processes. They are applied to signal templates during the limit setting phase, as described later in Section 7.3. These uncertainties are not relevant for the data-driven background estimate, which uses separate systematic uncertainties described in Section 7.1.

A systematic is applied to account for PDF and scale uncertainties in the MC simulation.

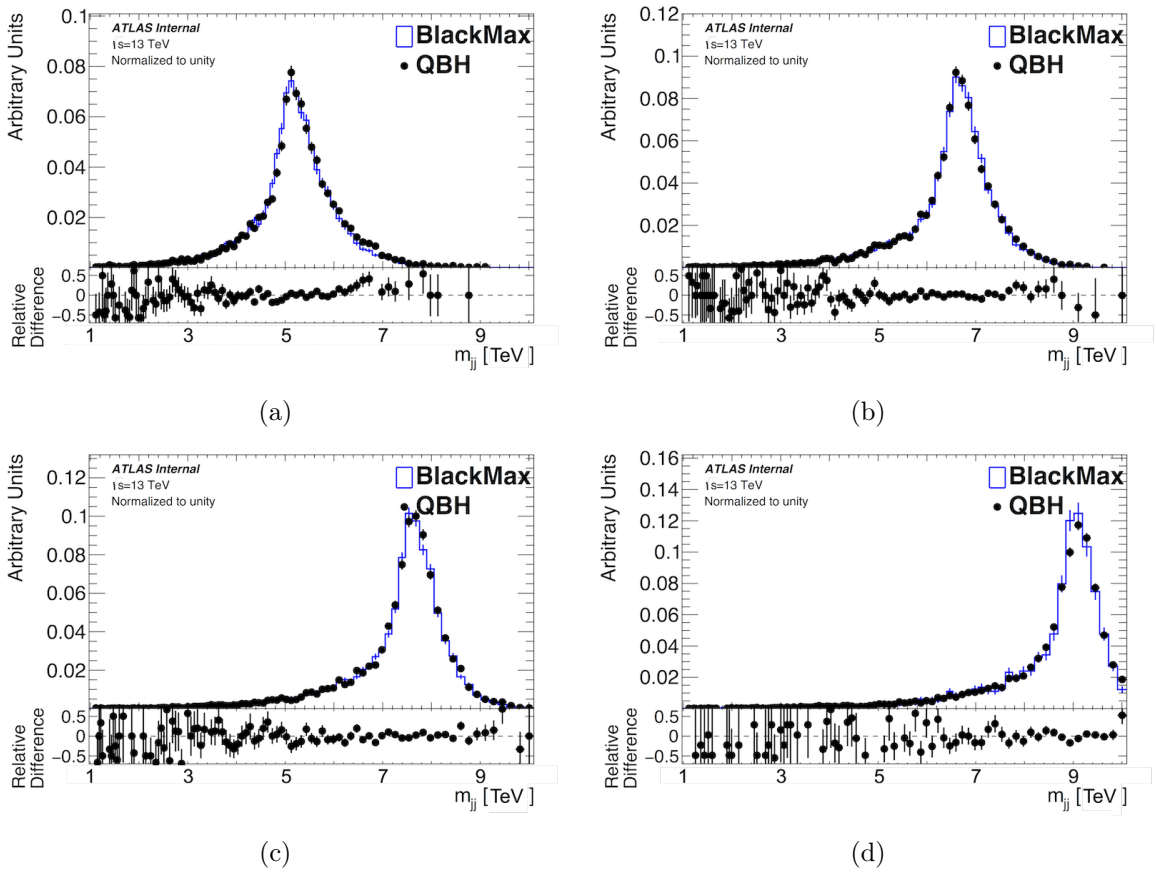

Figure 4.6: A normalized comparison of the dijet invariant mass distributions between the six extra-dimensional BlackMax and QBH generators for quantum black hole masses of (a) 5.0, (b) 6.5, (c) 7.5, and (d) 9.0 TeV. Good agreement is found between the two QBH templates, and therefore only BlackMax is used for limit setting.

The PDF uncertainty is calculated by reweighting signal sample distributions according to a different determination of the parton distribution following PDF4LHC recommendations [87]. The effect on acceptance ranges from negligible to a few percent for various mass points and is taken as an uncertainty on the signal scale. Similarly the factorization and renormalization scales are varied in the MC generator by factors of 0.5 and 2, but the effect on acceptance is found to be negligible compared to the PDF uncertainty and they are ignored.

A luminosity systematic uncertainty is applied to the MC signal normalization factor to account for an uncertainty in the cross section normalization of the data collected. A conservative uncertainty of 9% is derived from an initial calibration of the luminosity scale using x-y beam separation scans performed in June of 2015 [88]. An uncertainty on the

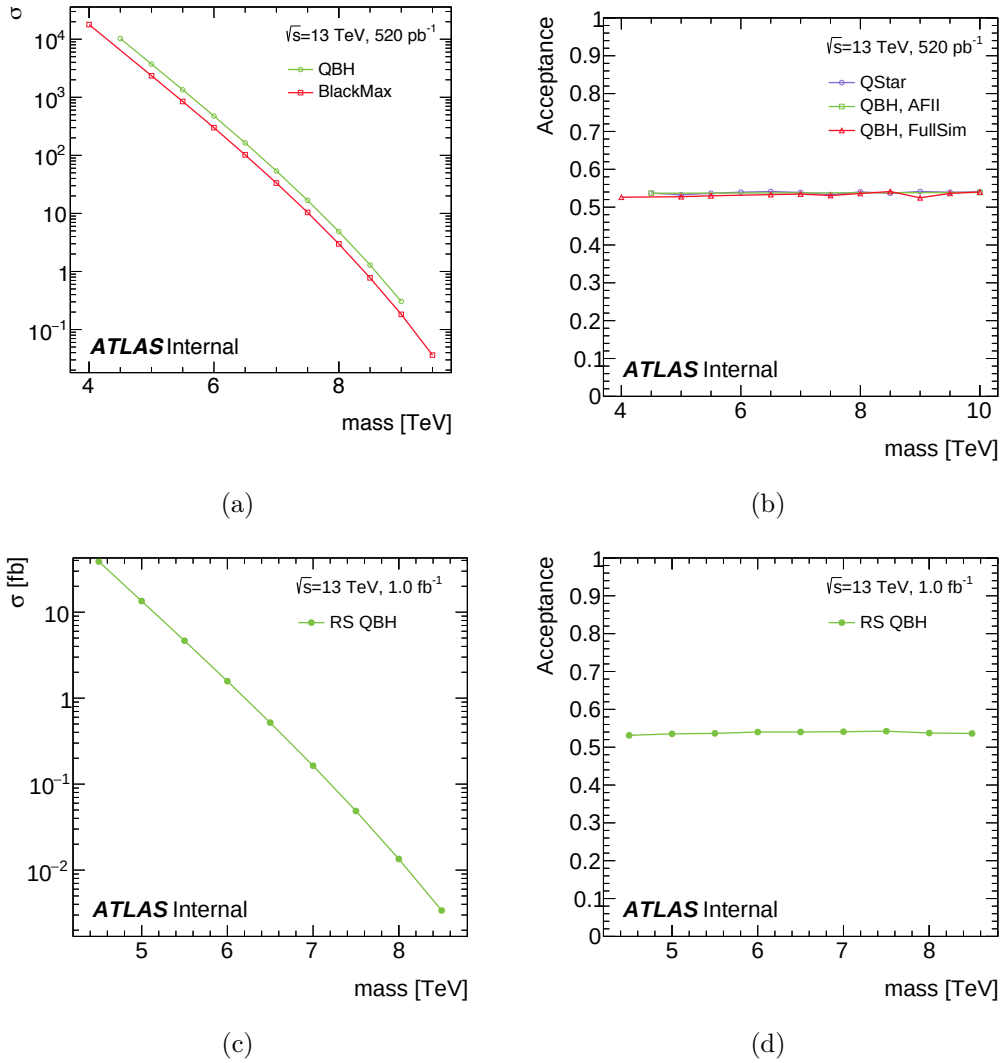

Figure 4.7: Cross-sections and analysis acceptances for six ((a),(b)) and one ((c),(d)) extra-dimensional models for several generators at various mass points. Analysis acceptances are after the full event selection described in Section 6.1.

beam energy is not included as the information is not available in MC simulations and its effect is negligible for early analyses compared with the large luminosity uncertainty.

CHAPTER 5
JET RECONSTRUCTION AND PERFORMANCE

Physics jets are the essential input to the dijet analysis. The accuracy of the analysis directly depends on the performance of the jet reconstruction and calibration. Jets from QCD processes and potential BSM resonances begin as individual quarks and gluons created from the hard scatter of hadron collisions. These partons are not directly observed in the detector, but are instead inferred from collimated showers of hadrons. The energy deposited in the finely segmented calorimeter cells by the shower constituents forms the inputs for constructing jets.

The jet four-momentum is derived from the magnitude, direction, and topology of the energy deposits through clustering methods detailed in Section 5.1. A series of calibrations described in Section 5.2 correct the jet four-momentum, built only on the energy deposited in and measured by the calorimeters, to accurately reflect the four-momentum of the initial hard scatter partons. Techniques for rejecting spurious jets are detailed in Section 5.3 while methods used to identify and trigger on events containing jets of interest are detailed in Section 5.4.

5.1 Jet Reconstruction

Jets consist of a collection of calorimeter cells with significant energy deposits from particles of a parton shower. Measuring the energy of the individual particles is not straightforward; the calorimeter responds differently to strongly interacting particles like pions and protons compared to particles interacting electromagnetically such as electrons and photons. While calorimeter cells contains components of both types of energy depositions, the jet reconstruction considers only the response at the electromagnetic (EM) energy scale, while subsequent calibrations account for strongly interacting particles.

Jets are reconstructed through clustering methods known as jet-finding algorithms [89]. Jet-finding algorithms attempt to group the many particles of a parton shower into a single four-vector representative of the direction and energy of the initial hard scatter parton. The algorithms may take a variety of inputs representing individual particles such as energy deposits, particle tracks, or truth-level particles provided in MC simulation. In ATLAS

the jets are typically formed from several topologically adjacent clusters (topo-clusters) of calorimeter cells.

5.1.1 Topo-clusters

Topo-clusters represent a collection of calorimeter cells with related energy deposits. The cells in each calorimeter form a concentric cylinder about the beam-line, providing tangential and radial position measurements of incident particles. Several calorimeter cells traversed by a single particle are joined into a single topo-cluster representative of that particle. A topo-cluster may also represent several parallel particles within the detector resolution of one another. Topological clusters are formed through an iterative procedure [90] which identifies the most significant energy deposits, the seed cells, and then clusters neighboring cells into a single topo-cluster.

Seed cells are first identified as the calorimeter cells with an energy significantly above a predefined noise threshold $|E_{\text{cell}}| > 4\sigma_{\text{noise}}$. The seed cell forms a protocluster and neighboring cells are iteratively added to it if they have an energy of $|E_{\text{cell}}| > 2\sigma_{\text{noise}}$. Once the iterative process ends and a stable protocluster is formed, all cells adjacent to the protocluster are added, independent of the magnitude of their signal. Through this method a topo-cluster is formed by a core of cells with significant energy surrounded by an envelope of cells containing any residual or leaked energy.

The jet-finding algorithms, detailed in the next section, treat the topo-clusters as massless four-vectors of magnitude $E = \sum E_{\text{cell}}$ which point from the center of the detector to the energy-weighted barycenter of the topo-cluster. The distance between four-vectors is defined as

$$\Delta_{ij}^2 = \left(y_i - y_j\right) + \left(\phi_i - \phi_j\right), \tag{5.1}$$

where y_i is the rapidity and ϕ_i the azimuthal angle of four-vector i.

5.1.2 Jet-finding

Jet-finding algorithms combine the topo-clusters which are likely to have resulted from the same initial parton. Numerous jet-finding algorithms exist with various criteria for combining topo-clusters within a predetermined radius. The most successful algorithms consider the

following rules:

Well-defined

The boundaries of a jet should be well-defined, even when two jets overlap. Algorithms that produce well-defined boundaries will assign any shared topo-clusters to only one of the overlapping jets according to their relative energy and the topo-cluster's distance to other jet constituents. Using jets with well-defined boundaries is important when correcting for the additional energy deposited by pile-up jets.

Collinear-safe

Jet formation should be insensitive to the number of particles within the parton shower. The choice of jet boundary should not be altered if a single particle is replaced by two collinear particles of half the original energy, a common result of parton fragmentation and radiation. Similarly no p_{T} threshold should be required when choosing four-vectors from the list of topo-clusters, preventing a scenario where two adjacent topo-clusters below p_{T} threshold are rejected when a single topo-cluster with the combined p_{T} would be accepted.

Infrared-safe

The definition of a jet should be insensitive to the soft radiation of the parton shower. Infrared-safe algorithms ensure that the hardest energy deposits drive jet clustering, and that soft radiation between overlapping jets does not alter the jet multiplicity of an event.

These requirements ensure that the jet reconstruction is well-defined for theoretical simulation at all orders of perturbation theory and that the jet multiplicity is relatively insensitive to the modeling details of parton showering and hadronization.

A successful series of jet-finding algorithms are the k_t algorithms [91]. These algorithms combine two four-vectors into a jet based on the p_{T} weighted distance between them, as defined in Eq. 5.2a, and between each four-vector and the LHC beam, as defined in Eq. 5.2b. Here k_{ti} is the p_{T} of input i, Δ_{ij} is the distance between inputs i and j (as defined by Eq. 5.1), R is a radius parameter the defines the size of the jet, and p is a configurable exponent.

$$d_{ij} = min\left(k_{ti}^{2p}, k_{tj}^{2p}\right)\frac{\Delta_{ij}^2}{R^2} \tag{5.2a}$$

$$d_{iB} = k_{ti}^{2p} \tag{5.2b}$$

The algorithms work by identifying the two four-vectors of an event with the smallest distance d_{ij}. If $d_{ij} < d_{iB}$ the two four-vectors are removed from the event and replaced by a single four-vector combination. The smallest distance d_{ij} between all four-vectors is then recalculated, and the sequential recombination procedure continues. If at some point $d_{iB} < d_{ij}$ for all four-vector combinations, then four-vector i is designated as a final jet and removed from the event. The procedure continues until no four-vectors remain and all inputs have been classified into jets.

The choice of p in Eq. 5.2a and Eq. 5.2b defines the combination behavior of soft radiation. A value of $p \geq 1$ creates a soft-adaptive algorithm which adapts jet boundaries to encompass soft radiation from the showering. Jets formed using a value of $p = 1$ are generally referred to as k_t jets. While k_t jets are better able to capture the evolution of hadronic showers they are more susceptible to contamination from pile-up [91]. Their irregular boundaries are dependent on soft radiation, illustrated in Figure 5.1(a), complicating the subtraction of pile-up through calibration methods, later detailed in Section 5.2.

A value of $p = 0$ combines topo-clusters purely on their angular separation, with no regard to their p_{T}. Jets formed using a value of $p = 0$ are referred to as Cambridge/Aachen jets. They are most useful when using a larger radius whose boundaries include the entire substructure of the independent showers within a jet. Their less well-defined boundaries, shown in Figure 5.1(b), may also cause calibration issues similar to k_t jets.

Jets formed with a value of $p < 0$ are referred to as anti-k_t jets, and are the jets of primary use by the ATLAS collaboration and by this analysis. The anti-k_t algorithm is soft-resilient with well-defined boundaries driven by the hard energy deposits. Calibrations are used to account for the average energy of the soft radiation excluded in anti-k_t jets. Their regular boundaries, shown in Figure 5.1(c), are less sensitive to soft radiation, facilitating the process of pile-up removal and energy calibration.

The jet radius defines the size of the jet and its choice is driven by the nature of the physics sought in the analysis. A larger R captures more of the deposited energy, particularly for

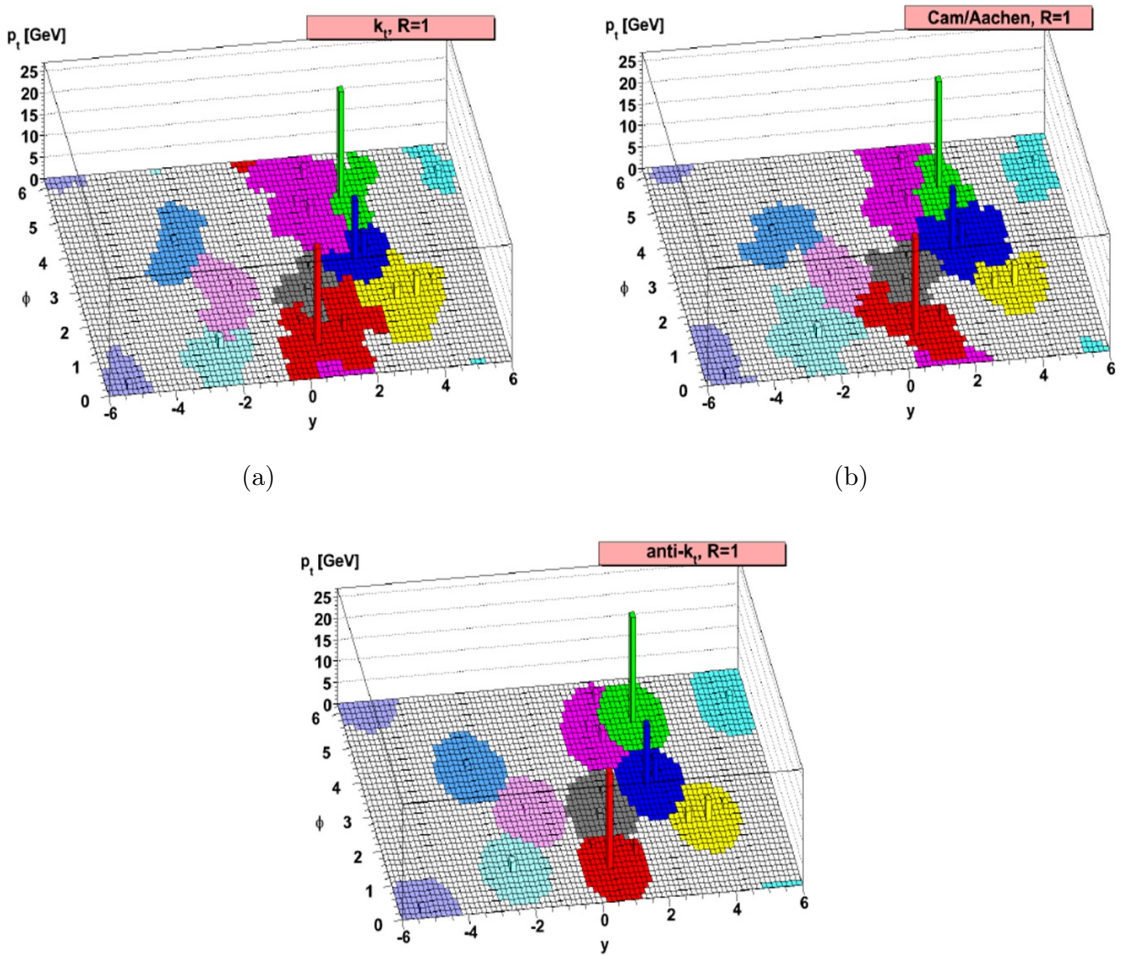

(a) (b)

(c)

Figure 5.1: Illustration of topo-cluster grouping for k_t (a), Cambridge/Aachen (b), and anti-k_t (c) algorithms. Identical topo-clusters, shown as columns of p_{T} in the ϕ-y plane, are grouped into jets of various colors according to the algorithm.

particles with wide showers, while a smaller R jet is less affected by pile-up energy or other particles in the collision. Value such as 0.4, 0.6, and 1.0 are common for analysis studies, and jets of each radius are calibrated independently using the procedures defined below. This analysis utilizes jets of the highest p_{T} which are generally very collimated and dominated by hard energy deposits. A radius parameter of R=0.4 is therefore used for the jets in the analysis.

5.2 Jet Calibration

The jets formed from topo-clusters are reconstructed at the EM scale. To correct jets to the particle-level energy of the initial parton a series of corrections are derived from both the MC simulation and from data, with the latter referred to as *in-situ* corrections [92, 93]. MC-based calibrations are derived and applied sequentially and correct the direction of the jet, the modeled response of the calorimeter, and the effects of pile-up. However MC simulation, obtained from test-beams, collision data, and theoretical considerations, is not a perfect description of the physics and detector response. *In-situ* calibrations account for any physics or detector mismodeling by correcting jet p_{T} against other well-measured physics objects.

Pile-up Correction

The pile-up corrections [92, 94] account for additional energy deposited within the jet radius from in-time and out-of-time pile-up. Pile-up is assumed, on average, to deposit energy uniformly in η and ϕ throughout the detector, providing a diffuse background that may be subtracted from individual jets. The level of pile-up is parameterized as a function of the number of primary vertices $\mathrm{N_{PV}}$, the average number of interactions per crossing $\langle\mu\rangle$, and the median energy density ρ of jets in the event. The pile-up energy is then subtracted from each jet according to it's area. Jet area is defined by ghost association, whereby "ghost" particles of infinitesimal momentum are added uniformly to an event. The relative fraction of ghost particles associated to the jet after reconstruction determines the jet area.

Origin Correction

Jet four-vectors are initially constructed to point to the geometrical center of the detector. In reality particles point back to vertices at the interaction point, identified through the extrapolation of tracks in the inner detector. The typical volume in which interactions may take place is 14 μm in the transverse direction (x and y) and 45 mm in length. Jet four-vectors are adjusted to point back towards the primary vertex, or the vertex consisting of the largest Σp_{T}^2 of tracks. The origin correction improves the angular resolution of jets while only having a small effect on jet p_{T}.

Jet Energy Scale and η Correction

A jet energy and η correction is derived from MC to correct the EM scale jets to the

true energy scale. Energy at EM scale is lower due to unmeasured energy deposited in inactive detector regions and outside of the jet radius (out-of-cone radiation), the non-compensation of the hadronic calorimeters, or reconstruction inefficiencies. The true jet p_{T}, including all showered particles except muons and neutrinos, is calculated in MC and matched to reconstructed jets through a requirement on distance Δ_{ij} (Eq. 5.1). The ratio of reconstructed jet energy to true jet energy is parameterized as a function of the reconstructed jet's p_{T} and η_{det} and its inverse is applied as an energy correction. The η_{det} of a jet is the η as measured toward the center of the detector, rather than the primary vertex, and is useful when deriving average corrections that depend on detector geometry. The magnitude of this calibration as a function of η_{det} is shown in Figure 5.2(a) for various values of E_{true}.

Following the energy scale calibration it is found that a bias exists in the η_{det} distribution of reconstructed jets with respect to truth jets. This bias, shown in Figure 5.2(b), is primarily induced by gaps and transition regions in the calorimeters. An additional η_{det} correction is applied to reduce this bias and consequentially improves the closure of energy scale correction.

Global Sequential Correction

A residual dependence of jet energy is found on longitudinal and transverse features of the jet, primarily due to differences in the shower profiles between jets initiated by quarks and by gluons. A series of independent corrections based on optimized observables form the set of Global Sequential Corrections (GSC) [92, 95]. The GSC shifts the energy of individual jets while maintaining the mean energy response derived in the previous jet energy scale calibration. The variables of interest are

1. the fraction of jet energy deposited in the first layer of the Tile Calorimeter,
2. the fraction of jet energy deposited in the last layer of the EM calorimeter,
3. the number of tracks associated with the jet,
4. the width of the tracks associated with the jet,
5. the number of muon segments associated with the jet.

Tracks and muon segments are associated to jets through ghost association (see "Pile-up Correction" earlier in this section). The width of the tracks is defined by the

p_{T}-weighted average distance Δ_{ij} between all constituent tracks and the jet four-momentum. Tracks considered are required to have $p_{\mathrm{T}} > 1$ GeV, be within the acceptance of the ID ($|\eta| < 2.5$), and pass several basic quality criteria. The final correction uses track segments reconstructed in the muon spectrometer to identify high-p_{T} jets which are not fully contained in the calorimeter, referred to as punch-through. Punch-through would otherwise produce high-p_{T} tails in the jet response distribution. An uncertainty on the punch-through correction is derived through a data-MC comparison of dijet events in which one jet is completely contained in the calorimeter, having 0 associated muon segments.

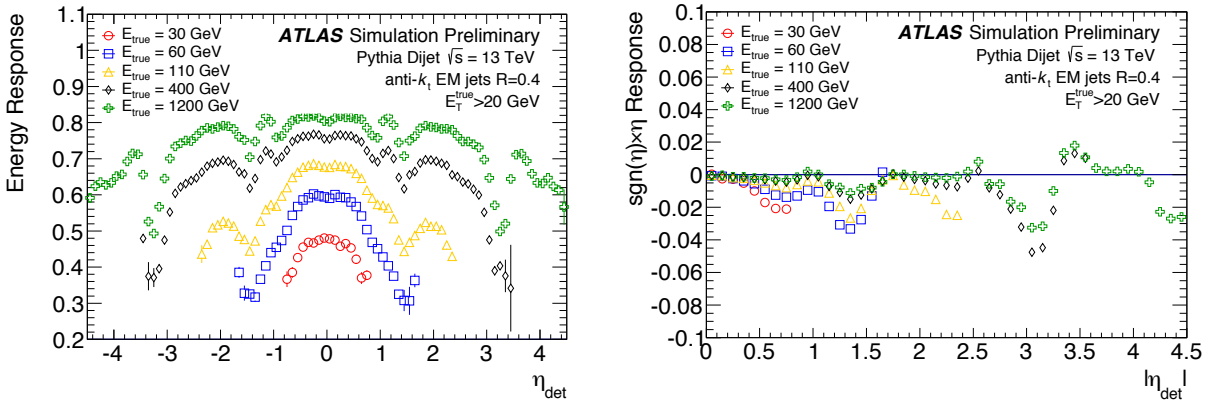

(a) (b)

Figure 5.2: Jet energy response (a) as a function of η_{det} for several values of E_{true} is derived using anti-k_t jets of R=0.4 in MC simulation. The inverse of the energy response serves as the jet energy scale calibration. An η_{det} symmetric bias exists after the calibration is applied (b), shown as a function of $|\eta_{\mathrm{det}}|$.

5.2.1 In-situ Jet Calibration

MC-based calibrations are successful in correcting the EM scale jet to the predicted particle-level energy scale but may suffer from MC mismodeling. A series of *in-situ* corrections are derived from data by balancing the p_{T} of individual jets against well-measured physics objects. The relative difference in the jet response between data and MC is taken as the correction, defined as

$$\frac{\mathcal{R}_{\text{data}}}{\mathcal{R}_{\text{MC}}} = \frac{\langle p_{\text{T}}^{\text{jet}}/p_{\text{T}}^{\text{ref}}\rangle_{\text{data}}}{\langle p_{\text{T}}^{\text{jet}}/p_{\text{T}}^{\text{ref}}\rangle_{\text{MC}}} \tag{5.3}$$

The *in-situ* corrections are derived in order, with each applying the previous calibration and propagating the relevant systematic uncertainties. They consist of:

η-intercalibration

At the hadronic scale the response of jets should be flat as a function of η, however variations can occur due to non-uniformities in the distribution of dead material and in calorimeter response. The $\eta-$intercalibration [96] corrects the response of forward jets ($0.8 < |\eta| < 4.5$) with respect to well-modeled central jets ($|\eta| < 0.8$). The calibration is derived as a function of p_{T} and η, and is shown for one p_{T} region in Figure 5.3(a).

Boson Balance

Bosons provide an independent reference that can calibrate a jet's response in events where the two objects are expected to have a balanced transverse momentum. Photons are used as reference particles as they decay into relatively narrow electromagnetic showers, which benefits their energy measurement and calibration. Z bosons that decay into leptons are also used as reference particles as their energy measurements benefit from extensive tracking information. Boson balancing [97] compares the response of central jets ($|\eta| < 0.8$) in the calorimeter against well calibrated photons ($30 < p_{\text{T}} < 800$ GeV) and Z bosons decaying to pairs of electrons or muons ($20 < p_{\text{T}} < 200$ GeV).

Multijet Balance

The multijet balance calibration [96] extends the range of photon and Z boson balancing beyond the statistics-driven limit of 800 GeV. Individual high-p_{T} jets are balanced against a collection of low-p_{T} jets which have benefited from the full calibration, including boson balancing. This procedure is repeated iteratively, with newly calibrated high-p_{T} jets being used to calibrate even higher p_{T} jets, covering a total range of $300 < p_{\text{T}} < 1700$ GeV.

The data-MC ratios derived for the boson and multijet balance calibrations are combined into a single correction over the full jet p_{T} range as shown in Figure 5.3(b). A weighted average between measurements is found through χ^2 minimization, with residual statistical

fluctuations smoothed with a sliding Gaussian kernel method. Each source of uncertainty is treated independently, is assumed to be fully correlated across p_{T} and η, and is propagated to the final combination through pseudo-experiments. Regions of p_{T} with significant tension between *in-situ* measurements are given inflated uncertainties. If the tension, defined as $\sqrt{\frac{\chi^2}{\mathrm{dof}}}$, is larger than one, each uncertainty source is scaled upwards by the tension factor. The tension rescaling is only needed in one region near 200 GeV, as shown in Figure 5.4.

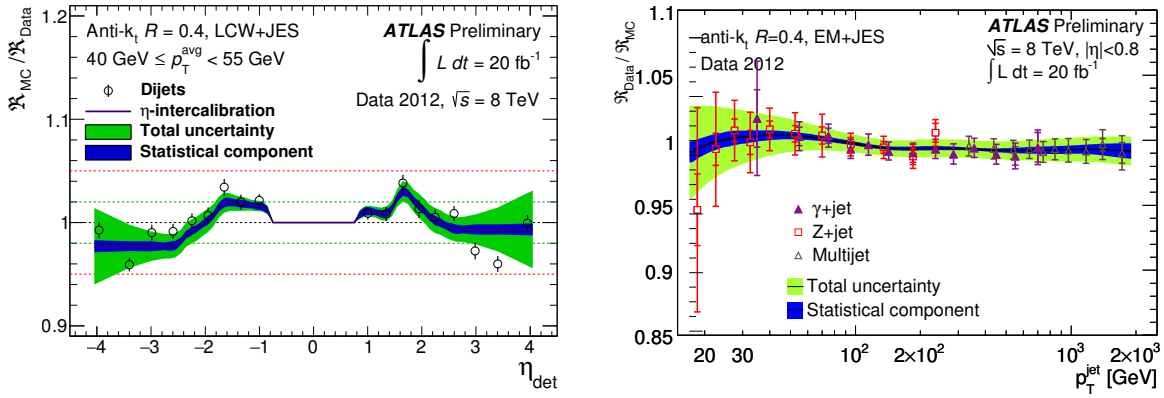

(a) (b)

Figure 5.3: Relative jet response and the total uncertainty for the $\eta-$intercalibration (a) as a function of η_{det} ($40 < p_{\mathrm{T}} < 55$ GeV) and *in-situ* balance calibrations (b) as a function of p_{T} ($|\eta| < 0.8$). The black line shows the derived calibration factor with colored uncertainty bands. The $\eta-$intercalibration calibration is 1 in the central reference region ($|\eta| < 0.8$) by design.

5.2.2 Single Particle Response

The performance of the *in-situ* calibrations may be compared to the estimated jet energy scale from the response of single hadrons [98–100]. The calorimeter response to isolated charged hadrons is measured in data up to ∼20 GeV, and through test-beam data up to ∼350 GeV. The response of neutral pions and hadrons is also estimated, albeit with larger uncertainties. Given estimates on the response of single particles, the response of high-p_{T} jets can be derived from estimates of the particle composition within a jet, derived from MC simulation. The single particle response studies show good agreement with the *in-situ* methods [93] but with larger uncertainties of roughly 5% compared to 2%.

The *in-situ* calibrations cover energies up to 1.7 TeV, after which an extrapolation of their

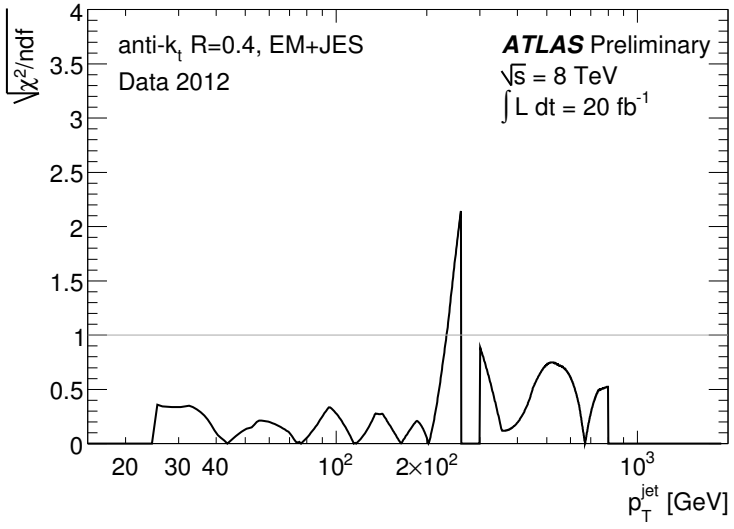

Figure 5.4: Tension ($\sqrt{\frac{\chi^2}{\text{dof}}}$) between *in-situ* measurements during the χ^2 minimization. The measurements are generally in good agreement, with a single region of minor disagreement around 200 GeV where the uncertainties are increased as a result.

calibration is required. The uncertainties on this result, which cannot be reliably measured past 1.7 TeV, are instead taken from the more conservative single hadron response studies. A breakdown of the effect on the jet energy scale from single hadron response uncertainties is shown in Figure 5.5. The dominant uncertainty arises from an extrapolation to hadron response above 350 GeV from test-beam results, where individual high-p_{T} hadrons are given a conservative 10% uncertainty to account for calorimeter saturation and non-linearities as well as hadrons escaping into the Muon Spectrometer.

5.2.3 Corrections for 2015 data

At the time of publication of the 13 TeV dijet resonance analysis the *in-situ* calibrations derived with 13 TeV data and updated MC simulations were not available. Calibrations derived at 8 TeV were instead applied after considering changes in 2015 run conditions and MC simulation [92].

The changes to MC simulation affect the MC-based calibrations preceding the *in-situ* calibrations, and include updates to

- the modeling of interactions within the detector from the QGSP model to the FTFP

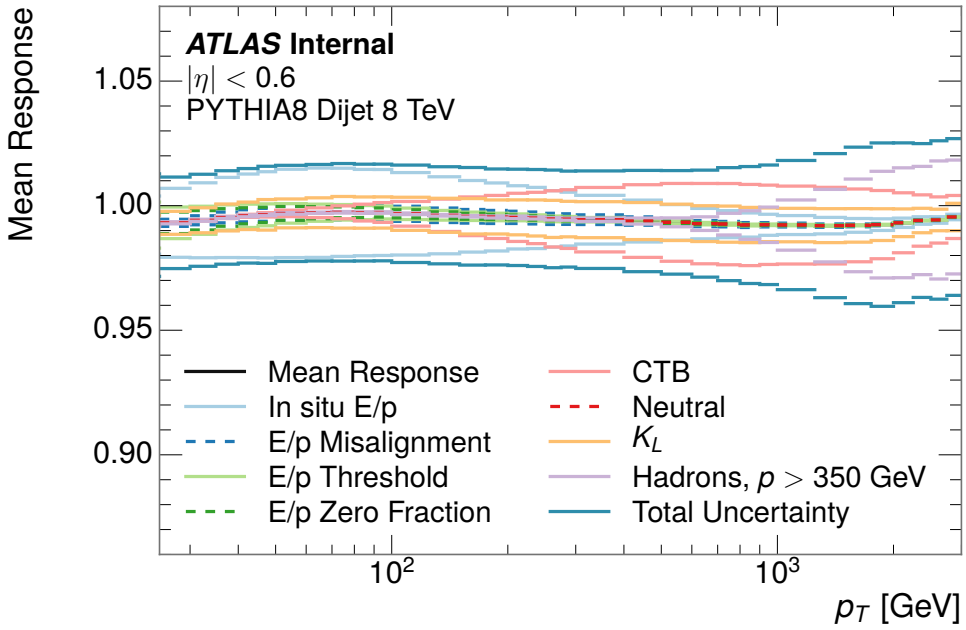

Figure 5.5: Uncertainties on the jet energy scale due to single hadron response [98]. Uncertainties account for assumptions made in the single hadron response analysis (E/p) and the combined test beam results (CTB), on the MC-based extrapolations for neutral hadrons (Neutral) and K_L (K_L), and extrapolations of combined test-beam results beyond 350 GeV (Hadrons, p > 350 GeV).

model [101],

- the MC generator tune, affecting the description of the underlying event and PDF,
- the ϕ-dependence of the Tile Calorimeter signal reconstruction.

To account for the predicted effects on the 2012 *in-situ* result, the variation in jet response is found when varying each of these updates independently, as shown in Figure 5.6(a). As these changes affect only MC simulation, and not data, a 2015 *in-situ* calibration (f_{2015}) can be computed from the original calibration (f_{2012}) according to

$$f_{2015} = \frac{R_{\text{new tune}}}{R_{\text{old tune}}} \times \frac{R_{\text{new tile sim}}}{R_{\text{old tile sim}}} \times \frac{R_{\text{FTFP}}}{R_{\text{QGSP}}} \times f_{2012} \tag{5.4}$$

and applied as a function of jet p_{T} and η.

There are also changes to 2015 run conditions which affect both data and MC simulation,

and therefore cannot be easily divided out. These differences include

- an uncertainty in the MC simulation on the underlying event due to an increased center-of-mass energy,
- a change to 25 ns bunch spacing from 50 ns,
- a change in data-taking conditions and readout settings,
- a change from the use of 5 to 4 samples in the signal reconstruction in the LAr calorimeter,
- adjustments to the noise thresholds in the topo-clustering algorithm (∼10% in the barrel region),
- an improved reduction of pile-up jets during topo-cluster reconstruction by curtailing growth in the calorimeter pre-sampler layers.

Systematic uncertainties are derived using dedicated MC samples simulating each effect. The systematic difference was calculated with respect to a reference sample and the change in scale taken as an additional source of uncertainty on the *in-situ* correction. The size of this correction as a function of true jet p_{T} is shown in Figure 5.6(b).

5.2.4 JES Uncertainty Reduction

The full list of 73 systematic uncertainties considered is found in Table 5.1. The majority (56) of uncertainties come from the 2012 *in-situ* calibrations and account for assumptions made in the event selection, MC simulation, sample statistics, and propagated uncertainties on the electron, muon, and photon energy scales. An additional 6 *in-situ* uncertainties account for the correction to 2015 conditions. One high-p_{T} uncertainty is derived from the single particle response and applied beyond the reach of *in-situ* uncertainties. Four pile-up uncertainties are included to account for potential mismodeling in MC simulation of the number of reconstructed primary vertices $\mathrm{N_{PV}}$, the mean number of interactions per bunch crossing $\langle\mu\rangle$, and the energy density in jets ρ. Three additional uncertainties account for differences in the calorimeter response and simulated jet composition of light-quark, b-quark, and gluon initiated jets. An uncertainty is also provided on the GSC punch-through correction. The full combination of these uncertainties is shown in Figure 5.7.

Z+jet	
e E-scale material	Material uncertainty on electron energy scale
e E-scale presampler	Presampler uncertainty on electron energy scale
e E-scale baseline	Baseline uncertainty on electron energy scale
e E-scale smearing	Uncertainty on electron energy smearing
μ E-scale baseline	Baseline uncertainty on muon energy scale
μ E-scale smearing (ID)	Uncertainty on muon momentum smearing from inner detector
μ E-scale smearing (MS)	Uncertainty on muon momentum smearing from muon spectrometer
MC generator	Difference between MC generators
JVF	JVF choice
$\Delta\phi$	Extrapolation in $\Delta\phi$
Out-of-cone	Contribution of particles outside the jet cone
Sub-leading jet veto	Variation in subleading jet veto
Statistical components	Statistical uncertainty
γ+**jet**	
γ E-scale material	Material uncertainty on photon energy scale
γ E-scale presampler	Presampler uncertainty on photon energy scale
γ E-scale baseline	Baseline uncertainty on photon energy scale
γ E-scale smearing	Uncertainty on photon energy smearing
MC generator	Difference between MC generators
$\Delta\phi$	Extrapolation in $\Delta\phi$
Out-of-cone	Contribution of particles outside the jet cone
Photon purity	Purity of sample in γ +jets
Statistical components	Statistical uncertainty
Multijet Balance	
α	Angle between leading jet and recoil system
β	Angle between leading jet and closest subleading jet
MC generator	Difference between MC generators
p_{T} asymmetry selection	Asymmetry selection between leading jet and subleading jet
Jet p_{T} threshold	Jet p_{T} threshold
Statistical components	Statistical uncertainty
2012→2015	
Underlying event	Change in underlying event MC simulation from QSGP to FTFP
Bunch spacing	Difference between 25 and 50 ns bunch spacing
Data-taking conditions	Update to data-taking conditions and readout settings
4-sample LAr	Switch in LAr signal reconstruction from 5 to 4 samples
Topo-clustering	Adjusted algorithm to remove PS initiated jets
Noise thresholds	Increased noise thresholds for topo-clustering algorithm
Pile-up	
μ Offset	Uncertainty in μ modeling in MC simulation
$\mathrm{N_{PV}}$ Offset	Uncertainty of $\mathrm{N_{PV}}$ modeling in MC simulation
ρ topology	Uncertainty on modeling of event energy density in MC simulation
p_{T} dependence	Uncertainty of the pile-up correction on p_{T} dependence
η − intercalibration MC	Difference between MC generators
η − intercalibration stat.	Statistical uncertainty
Flavor b-jet	Uncertainty on calorimeter response to b-tagged jets
Flavor Response	Uncertainty on calorimeter on response of gluon-initiated jets
Flavor Composition	Uncertainty on jet composition between quarks and gluons (50/50 assumed)
Punch-through	Uncertainty on GSC punch-through correction
Single hadron response	High-p_{T} jet uncertainty from single hadrons and test-beam

Table 5.1: Summary of the systematic uncertainties in the jet energy scale [102].

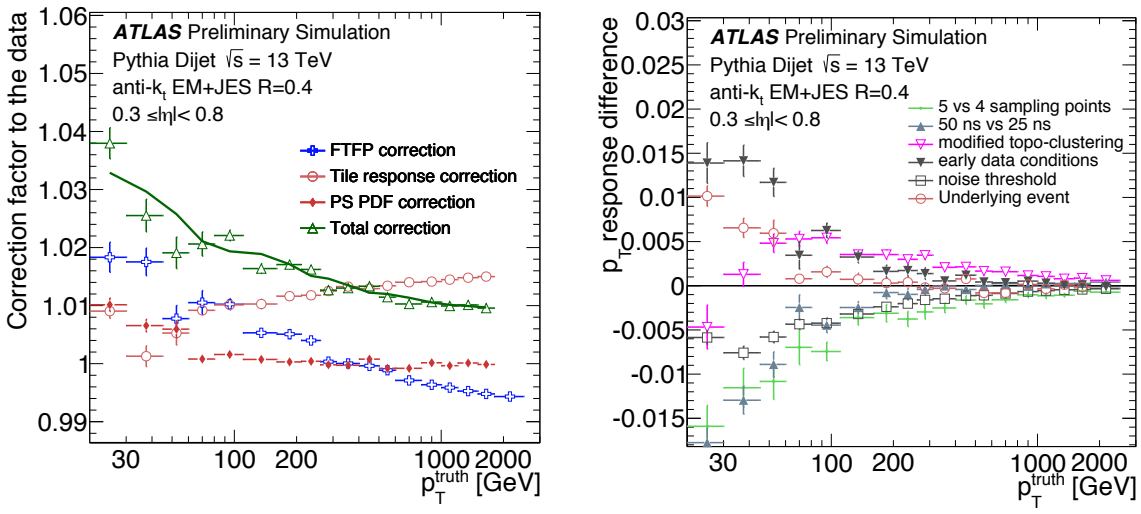

(a) (b)

Figure 5.6: Corrections to the 2012 *in-situ* calibration (a) due to changes to the MC simulation in 2015. Additional systematic uncertainties (b) are considered due to differences in data-taking condition between 2015 and 2012.

As the background estimate is data-driven, the JES uncertainties are applied only to the signal models during the limit setting phase, described in Section 7.3. For the dijet analysis (as with many others) a full accounting of all 73 systematic variations is impractical and provides a negligible improvement to limit-setting precision. To simplify the analysis a set of reduced nuisance parameters (NPs) are derived. However each uncertainty may have a degree of correlation with each other uncertainties that varies with p_{T} and η, and any reduction in the number of NPs can lead to a loss of correlation information. The reduced NPs are derived so as to maintain the bulk of the jet-jet correlations in targeted p_{T} and η regions.

First an eigenvalue decomposition is performed [93] using the 62 *in-situ* uncertainties. Many of these uncertainties are derived from a similar source, such as MC modeling or the photon and lepton energy scales, and are strongly correlated. A set of 62 independent NPs are derived by diagonalizing the total covariance matrix. The NPs with the largest eigenvalues are separated out while the residual NPs are combined with only a minimal loss of correlation information. In total the eigenvalue decomposition is able to reduce the set of 62 *in-situ* uncertainties into 6 distinct NPs with only a percent-level loss of correlation information.

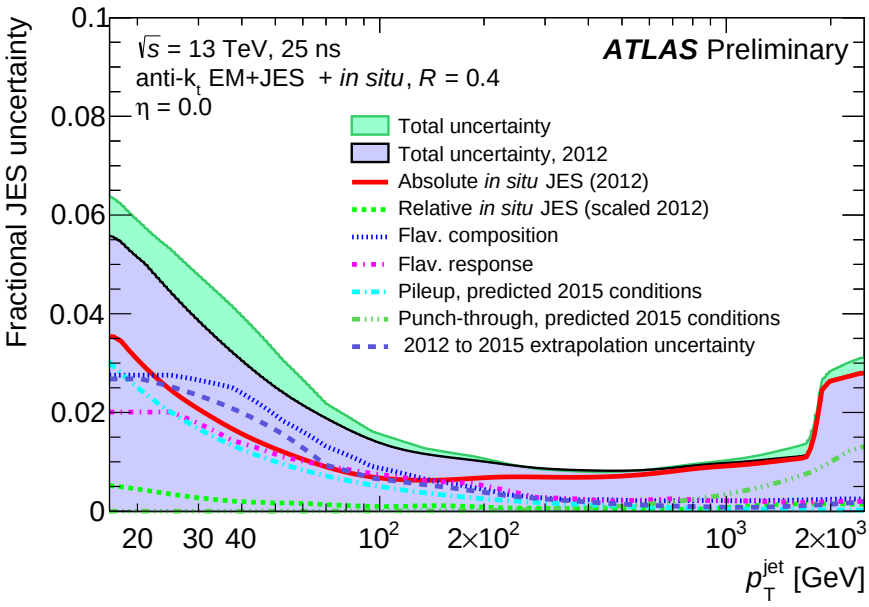

Figure 5.7: The jet energy scale uncertainty as a function of p_{T} at $\eta = 0$. Uncertainty are grouped into subcategories of absolute *in-situ* JES (boson balance, multijet balance, single particle response), relative *in-situ* JES ($\eta-$intercalibration), flavor composition, flavor response, pile-up, punch-through, and the 2012 to 2015 *in-situ* extrapolation uncertainties. The total uncertainty for 2015 is shown in the green band alongside the total uncertainty derived in 2012.

A second procedure [103] further reduces the 6 distinct NPs and remaining 12 systematic uncertainties into 3 strongly reduced NPs. Two individual NPs with the largest correlation are isolated while the remaining subdominant NPs are quadratically combined. While a significant loss of correlation information is seen in the strongly reduced set it is isolated to distinct regions of the jet-jet p_{T}-η parameter space. A map of the correlation information loss between the full systematic uncertainty treatment and the strongly reduced configuration is shown in Figure 5.8(a) as a function of jet p_{T} for $\eta^{\mathrm{jet1}} = 0$ and $\eta^{\mathrm{jet2}} = 0.5$. The loss of correlation information is maximized in the region where the leading jet has a p_{T} between 1.3 and 1.8 TeV and the subleading jet has a p_{T} below 1 TeV. In Figure 5.8(b) the same correlation loss map is superimposed with a map of events passing the dijet analysis, showing the region of maximum correlation loss is mostly avoided.

To quantify the affect of the correlation loss, three other distinct sets of strongly reduced NPs are derived using the same method, but varying the NP combination so as to alter the affected region of parameter space. Predicted limits are calculated for q^* signals using

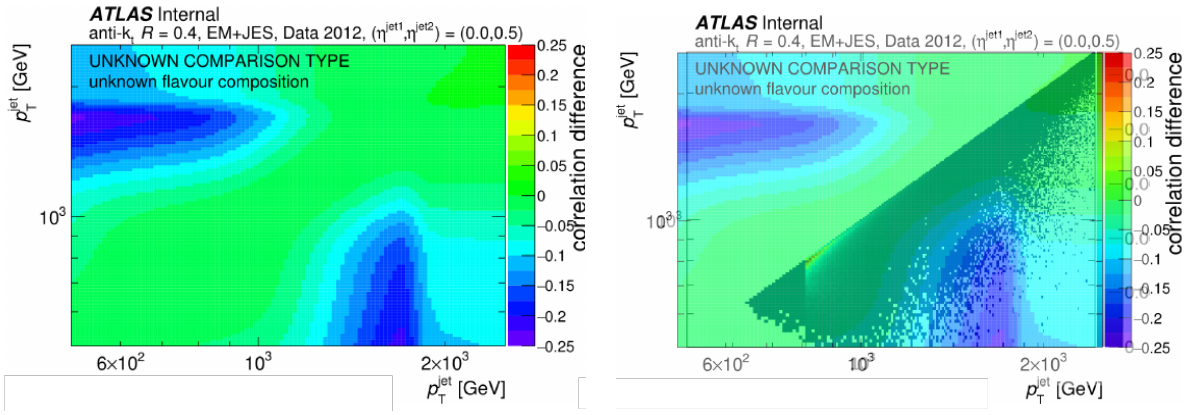

(a) (b)

Figure 5.8: (a) Difference in the correlation matrix between the full systematic uncertainty treatment and the strongly reduced configuration as a function of jet p_{T} for $\eta^{\mathrm{jet1}} = 0$ and $\eta^{\mathrm{jet2}} = 0.5$, where jet1 and jet2 are any two jets in an event. (b) A map of events passing the dijet analysis selection overlaid on the correlation difference map of (a), where jet1 and jet2 are the leading and subleading jets by p_{T}, respectively. The phase space of the analysis mostly avoids the regions of large correlation information loss.

JES Configuration	1	2	3	4
Expected Limit (TeV)	2.51	2.50	2.41	2.44

Table 5.2: Expected lower limits for q^* detection with a data sample of 1 fb^{-1} under the 4 different strongly reduced JES configurations. The difference of 4% is found to be negligible.

Pythia 8.1 backgrounds at 1 fb^{-1}, as shown in Table 5.2. The difference in predicted limits is found to be no more than 4% and is minor relative to the size of the JES uncertainties themselves. The sensitivity to correlation loss is therefore determined to be negligible and a single set of strongly reduced NPs is used for limit setting.

5.2.5 Jet Energy Resolution

The energy of a jet cannot be exactly measured due to noise, stochastic fluctuations in the calorimeter response, and detector calibration effects. A distribution of jet energy measurements of jets with the same true energy are assumed to have a Gaussian spread whose width is known as the jet energy resolution (JER). The width of the balance distributions in the η – intercalibration and boson *in-situ* calibrations are used to derive the JER as a function of p_{T} and $|\eta|$. These distributions are then fit with Eq. 3.2 to determine the constants for

the different uncertainty terms.

The noise term arises due to pile-up, electronic noise and jet reconstruction threshold effects. At low p_{T} the noise term is dominant, with very large uncertainties and a shape similar to the stochastic term. The noise term is therefore determined independently by three separate techniques and is held constant in the fit of the *in-situ* JER distributions. The noise arising from the electronics and threshold effects is predicted in MC samples with no pile-up ($\mu = 0$) through a fit of Eq. 3.2 to the JER distribution. Noise including pile-up is measured in data by balancing the energy deposited in two cones of opposite ϕ in an event selected using a zero-bias trigger[1], with the difference in energy taken as a measure of the noise. A second method serves as a systematic on the pile-up noise measurement by subtracting the average density ρ of an event from each jet according to its area. For an unbiased event sample selected from $\mathrm{Z}\rightarrow \mu\mu$ events, which is assumed to have no jets occurring from the hard scatter, the distribution is expected to be centered about 0 with the width of the distribution representing the fluctuations per unit area due to noise.

The no pile-up MC noise result is added in quadrature with the pile-up term to determine a jet resolution noise term of 3.33 ± 0.63 GeV. The *in-situ* resolution results are fit with Eq. 3.2 to determine the stochastic and constant resolution terms, with the full jet resolution uncertainty of

$$\frac{\sigma_E}{E} = \frac{3.33 \pm 0.63 \text{ GeV}}{E} \oplus \frac{0.71 \pm 0.07 \text{ GeV}^{\frac{1}{2}}}{\sqrt{E}} \oplus 0.030 \pm 0.003 \tag{5.5}$$

As with the jet energy scale calibration, the difference in JER due to 2015 data-taking conditions and MC modeling are taken as additional uncertainties on the 2012 derived JER. As the uncertainty due to the 2012 to 2015 extrapolation is dominant, all uncertainties are combined into a single NP with minimum correlation loss. The uncertainty as a function of p_{T} and η are shown in Figure 5.9.

The effect of the JER uncertainty on the signal acceptance and m_{jj} shapes of the dijet analysis is found to be minor. As the JER is negligible with respect to the larger energy scale uncertainties it is dropped from the analysis.

1. The zero-bias trigger records events one LHC rotation after a specific L1 trigger. The recording of these events are therefore unbiased by any activity within the event and are collected at a rate proportional to the instantaneous luminosity of the beam.

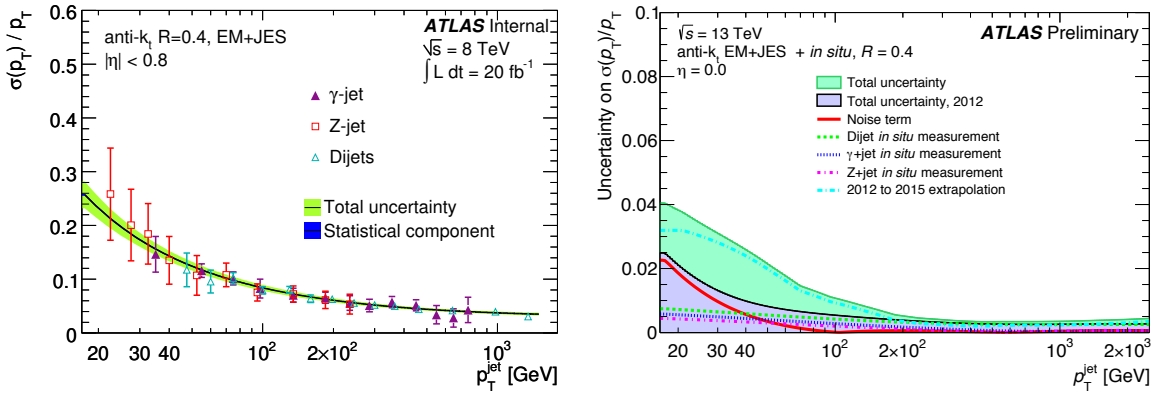

(a) (b)

Figure 5.9: Jet energy resolution (a) and its uncertainty (b) as a function of jet p_{T} at $\eta = 0$. The final resolution is determined by a fit to the γ+jet, Z+jet, and dijet resolutions, with the noise term held constant and derived from dedicated noise measurements. The 2012 subcomponents and 2015 extrapolation are shown in the uncertainty, and a single JER NP calculated from the combination is derived.

5.3 Jet Cleaning

Jet cleaning [104] removes fake jets which are not likely to have been produced by the hard scatter or pile-up collisions within the detector. Fake jets may be caused by coherent calorimeter noise that passes data quality criteria [105]. Several sources of non-collision background may also create fake jets such as cosmic rays or beam-induced backgrounds. Beam-induced backgrounds include protons lost from the beam upstream of the interaction point or from collisions of protons with residual gas in the beam pipe. Fake jets, in combination with the high pile-up conditions, can mirror the QCD background. Fake jets are identified by the following detector-level quantities.

Calorimeter Noise

The shape of signals in the EM calorimeters is used to discriminate between the energy deposits of fake and real jets. A quality factor $\mathcal{Q}_{\mathrm{cell}}$ quantitatively compares the LAr pulse to the expected pulse shape from real jets in a single cell. Energy deposits in cells with small values of $\mathcal{Q}_{\mathrm{cell}}$ are more likely to have occurred from real jets than those with large values. The relative pulse quality of all cells within a jet is measured by the energy-weighted average of pulse quality, $\langle \mathcal{Q}_{\mathrm{cell}} \rangle$, and the fraction of total energy deposited in LAr cells of poor quality, f_Q. The fractional energy from poor quality cells

is measured in all LAr calorimeters (f_Q^{LAr}) as well as only the forward HEC (f_Q^{HEC}). Noise bursts in the calorimeters may also be reconstructed as negative energy deposits, providing discrimination through the sum of energy E_{neg} in all negative energy cells associated with the jet.

Energy Ratio

Energy deposits originating from calorimeter noise or beam-induced backgrounds are often localized in small regions of the calorimeter and extend laterally in the detector rather than longitudinally. A measure of the fraction of total energy located only in the EM calorimeter (f_{EM}), only in the HEC (f_{HEC}), or only in single calorimeter layer (f_{max}) can discriminate against energy deposits which are localized or lateral.

Tracking Variables A real jet typically contains charged hadrons that deposit energy in the inner detector, reconstructed as tracks that can be associated with the jet. The relative fraction of jet p_{T} measured by tracks in the inner detector (f_{ch}) can identify fake jets formed outside of it.

The jet selections used to identify bad jets during Run 2 were based on established criteria of Run 1 as well as performance studies using the new Run 2 data. For these studies enriched samples of good jets and bad jets are created independently of the cleaning variables listed above to facilitate the optimization of cleaning cuts. Events are selected using fully efficient single jet triggers. The sample of events enriched in good jets requires:

- at least two jets with $p_{\mathrm{T}} > 70$ GeV,
- back-to-back leading jets with $\Delta\phi_{12} > 3$,
- balanced jet momentum with $|p_{\mathrm{T}}^1 - p_{\mathrm{T}}^2|/(p_{\mathrm{T}}^1 + p_{\mathrm{T}}^2) < 0.3$.

The sample enriched in fake jets requires:

- at least one jet with $p_{\mathrm{T}} > 70$ GeV,
- a substantial imbalance in the calorimeter energy, defined as $H_{\mathrm{T}}^{\mathrm{miss}} = \sum_{\mathrm{jets}} p_{\mathrm{T}}$,
- the direction of $H_{\mathrm{T}}^{\mathrm{miss}}$ pointing away from the leading jet, with $\Delta\phi_{j,H_{\mathrm{T}}^{\mathrm{miss}}} > 3$,

- the leading jet to be out-of-time with respect to the bunch crossing timing, with $|t_{jet}| >$ 6 ns.

A loose working point for jet cleaning was derived with a 99.5% (99.9%) efficiency of selecting good jets of $p_{\mathrm{T}} > 20(100)$ GeV. Jets are flagged as fake and removed if they pass any of the following loose cleaning criteria:

- $f_{\mathrm{HEC}} > 0.5$ and $|f_Q^{\mathrm{HEC}}| > 0.5$ and $\langle \mathcal{Q}_{\mathrm{cell}} \rangle > 0.8$,
- $|E_{\mathrm{neg}}| > 60$ GeV,
- $f_{\mathrm{EM}} > 0.95$ and $f_Q^{\mathrm{LAr}} > 0.8$ and $\langle \mathcal{Q}_{\mathrm{cell}} \rangle > 0.8$ for jets within $|\eta| < 2.8$,
- $f_{\mathrm{max}} > 0.99$ for jets within $|\eta| < 2$,
- $f_{\mathrm{EM}} < 0.05$ and $f_{\mathrm{ch}} < 0.05$ for jets within $|\eta| < 2$,
- $f_{\mathrm{EM}} < 0.05$ for jets of $|\eta| \geq 2$.

The loose jet cleaning was further tested on events passing the dijet analysis selections, with the discrimination between the good- and fake-jet enriched samples shown for the cleaning variables in Figures 5.10 and 5.11. Jet cleaning significantly reduces the number of events in the fake-jet enriched sample while maintaining the data-MC agreement in the good-jet enriched sample, as seen in the p_{T} and timing of analysis jets in Figure 5.12. Jet cleaning typically removes jets of poor timing and are distributed more evenly in jet p_{T} than QCD background, with the exception of a large population at low p_{T}.

5.3.1 Masked Tile Calorimeter Modules

Two of the 256 modules of the Tile Calorimeter suffered failures before data-taking and were not included in jet reconstruction. One module failed early and was removed from MC simulation, avoiding a bias in the data-MC comparisons. The second module did not fail until after the MC simulation was complete. As MC simulation is a time-intensive process it was not repeated to include the module failure. This MC mismodeling introduces a minor data-MC discrepancy which is corrected by the $\eta-$intercalibration.

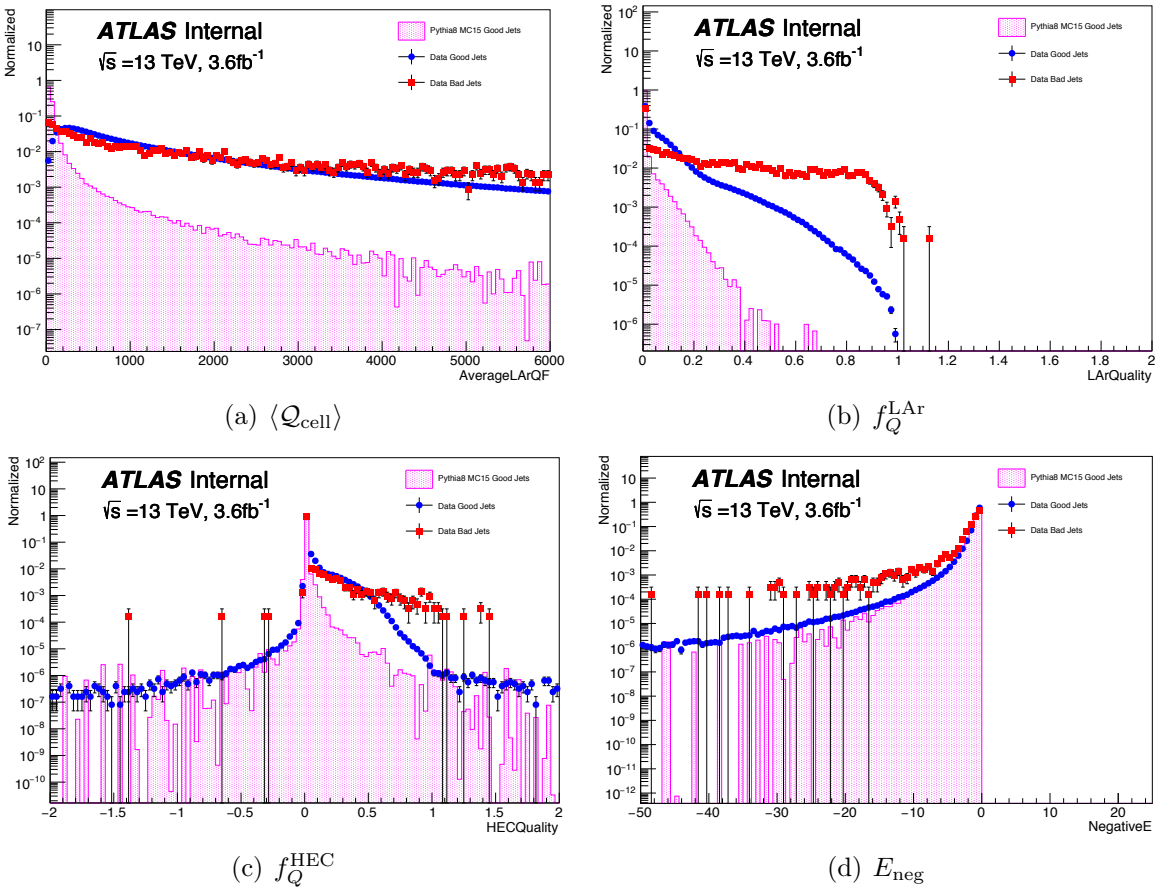

(a) $\langle \mathcal{Q}_{\text{cell}} \rangle$

(b) f_Q^{LAr}

(c) f_Q^{HEC}

(d) E_{neg}

Figure 5.10: Distributions of jet cleaning variables in good-jet enriched samples in MC (purple) and data (blue) as well as fake-jet enriched samples of data (red) for (a) $\langle \mathcal{Q}_{\text{cell}} \rangle$, (b) f_Q^{LAr}, (c) f_Q^{HEC}, and (d) E_{neg}. MC modeling of $\langle \mathcal{Q}_{\text{cell}} \rangle$, f_Q^{LAr}, and f_Q^{HEC} is known to be poor and discrepancies with data are expected. Events are chosen after applying the dijet analysis selections described in Section 6.1, with a relaxed $y^* < 1.7$. Distributions are normalized to have an integral of 1.

5.4 Jet Triggering

Events are selected using triggers (Section 3.2.6) focused on finding high-p_{T} jets. A jet p_{T} threshold is set at each level of the trigger to ensure all events can be reprocessed and stored. At L1 the calorimeter-based trigger, L1Calo, cannot examine the signals from each calorimeter cell separately due to bandwidth constraints. Instead several topologically close cells within $\Delta\eta \times \Delta\phi$ of 0.1×0.1 form a single trigger tower whose individual signals are summed into a single pulse. The magnitude and shape of a trigger tower pulse is used to

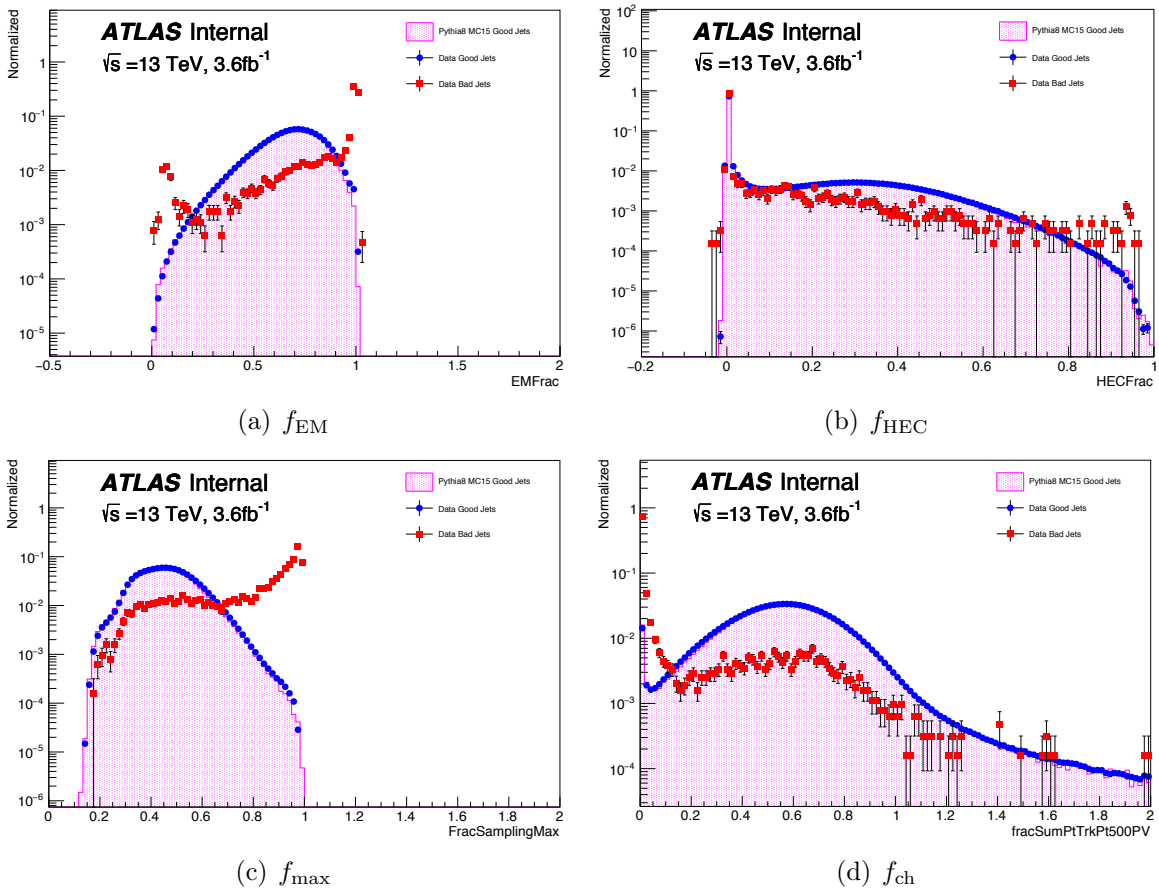

(a) f_{EM} (b) f_{HEC}

(c) f_{max} (d) f_{ch}

Figure 5.11: Distributions of jet cleaning variables in good-jet enriched samples in MC (purple) and data (blue) as well as fake-jet enriched samples of data (red) for (a) f_{EM}, (b) f_{HEC}, (c) f_{max}, and (d) f_{ch}. Events are chosen after applying the dijet analysis selections described in Section 6.1, with a relaxed $y^* < 1.7$. Distributions are normalized to have an integral of 1.

measure its energy and timing.

The uncalibrated E_{T} of a jet is found through a sliding window algorithm which coarsely calculates the E_{T} from several adjacent trigger towers. The L1 J100 trigger requires the event to have a significant energy deposit of $E_{\mathrm{T}} \geq 100$ GeV. Jets in events reaching the high level trigger (HLT) are fully reconstructed but do not benefit from the full calibration chain, resulting in slightly lower values of E_{T} than after calibration. The HLT j360 trigger requires events passing the L1 J100 trigger to have a jet with $E_{\mathrm{T}} \geq 360$ GeV. The 360 GeV limit is sufficiently high enough to allow all events to be processed and stored on disk.

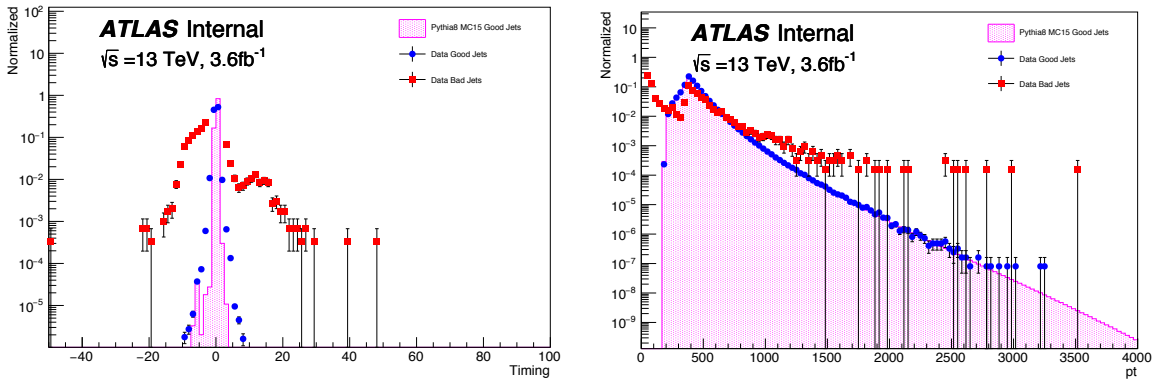

(a) (b)

Figure 5.12: Distribution of the jet timing (a) and jet p_{T} (b) in good-jet enriched samples in MC (purple) and data (blue) as well as fake-jet enriched samples of data (red). Events are chosen after applying the dijet analysis selections described in Section 6.1, with a relaxed $y^* < 1.7$. Distributions are normalized to have an integral of 1.

The E_{T} thresholds of the triggers do not correspond precisely to the final calibrated E_{T} and therefore will still reject some events containing jets with a true E_{T} above 360 GeV. The observable of interest, m_{jj}, can similarly be biased by its kinematics as events with identical m_{jj} can include jets both above and below the E_{T} threshold. Any bias from this effect can be avoided by requiring more stringent analysis selections on the leading jet p_{T} and m_{jj}. These selections are calculated for the dijet phase space through trigger efficiency curves as described in Section 6.1.2.

CHAPTER 6
ANALYSIS SELECTION

A search for new physics would already be possible with the choice of analysis observable m_{jj}, the reconstruction of input jets, and the choice of BSM models. However an uninformed search would fail to maximize the potential sensitivity of the analysis. Selection criteria applied on the kinematics of the jets are able to enhance the contributions of BSM s-channel processes while suppressing the dominant t-channel QCD processes. An absence of quality cross-checks on the data and detailed MC comparisons may fail to catch defects that would bias the m_{jj} distribution and results.

The analysis selections are presented in Section 6.1, including their optimization on signal significance and trigger efficiency. The choice of m_{jj} binning is presented in Section 6.2 that facilitates a smooth and sensible background estimation. The criteria for including new data and the data quality cross-checks are presented in Section 6.3, while a set of runs of special consideration are presented in Section 6.4.

6.1 Event Selection

Selections are made on event observables to define the phase space of the analysis which maximizes potential signal yield while minimizing QCD background contamination. Events are also removed if they show characteristics of poor quality data or have features unexpected of a back-to-back two jet system. A record of the event selections and their effect on the event yields, referred to as the analysis cutflow, is presented in Table 6.1 of Section 6.1.3.

Regardless of our analysis criteria, the ATLAS subdetectors are constantly monitored for suboptimal operation, noise bursts, or data corruption. For each run a list of lumiblocks (Section 3.2.6) is selected during which all subdetectors were fully operational, referred to as the Good Run List (GRL). Any data taken outside of the lumiblocks listed in the GRL is discarded by the analysis, and amounts to $\sim$18% of the data collected in 2015. Within an accepted lumiblock individual events may be removed due to noise bursts in the calorimeters or data corruption. The data is coarsely scanned for tell-tale signs of such activity and events are flagged by subdetector experts. Events taken during the recovery process of the SCT from radiation-induced upsets are also vetoed.

Further selections are applied to ensure the events are characteristic of a dijet event. Events are required to have a reconstructed primary vertex with at least two associated tracks, removing events where the hard scatter vertex may only be associated with one of the jets. Events are required to pass a high-p_{T} jet trigger, described in Section 5.4, to avoid recording a large number of less interesting events. The unprescaled HLT j360 trigger utilizes the full luminosity collected in 2015. Events are rejected if any of the three leading jets fail the jet cleaning criteria of Section 5.3. The event selection also includes several cuts to optimize the search and to ensure the trigger efficiency for collecting events is above 99.5% in the analysis phase-space, detailed in Section 6.1.1.

6.1.1 Selection Optimization

The analysis is optimized to increase the sensitivity to BSM signals and reject as much of the QCD background as possible. As detailed in Section 2.2, the production of heavy physics particles is an s-channel process with decays generally occurring isotropically throughout the detector, though a small dependence on spin may exist [106]. Alternatively the QCD background is primarily produced through t-channel processes that favor jets in the forward region. The difference in rapidity between the two leading jets, described by Eq. 6.1, can be used to reject events with more forward jets and increase the relative signal yield.

$$y^* = \frac{|y_1 - y_2|}{2} \tag{6.1}$$

The analysis sensitivity to y^* was studied by summing the significance ($S/\sqrt{B}$) over m_{jj} bins for various values of y^*, as shown in Figure 6.1(a). An optimal value of $y^* = 0.6$ was found. Other analysis selections were also explored, such as the boost of the two jet system relative to the detector ($y_{\mathrm{boost}} = (y_1 + y_2)/2$) shown in Figure 6.1(b), the sum of the p_{T} of the two leading jets, and the mass-drop variable ($\max(m_1, m_2)/m_{jj}$). No gain in the sensitivity was found with these other selections and they were not included in the analysis.

6.1.2 Trigger Efficiency

The HLT j360 trigger is used to collect all events which include a jet with p_{T} above 360 GeV at the HLT level. The HLT p_{T} is not an accurate measure of the jet p_{T} after all corrections

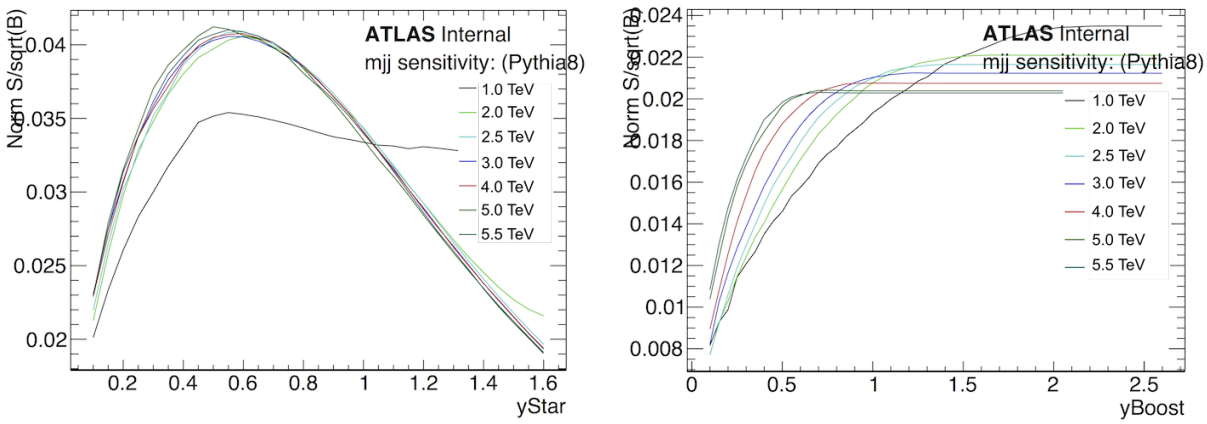

(a) (b)

Figure 6.1: Dijet resonance analysis sensitivity to various cut values for (a) y^* and (b) y_{boost}. A selection value of $y^* = 0.6$ is chosen, and no selection on y_{boost} is made.

and calibrations are taken into account and may therefore reject events with a calibrated p_{T} above 360 GeV depending on their kinematics. A true p_{T} cutoff is established for calibration stage jets by comparing events passing both the HLT j360 and a lower p_{T} trigger, HLT j260.

The data quality selections and the $y^* < 0.6$ cut are applied to ensure the trigger efficiency curves are calculated in the dijet phase space. Curves are created from the ratio of events passing both HLT j360 and HLT j260 to those passing only HLT j260, and are derived as a function of leading jet p_{T}, shown in Figure 6.2(a), and m_{jj}, shown in Figure 6.2(b). A fit to the curve determines the plateau at which the trigger becomes 99.5% efficient, and a conservative event selection is taken to be $p_{\text{T}} > 440$ GeV and $m_{jj} > 1.1$ TeV.

6.1.3 Event Cutflow

The event cutflow tracks the number of events at each stage of the selection to quantify their impact. The cutflow for data is listed in Table 6.1 and for MC simulation in Table 6.2. Data quality variables are not required for the MC simulation.

While only one trigger selection is required, two trigger selections are presented in the data cutflow. This is an artifact of the unique aspects of this early analysis in which the continual availability of new data and the extensive cross-checks for the very first 13 TeV data required a two stage processing of data. The first stage did not include the Jet Cleaning, leading jet p_{T}, m_{jj}, and y^* selections. Furthermore several triggers beyond HLT j360, as

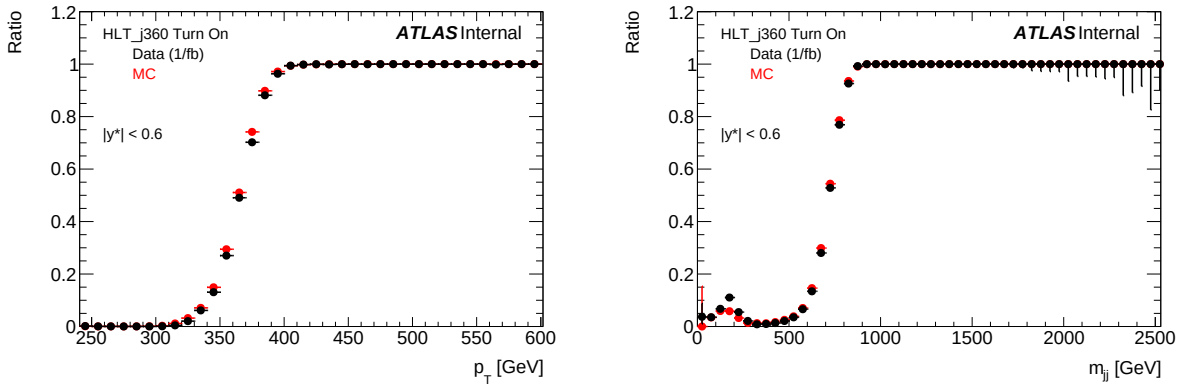

(a) (b)

Figure 6.2: Trigger efficiency curves for the HLT j360 trigger as a function of p_{T} (a) and m_{jj} (b) in the resonance selection. The ratio is derived as the number of events passing both HLT j360 and HLT j260 to those passing only HLT j260.

described in Section 5.4, were saved for use in cross-checks and other analyses of similar phase-space. The L1 triggers J75 and J100 were included, saving events at L1 that may not have passed the HLT trigger. Also included were the multijet triggers HLT 3j175 and HLT 4j85 that select events with at least 3 jets above 175 GeV at HLT scale or 4 jets above 85 GeV at HLT scale, respectively. The Full Trigger List entry in the analysis cutflow includes all these triggers from the first stage, while the HLT j360 trigger is applied during the second stage.

Event Selection	N_{events}	Rel. Decrease (%)
All GRL Events	13109864	-
LAr Quality	13048555	-0.47
TileCal Quality	13045369	-0.02
SCT Quality	13032586	-0.10
Primary Vertex	13031433	-0.01
Full Trigger List	8060987	-38.14
Jet Selection	7945501	-1.43
HLT j360	3990986	-50.23
Jet Cleaning	3988328	-0.07
Leading Jet $p_{\mathrm{T}} > 440$ GeV	1457155	-63.46
$m_{jj} > 1.1$ TeV	725160	-50.23
$y^* < 0.6$	198450	-72.63

Table 6.1: Event selection table for 2015 data showing the relative decrease in the number of events between each selection. The Full Trigger List entry includes events passing any of the following triggers: L1 J75, L1 J100, HLT j360, HLT 3j175 or HLT 4j85.

Event Selection	N_{events}	Rel. Decrease (%)
HLT j360	5325238.76	-
Leading Jet $p_{\mathrm{T}} > 440$ GeV	2739505.39	-48.56
$m_{jj} > 1.1$ TeV	1177444.36	-57.02
$y^* < 0.6$	243284.94	-79.34

Table 6.2: Event selection table for PYTHIA 8.1 MC simulation showing the relative decrease in the number of events between each selection. Events are fractional due to weights applied to the MC simulation.

6.2 Invariant Mass Binning

The binning of the dijet invariant mass spectrum is an important consideration in the dijet resonance search. It is carefully chosen so as to minimize any bias introduced by the data-driven background estimation (Section 7.1) that may cause spurious signals. It should also not hide any true signals or reduce their significance, potentially missing a discovery. A relatively narrow signal in m_{jj} should be sampled over several bins while maintaining a statistically significant result. However a binning that is too wide could reduce a signal resonance to a single bin, reducing the statistical power of the search. Wide binning will also reduce the number of degrees of freedom used in the background fit and lead to overfitting.

In determining the bin sizes, a set of four criteria were introduced:

1. bins widths should be at least the size of the detector resolution,
2. the number of bins should be maximized,
3. bins should be narrow enough so that expected signals span more than 1 bin,
4. binning should produce a smooth mass spectrum.

Binning was derived using PYTHIA 8.1 QCD simulation. The full analysis selection was first applied, but the leading jet p_{T} cut was reduced to 350 GeV to reduce any kinematic bias on the binning. The procedure begins by deriving a continuous detector resolution curve from MC simulation followed by an iterative procedure to determine bin edges.

The detector resolution curve was first determined by calculating the ratio of the reconstructed m_{jj} to the true m_{jj} for each event. The ratio is binned in thin slices of true m_{jj} and the jets in the reconstructed pair are matched to the true jets to ensure no miscalculation

due to a third jet. The distribution of ratios is then fit with a Gaussian and the detector resolution is calculated as the width of the Gaussian divided by it's mean. The distribution of the detector resolutions as a function of thin m_{jj} slice is then fit with a 6 degree polynomial to derive the final detector resolution curve, as shown in Figure 6.3.

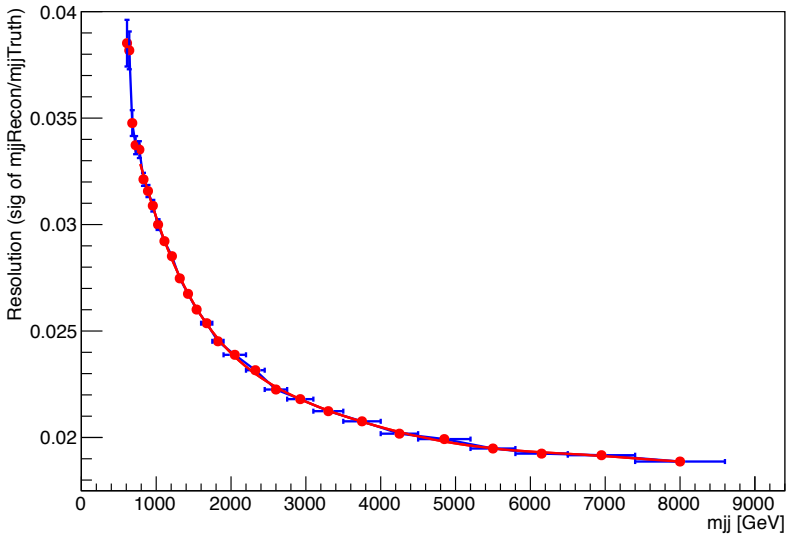

Figure 6.3: The m_{jj} resolution of the ATLAS detector as a function of true m_{jj}. Individual points are generated through the ratio of reconstructed m_{jj} to true m_{jj} using PYTHIA 8.1 QCD MC simulation. A 6^{th} order polynomial fit provides the detector resolution curve within 0.75 to 8 TeV.

An iterative procedure was used to determine the bin edges using the detector resolution and following the 4 criteria outlined above. The procedure begins at the lowest m_{jj} bound and calculates upper bounds for each bin. The lowest m_{jj} bound is required to be significantly far away from the m_{jj} peak in MC simulation to ensure no bias from the relaxed leading jet p_{T} cut. A value of 946 GeV was chosen, 100 GeV from the m_{jj} peak and significantly lower than the m_{jj} start of 1.1 TeV determined by the trigger efficiency cutoff.

The iterative procedure proceeds as follows:

1. The location of the bin center is guessed using the detector resolution R at the initial lower bound: $m_{\text{center}} = m_{\text{initial}}(1 + \frac{1}{2}R(m_{\text{initial}}))$.

2. At m_{center} a bin width is determined from the local detector resolution, providing a guess as to the lower bound: $m_{\text{lower}} = m_{\text{center}}(1 - \frac{1}{2}R(m_{\text{center}}))$

3. The derived lower bin boundary m_{lower} is checked against the true lower bin boundary m_{initial}, and is required to agree within 0.1%. If they do not agree, and $m_{\text{lower}} > m_{\text{initial}}$, m_{center} is shifted by -0.01 GeV, and step 2 is repeated. If $m_{\text{lower}} < m_{\text{initial}}$, m_{center} is shifted by +0.01 GeV, and step 2 is repeated.

4. Once m_{lower} and m_{initial} agree to within 0.1%, the new upper bin edge is calculated as $m_{\text{upper}} = m_{\text{center}}(1 + \frac{1}{2}R(m_{\text{center}}))$ and rounded to the nearest 1 GeV.

5. The procedure is repeated for the next bin, with the previous m_{upper} serving as the next m_{initial}.

The binning procedure continues until the MC statistics become insufficient at 8055 GeV. However this upper limit is too low to fully explore the QBH models, for which higher masses are theoretically possible. In Figure 6.3 it is seen that the detector resolution becomes nearly constant at high m_{jj}, so the width of the final bin is used to extrapolate out to 13,156 GeV.

The resolution of the binning, defined as bin width over bin center, is shown in black in Figure 6.2 alongside the derived detector resolution in red and the signal resolution of the benchmark q^* model in green. The signal resolution is derived from a Gaussian fit to the signal peak and is taken to be $(2 \times \sigma)/\mu$. Here it is clear the binning resolution is several multiples smaller than the signal resolution, satisfying binning criteria 3. The iterative procedure has derived binning that is near the detector resolution while maximizing the number of bins, satisfying both binning criteria 1 and 2 by construction. The agreement between the binning and detector resolution is evident in Figure 6.2, and it is found that the bin size, bin resolution curve, and final QCD spectrum are all smooth, satisfying criteria 4.

6.3 Data Quality

Data quality cross-checks are performed on new data before inclusion in the analysis. These high-level checks are independent of those performed by each ATLAS subdetector and during Jet Cleaning, and utilize the full event information, reconstructed jet properties, and analysis observables. Data-MC comparisons, detailed in Section 6.3.1, must show agreement for all observables relevant to the analysis, after accounting for systematic uncertainties. Dedicated validation techniques are also employed for the highest-p_{T} jets, such as the Jet Balance

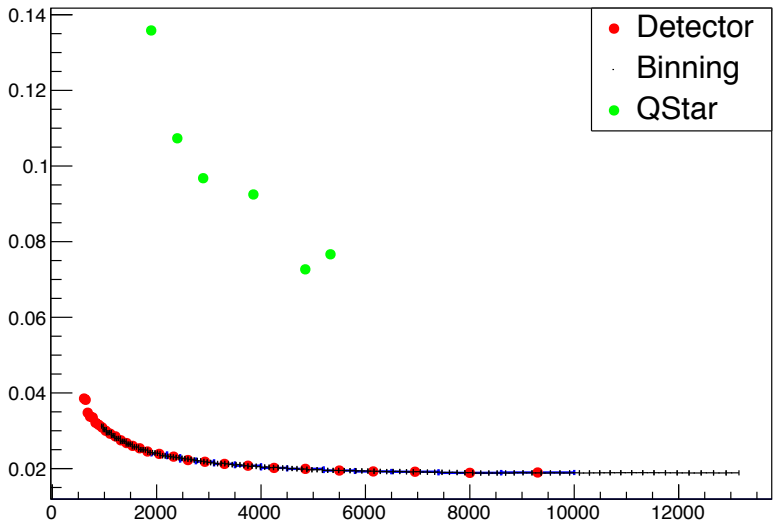

Figure 6.4: A comparison of the binning resolution (black) and local detector resolution (red) is shown to give good agreement, with the binning resolution well below the resolution of narrow signals (green). Agreement between the binning resolution and local detector resolution is generally within 1%.

method detailed in Section 6.3.2. Extra care is given to data with differences in the detector conditions or reconstruction, presented in Section 6.4.

6.3.1 Data-MC Comparisons

Each data run collected by ATLAS corresponds to a single fill of protons and the subsequent collisions. During 2015 data-taking a run could last for up to 13 hours, with the largest run collecting 546 pb^{-1} of data. Before a new run is included in the analysis it undergoes comprehensive cross-checks for any potential disagreements with MC simulation and with previously collected data. Cross-checks cover detector-level quantities, such as the distribution of energy within the calorimeter, jet reconstruction and calibration inputs [107], such as the number of muon segments involved in the GSC punch-through calibration, and analysis-level quantities. Care is taken to probe various η regions of the detector and to check the correlations between leading, subleading, and third jets, ordered by p_{T}. A few example comparisons are shown in Figures 6.5 and 6.6 for the full dataset, including the number of jets above 50 GeV and the p_{T}, η, and ϕ of the leading 3 jets of each event. Correlations between the leading and subleading jet are also shown, such as y^*, the p_{T}-asymmetry, the

angular separation, and the average subleading jet p_{T} as a function of leading jet p_{T}.

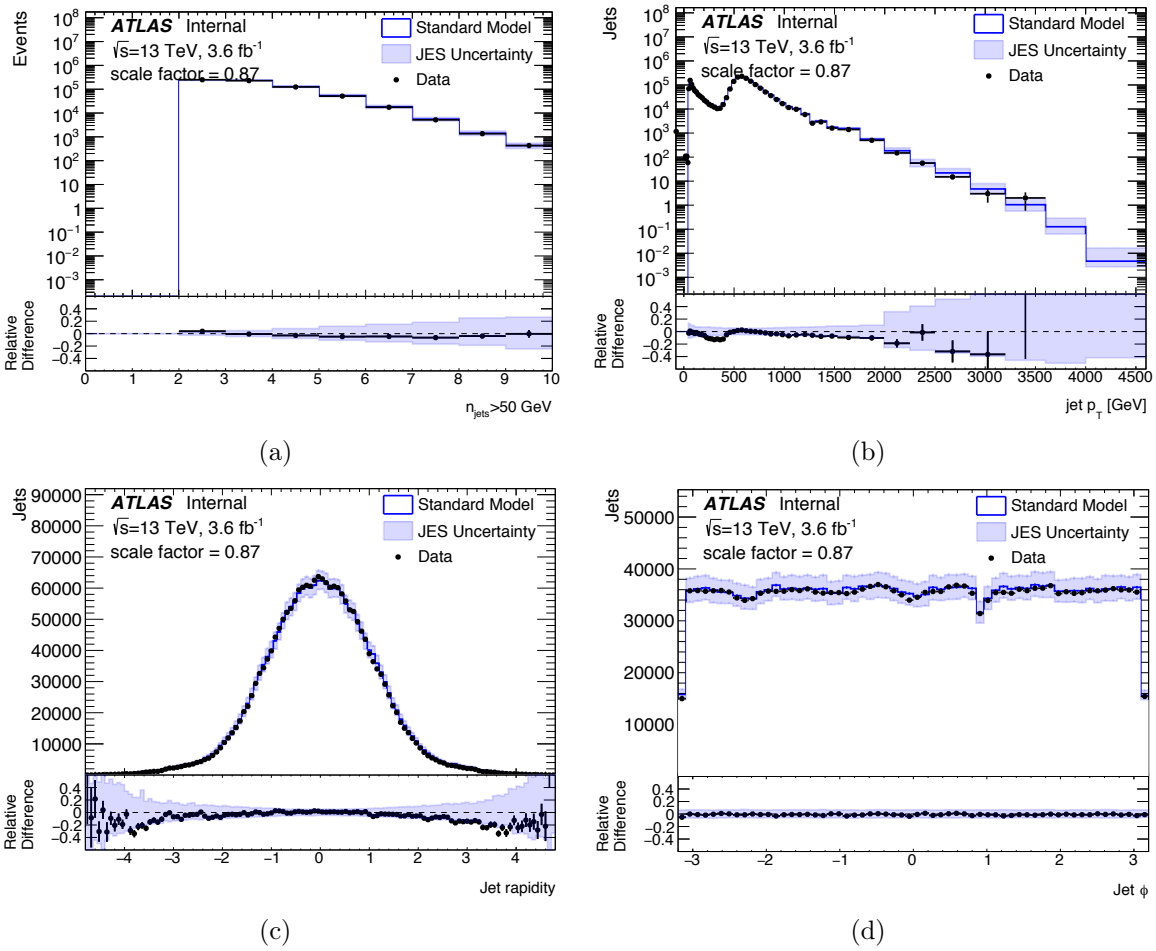

Figure 6.5: Data-MC comparisons are shown using the full 2015 dataset and PYTHIA 8.1 MC simulation. Comparisons include the number of jets above the 50 GeV pile-up cutoff (a) and the jet p_{T} (b), η (c), and ϕ (d) of the leading three jets in each event.

6.3.2 Jet Balance

A validation tool was created to check the performance of high-p_{T} jets. It is derived from the Multijet Balance Calibration (MJB) [96] which is used to calibrate high-p_{T} jets using a collection of well-calibrated, lower p_{T} jets. The procedure isolates the leading jet in p_{T}, and groups all other jets of $p_{\mathrm{T}} > 25$ GeV into a single four-vector, the recoil system. The p_{T} balance is calculated between the leading jet and the recoil system, with any significant imbalance a sign of potential mis-calibration. Two iterations of the validation are performed: one with identical event selections at the MJB (multijet validation), and one with tweaked

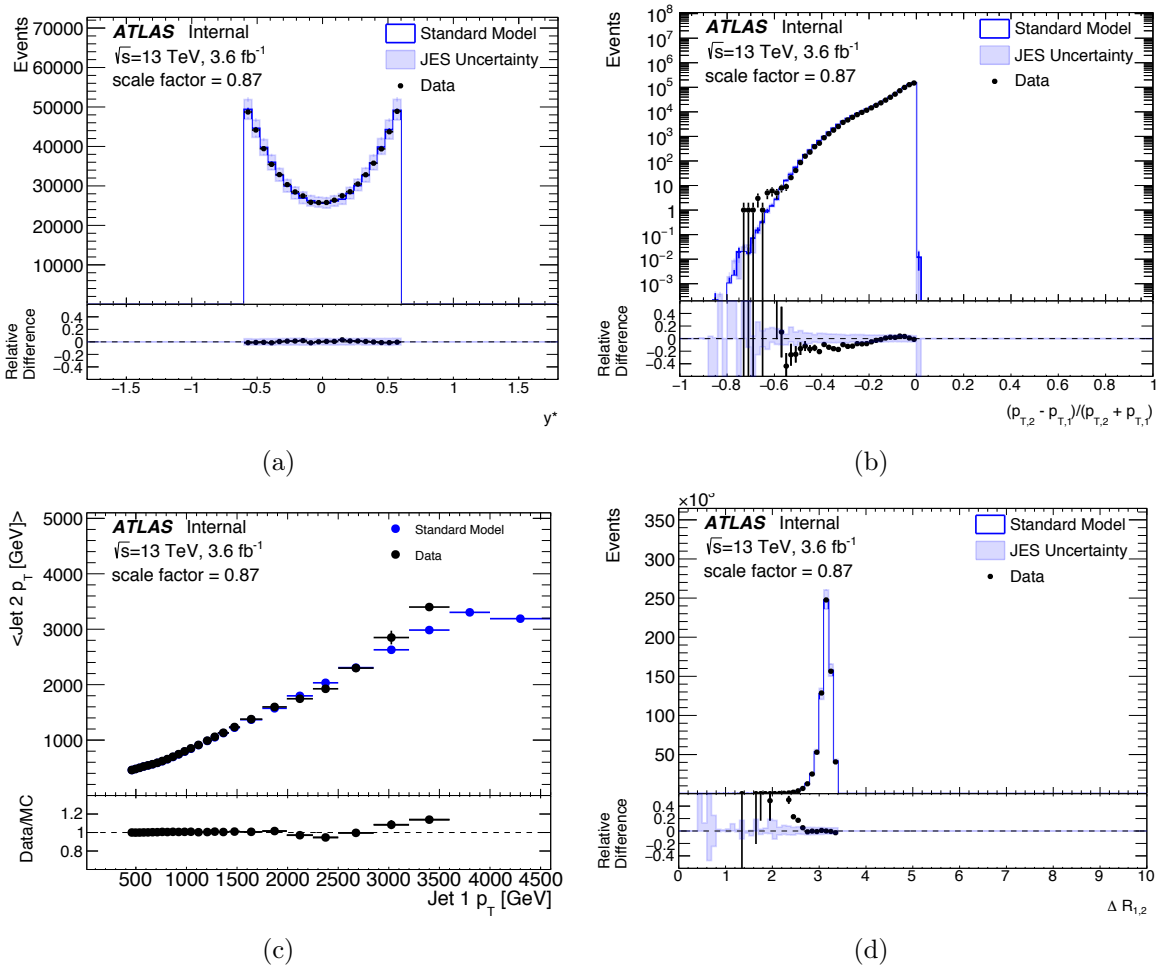

(a) (b) (c) (d)

Figure 6.6: Data-MC comparisons are shown using the full 2015 dataset and PYTHIA 8.1 MC simulation. Comparisons include y^* (a), the p_{T}-asymmetry ($(p_{\mathrm{T}}^1 - p_{\mathrm{T}}^2)/(p_{\mathrm{T}}^1 + p_{\mathrm{T}}^2)$) (b), the angular separation (dR_{12}) (c), and the average subleading jet p_{T} as a function of leading jet p_{T} (d).

selections to allow for dijet events of interest (dijet validation). The selections are as follows, with values for the dijet validation shown in parenthesis:

- leading jet $|\eta_{\mathrm{det}}| < 1.2$,
- at least three (two) jets with $|\eta_{\mathrm{det}}| < 2.8$ and $p_{\mathrm{T}} > 25$ GeV,
- JVT > 0.64 for any jet with $p_{\mathrm{T}} < 50$ GeV and $|\eta| < 2.4$, where JVT is a track-based multivariate discriminate against pile-up jets [108],
- no selected jets failing the Jet Cleaning criteria,

- the second leading jet composes $\leq 80\%$ (100%) of the recoil system p_{T},
- $\alpha > \pi - 0.3$, where $\alpha = |\Delta\phi(\mathrm{jet}_1, \mathrm{recoil})|$,
- $\beta_i > 1$ for jets of $p_{\mathrm{T}} > \frac{1}{4} p_{\mathrm{T}}^{\text{leading jet}}$, where $\beta_i = |\Delta\phi(\mathrm{jet}_1, \mathrm{jet}_i)|$

The first four selections ensure the jets are of good quality. The last two ensure that the leading jet and recoil system are properly balanced in ϕ and that the subleading jets do not contaminate the leading jet. For the multijet validation the second and fifth selections ensure that there are multiple jets and that more than one of them significantly contributes to the recoil system. These two selections are relaxed for the dijet validation to allow for two-jet events.

The results of the multijet validation are shown in Figure 6.7(a) for the full 2015 dataset beginning at a recoil system p_{T} of 500 GeV, where the HLT j360 trigger is fully efficient in the recoil system p_{T} variable. Good agreement is found between data and three independent MC generators. The small discrepancies are well below 1% and are completely covered by jet energy scale uncertainties. Similar agreement between data and Pythia 8.1 MC is found in the dijet validation shown in Figure 6.7(b), which uses the first 1 fb^{-1} of data collected. The plot is shown for values of recoil system p_{T} below the HLT j360 trigger efficiency cutoff of 500 GeV. This has the effect of including events where the lead jet fluctuates upwards in pt compared to the recoil system and rejecting events where the lead jet fluctuates downwards in pt compared to the recoil system, ultimately leading to an upward tail in the response. Both the multijet validation and the dijet validation show the p_{T} of jets to be well calibrated across the entire p_{T} spectrum.

6.4 Special Data

The following data runs or events are affected by non-standard detector operation or event reconstruction and were carefully checked before inclusion in the analysis.

6.4.1 IBL-off

Between the 5th and 6th of October the inner pixel layer IBL was powered off to investigate a drift in the current consumption. Data-taking continued, collecting 230 pb^{-1} of IBL-off

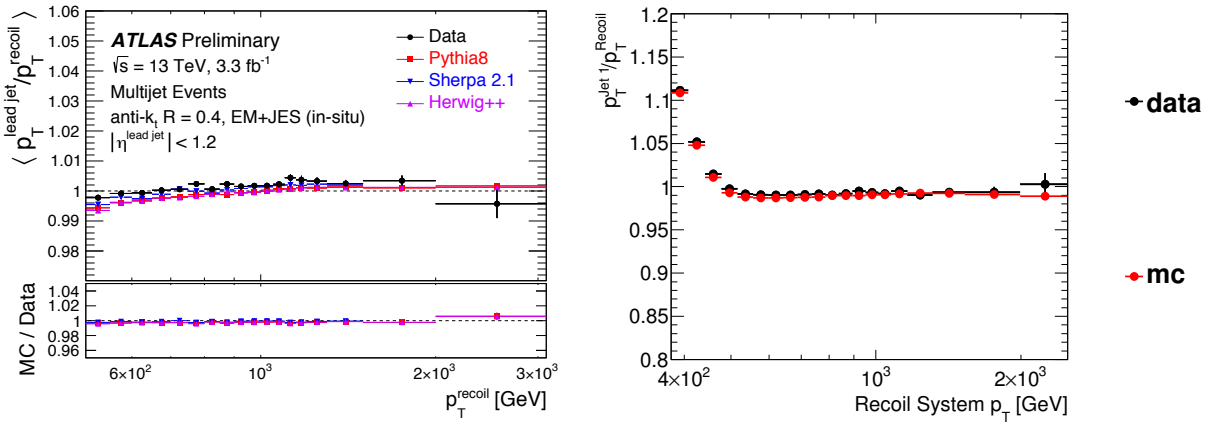

(a) (b)

Figure 6.7: Validation of jet calibration using multijet events (a) and dijet events (b). After the selections detailed in the text, the ratio of leading jet p_{T} to recoil system p_{T} in data agrees with MC simulation. PYTHIA 8.1, SHERPA 2.1, and HERWIG++ are used in the multijet validation, while only PYTHIA 8.1 is used in the dijet validation. The upward curve at low p_{T} in (b) is an expected feature below the trigger efficiency cutoff of 500 GeV in recoil system p_{T}.

data. The IBL is one layer of many in the ID, and its removal is expected to negligibly affect the efficiency of track reconstruction and the accuracy of track p_{T} measurements. The GSC calibration depends on the number of tracks and the p_{T}-weighted angular spread of tracks associated with a jet, but removing the IBL is also expected to have a negligible effect.

The IBL-off data was carefully cross-checked against IBL-on data and MC simulation for any evidence of bias. While most track and jet observables showed good agreement, a small possible deficiency in the number of high-p_{T} jets was observed, as shown for the leading jets in Figure 6.8(a). This discrepancy was checked before the GSC calibration was applied, shown in Figure 6.8(b), showing a noticeable deficit regardless of GSC.

As the GSC calibration does not cause the high-p_{T} deficit, the compatibility within statistical fluctuations of the IBL-off dataset was checked against the IBL-on dataset and MC simulation. The Kolmogorov-Smirnov (KS) test [109] was employed to measure the probability that the IBL-off dataset was drawn from the same distribution as the IBL-on dataset. The KS test samples two distinct distributions as they evolve with respect to a common parameter, m_{jj}, and compares their empirical distribution functions for compatibility. For compatible histograms the KS test will return probability values evenly distributed between 0 and 1, while incompatible histograms will return probability values close to 0. Choosing

an acceptance criteria of $\sigma_{\mathrm{KS}} \geq 0.05$, we can set a confidence level of 95% that the two histograms are drawn from the same distribution. While the KS test is nominally used on unbinned distributions it remains accurate for the m_{jj} distribution with binning smaller or on the order of any significantly physical effect.

The KS test returned a probability value of 0.55 between the IBL-off and IBL-on datasets, establishing a strong likelihood that they are compatible. A probability value of 0.72 was returned between the IBL-off dataset and MC simulation, again showing good agreement between distributions. It is therefore determined that there is a strong likelihood that the high-p_{T} deficit of the IBL-off dataset is due to statistical fluctuations.

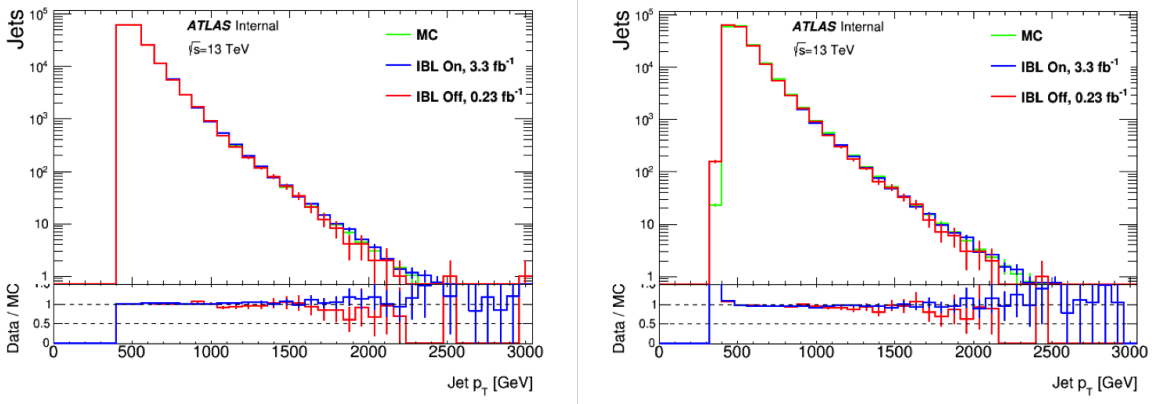

(a) (b)

Figure 6.8: Jet p_{T} spectrum before (a) and after (b) the GSC calibration is applied. Both exhibit a similar high-p_{T} deficiency. A small disagreement at the first bin of (b) is an expected feature of the trigger efficiency selection cut applied to partially calibrated jets.

The effect of the high-p_{T} deficiency on the background estimation was further explored to quantify the potential bias presented by the data's inclusion. A fit was performed on both the IBL-on only dataset and the full IBL-on + IBL-off dataset, and the two were compared. The ratio of the fits is shown in red in Figure 6.9, showing a ratio consistent with 1. A band describing the size of the fit uncertainty is shown for reference, with its magnitude significantly larger than the fit difference. The change to the total background estimate from including IBL off was found to be negligible. Details of the fitting procedure used for background estimation is outlined in Section 7.1.

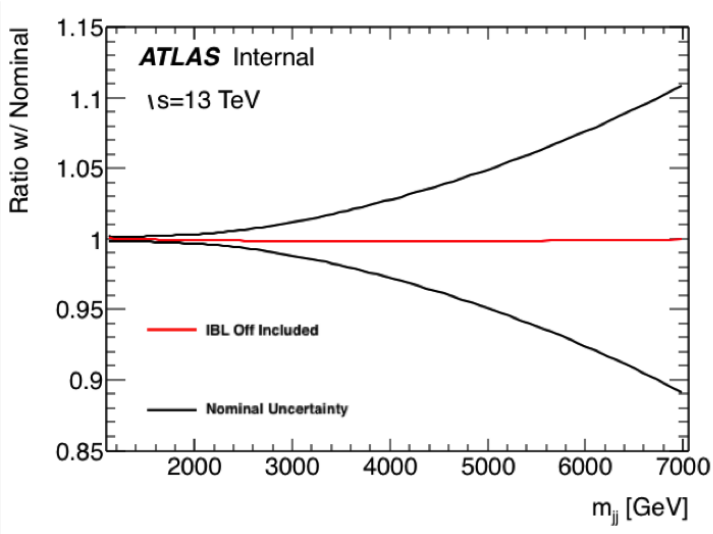

Figure 6.9: The impact on the background estimation fit of including data taken with the IBL off. The ratio between the fit with and without IBL off data (red) generally agrees with 1 and differences are significantly smaller than the fit quality uncertainty (black).

6.4.2 50 ns Data Run

Between the 21st and 22nd of August the LHC was operated with 50 ns bunch spacing instead of the nominal 25 ns spacing, resulting in 25 pb^{-1} of 50 ns data. The dijet analysis is fairly insensitive to the change in bunch spacing as it primarily affects the number of jets below 50 GeV from in-time and out-of-time pile-up. The jet energy scale uncertainties are calculated separately for 50 ns data, and the differences with the nominal uncertainties are well below 1% above 50 GeV [92]. Comparisons of 75 pb^{-1} of early 25 ns data against MC derived for 50 ns bunch spacing and 25 ns bunch spacing is shown in Figure 6.10 with good overall agreement. As no disagreements were found in data-data and data-MC comparisons with the 50 ns data, it is included in the analysis.

6.4.3 Debug Stream

Most physics events are processed rapidly by the HLT and included in a dataset known as the main stream. Any event which fails processing or takes an inordinate amount of time are cancelled and the full event information is saved to the debug stream. During 2015 data-taking an inefficiency in the muon trigger reconstruction caused a large number of events with many muon segments to be placed in the debug stream. The events were fully reconstructed

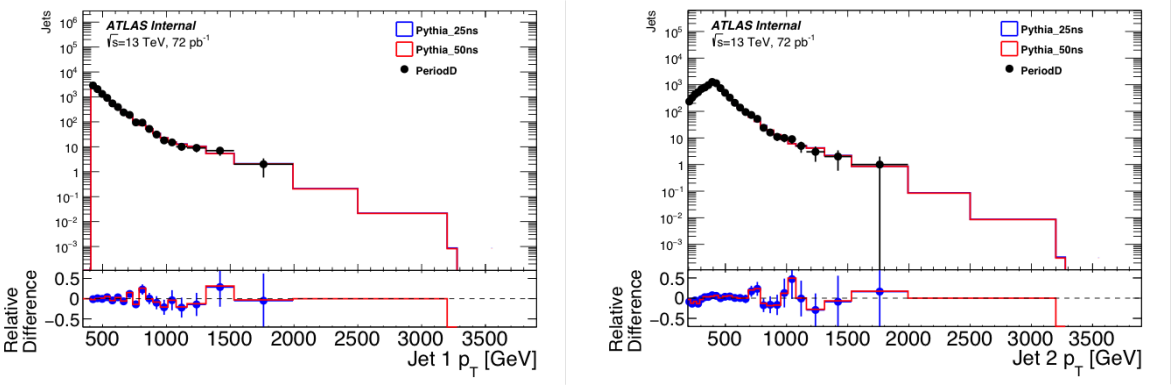

(a) (b)

Figure 6.10: Comparison of the 72 pb^{-1} of 50 ns data (black) with PYTHIA 8.1 MC simulation expectations, generated with 25 ns (blue) and 50 ns (red) bunch spacing, for the leading jet (a) and subleading jet (b). The lower panel shows the relative difference in the yield between the two MC simulations and data, showing similar agreement independent of bunch spacing.

at a later stage and included in the analysis. A comparison of the debug stream events to the entire dataset is shown in Figure 6.11. A trend is found where the debug stream has relatively more events with a large m_{jj}, likely a consequence of jet punch-through in which particles within high-p_{T} jets escape the hadronic calorimeter and produce extra muon segments. The properties of these events showed no signs of disagreement with events from the main stream or MC simulation.

6.4.4 Saturated towers

In 2015 two issues arose in the L1Calo jet triggering algorithm that led to a loss of data and the mis-reconstruction of jets. Two distinct algorithms [110] are used to calculate the bunch crossing associated with energy depositions in the trigger towers, one for saturated signals and one for non-saturated signals. Saturation occurs within a trigger tower if more than ∼250 GeV of energy is deposited.

During early data-taking at 50 ns a misconfiguration of the saturated algorithm caused it to choose a bunch crossing one position earlier than appropriate. With a bunch spacing of 50 ns it is expected that every other bunch is empty and does not contain a collision by design. Therefore when the algorithm chose an empty bunch the trigger decision was rejected and the data was lost. The saturated algorithm was quickly corrected, resulting in

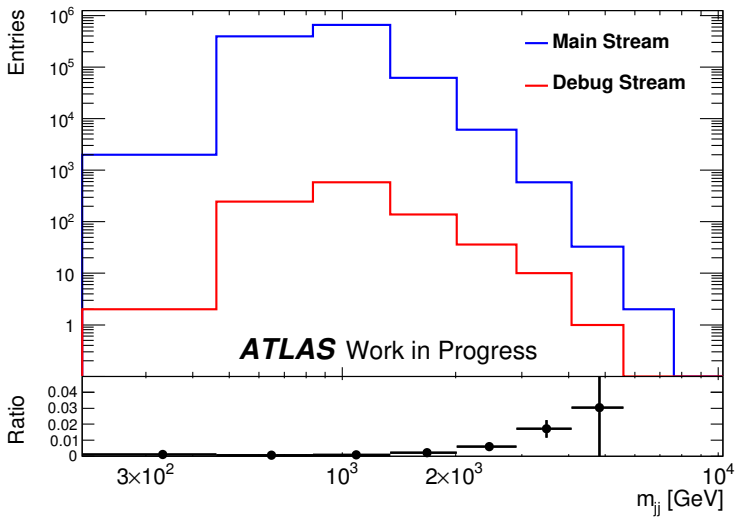

Figure 6.11: The ratio of debug stream events to the full dataset as a function of m_{jj}. The increase in relative debug stream events with larger m_{jj} is suggestive of punch-through in the muon spectrometer caused by high-p_{T} jets.

only about 100 pb^{-1} of lost data, and improvements were subsequently made to the online monitoring system.

During regular 25 ns data-taking a second, independent mistiming issue was observed. For signals of significant saturation the decision of the regular algorithm was accidentally chosen over that of the saturated algorithm. This was found to occur for energies above 500 to 1000 GeV in the Tile Calorimeter or above 2 to 3 TeV in the LAr calorimeters, depending upon the position and details of the energy deposition. This again had the effect of choosing a bunch crossing one position earlier than expected, however the data was recorded due to the 25 ns bunch spacing.

Though the previous bunch crossing was recorded some information was lost. Tracking information from the Inner Detector and Muon Spectrometer is confined to a single bunch, so the wrong tracks were recorded and the correct information was lost. Due to the details of the calorimeter energy reconstruction in which short pulses are shaped into wide signals over many BCIDs, the necessary calorimeter information was preserved. However the jet energy was reconstructed with the wrong timing, leading to mis-reconstructed jets of significantly lower p_{T}.

These events were identified from the timing of jets, as shown in Figure 6.12(a) for

mistimed jets in green and timing-corrected jets in red. The incorrect timing of most of these events were caused by saturation of the trigger signal from the Tile Calorimeter, as shown in the turn-on behavior of Figure 6.12(b) between 500 and 1000 GeV. Overall 48 events were identified that would pass into the analysis selection of the roughly 240,000 total analysis events. The timing of these events were manually corrected and the jets were reconstructed at their proper energies. The effect on m_{jj} of the mistiming can be seen in Figure 6.12(c); the spectrum of all non-mistimed events is shown in blue, the original mistimed events are show in green, and the same events reconstructed with the proper timing are show in red.

While the jet energy is properly corrected at the EM scale, a small bias in the jet calibration will occur due to the lack of tracks and muon segments associated with the event. The mis-calibration is expected to be small and should have a negligible effect on the discovery of a BSM resonance, shifting the m_{jj} of a narrow signal for a small fraction of events. However the movement of several events to lower m_{jj} could effect the background estimate, with a potentially significant effect on a discovery or limit setting. Realistic (conservative) estimates of the effect on jet p_{T} were derived from both a 3% (6%) shift in the track-based calibration of the GSC and a potential 20 (50) lost muon segments. These estimates were propagated through the jet calibration and dijet analysis and their effect on the background estimate is measured. The ratio of the new background estimate to the nominal estimate is shown in Figure 6.12(d) for each effect and is found to be well below the statistical uncertainty of the fit, even for the conservative estimates. As the background estimate is only slightly affected the analysis was performed with the 48 events reconstructed with the proper timing.

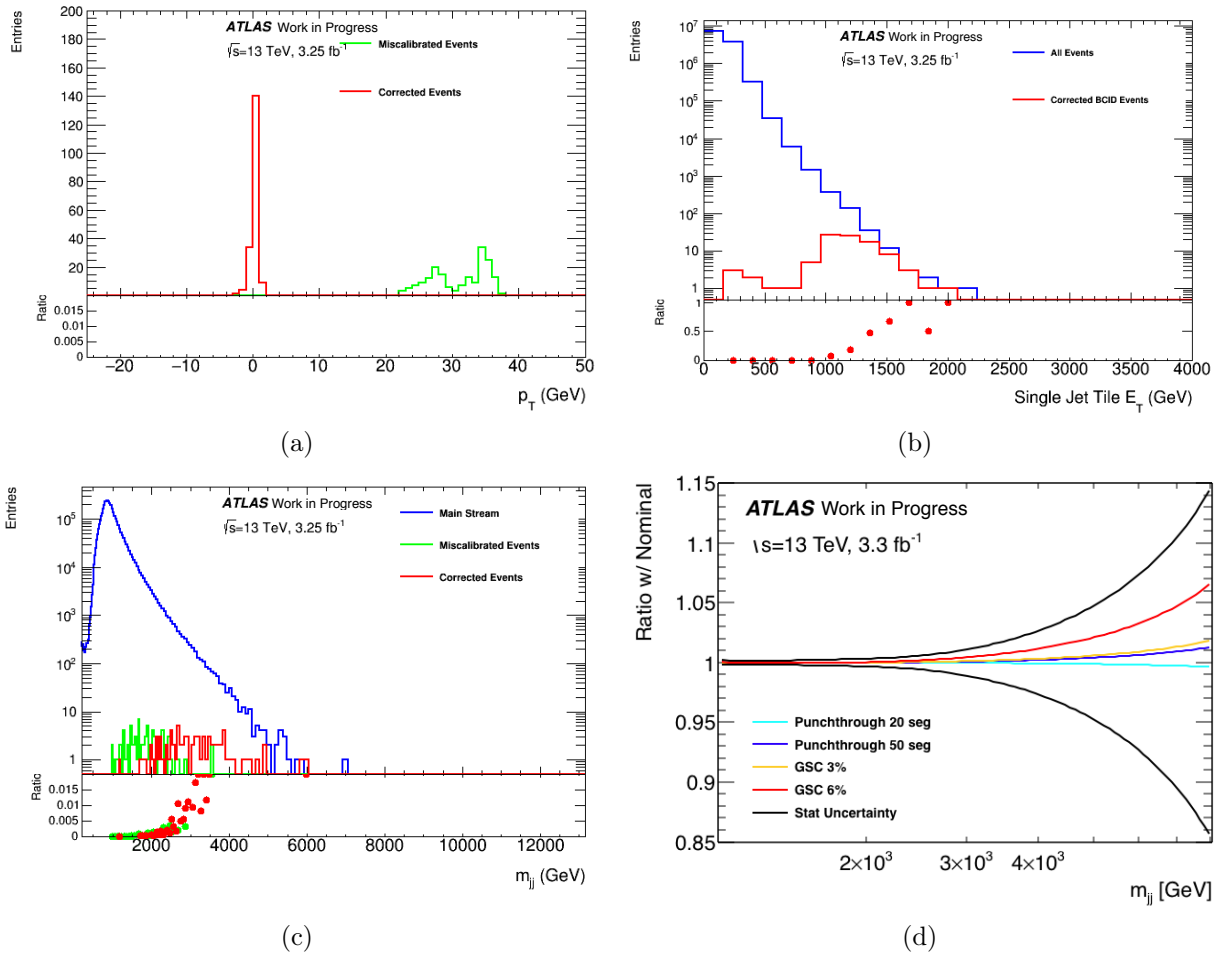

Figure 6.12: The jet timing (a), E_{T} deposited by a single jet in the Tile Calorimeter (b), and m_{jj} (c) are shown for mistimed events. Mistimed events are shown before (green) and after (red) their timing is corrected alongside unaffected events (blue). The event mistiming is found to turn on when a jet deposits more than 500-1000 GeV in the Tile Calorimeter, with a noticeable effect on the jet timing and calculated m_{jj}. The impact of a potential jet miscalibration due to the loss of track-based observables on the background estimation fit is shown in (d). The potential bias from conservatively large shifts in the GSC correction and the number of muon segments is significantly less than the background fit uncertainty.

CHAPTER 7
SEARCHES FOR NEW PHYSICS

The dijet resonance search looks for any resonance from BSM production superimposed on a smoothly falling QCD background. The proper modeling of the QCD background is essential; incorrect modeling could hide real signals or introduce fake spurious signals. The data-driven method for estimating QCD is presented in Section 7.1. Statistical tools locate the region in data of the greatest discrepancy with background estimation and quantify the significance of the excess, detailed in Section 7.2. In case no significant excess is found, limits can be set on the production cross section of new physics, presented in Section 7.3.

7.1 Background Estimation

Background estimation is integral to any search for new physics. A common method for estimating backgrounds is to use Monte Carlo simulation, generated independently from the dataset using theoretical knowledge and past experimental results. MC simulation is used extensively in this analysis to cross-check jet performance and to provide BSM models for analysis studies and limit setting. However it is less reliable when predicting QCD processes due to the large theoretical uncertainties on the parton distribution function and the factorization and normalization scales. These theoretical uncertainties on the NLO jet p_{T} cross section prediction can reach over 10% at 13 TeV [111]. It is also difficult to produce the large statistics required for the QCD spectrum at low p_{T}, reducing the ability to make a confident prediction. Historically, MC simulation has not been used for QCD background estimation in dijet searches.

When MC is inadequate for estimating backgrounds it may appropriate to use a data-driven approach. Simple functions fit to data can provide a valid background estimation and significantly reduce systematic uncertainties. Important considerations for data-driven background estimations include the functional form, the number of parameters, and the fitting method used to find the best parameter values.

7.1.1 Fitting Procedure

The mass spectrum covers a large range of event yield, with tens of thousands of events per bin at small m_{jj} and only one or two events per bin at large m_{jj}. As a consequence common fitting methods which require a minimum sample size in each bin are avoided when possible, including the Pearson χ^2 test [112, 113]. While the uncertainties on the binned data are Poisson, the χ^2 test assumes the error to be Gaussian. For large statistics a Poisson uncertainty can be reliably approximated by a Gaussian, but only if the number of events is larger than ~ 20.

Instead a maximum likelihood estimation (MLE) fit [112,114] is employed, with no Gaussian assumptions made on the errors. The MLE is not used as a direct goodness-of-fit measurement [115] but instead in a likelihood ratio approach between two hypotheses, detailed in Section 7.1.3. The χ^2 test is used to provide cross-checks to the MLE results, generally providing a close approximation, as well as for the initial rejection of a range of fit functions with unmistakably inferior fits.

Fitting is performed using the Minuit [116] routine. The fit proceeds by way of a gradient descent algorithm, relying on first-derivatives to locate the minimum, and in case of failure falls back on the slower but reliable downhill simplex algorithm. Details of the fitting procedure, such as the step-sizes between parameters and the required accuracy of the final parameter values, have been tuned for this analysis using MC simulation.

7.1.2 Functional Form of Background Estimate

The choice of fit function is a key consideration. It should mimic the exponentially decreasing QCD spectrum using the fewest possible parameters. It should include terms which increases with m_{jj}, mirroring the leading order QCD matrix term, while also accounting for the falling PDF with terms proportional to $1 - m_{jj}$. The number of required parameters should be kept to a minimum to avoid overfitting of the mass spectrum and to reduce sensitivity to the presence of narrow resonances. Numerous fit functions were explored using 8 TeV data and 13 TeV MC, and a full list of those considered can be found in Table 7.1.

The best fit function was chosen through MC studies at 13 TeV and is an extension of a function first used by the CDF experiment in 1995 [117]. It has been used successfully since then with the addition of more parameters, most recently by the 8 TeV ATLAS dijet

analysis [16]. That this fairly ad-hoc function, though driven by the matrix element and PDF considerations above, is able to approximate the complex QCD spectrum across many decades of intensity, center-of-mass energies, and detectors with only a few parameters is nothing short of remarkable. The full equation is given by

$$f(x) = p_1(1-x)^{p_2}x^{p_3+p_4\ln x+p_5(\ln x)^2}, \tag{7.1}$$

where $x \equiv m_{jj}/\sqrt{s}$. While 5 parameters are presented in equation Eq. 7.1, it is often seen that fewer degrees of freedom are needed to successfully estimate the background. An initial choice of the nominal fit function assumes only 3 degrees of freedom is necessary ($p_4 = p_5 = 0$). The Wilks theorem is then used to decide if any additional parameters are required.

Name	Description
UA2 (1990) [118]	$\frac{p_1}{m^{p_2}}e^{-(p_3 m+p_4 m^2)}$
CDF (1995) [117]	$\frac{p_1}{m^{p_2}}\,(1-x)^{p_3}$
CDF (1997) [119]	$\frac{p_1}{m^{p_2}}\left(1-x+p_3x^2\right)^{p_4}$
TeV Gravity [120]	$(1-x)^{p_1}\,x^{p_2+p_3 ln(x)}$
Unfixed $\sqrt{s}$ [16]	$p_1\,(1-x)^{p_2}\,x^{p_3+p_4 ln(x)}$ for $x = \frac{m}{p_5}$
Test Fit #1	$p_1\,(1-x)^{p_2}\,x^{p_3 x}$
Test Fit #2	$p_1\,(1-x)^{p_2}\,(1+x)^{p_3 x}$
Test Fit #3	$p_1\,(1-x)^{p_2}\,(1+x)^{p_3\ln(x)}$
Test Fit #4	$p_1\,(1-x)^{p_2+p_3\ln(x)}\,x$
Test Fit #5	$p_1\,(1-x)^{p_2+p_3\ln(x)}\,x^2$
Test Fit #6	$p_1\,(1-x)^{p_2+p_3\ln(x)}\,x^{p_4}$
Test Fit #7	$p_1\,(1-x^{p_2})^{p_3}\,x^{p_4}$

Table 7.1: A list of rejected background parameterizations based on 13 TeV studies with QCD MC simulation. Unless otherwise stated $x = \frac{m}{\sqrt{s}}$. The chosen function is given by Eq. 7.1.

7.1.3 Wilks Likelihood

The comparison between two fit functions on the same dataset is performed according to the likelihood ratio test of the Wilks theorem [121]. The Wilks theorem states that, given the likelihood ratio Λ between two nested functions, the test statistic $-2\log(\Lambda)$ will approach

a χ^2 distribution as the sample size approaches ∞, with the number of degrees of freedom equal to the difference in the number of parameters of the two functions. A conservative requirement is set on the Wilks p-value of 0.05, below which the lower order function is discarded in favor of the higher order function.

The performance of the Wilks test statistic on MC simulation is found to be in agreement with the Sequential Probability Ratio Test [122], an alternative likelihood ratio test, and the F-statistic, a χ^2 based test statistic following the F-distribution [123]. Due to the unique Wilks test requirements, functions not sharing nested parameters with the nominal function (Eq. 7.1 with $p_4 = p_5 = 0$) were rejected using a χ^2 test on MC simulation. Functions formed from extensions of the nominal 3 function were rejected using the Wilks test on MC simulation.

In using Eq. 7.1 it is found from MC studies that the number of parameters required by the Wilks test varies with the luminosity of the data sample. As the statistics of the sample increases the relative uncertainties in each bin decreases, requiring a more accurate parameterization to maintain the same relative performance. Additionally the range of the mass spectrum is extended as the luminosity increases. This was evident in the 8 TeV ATLAS dijet resonance analysis [16] in which the 4 parameter fit function was chosen on a blinded dataset consisting of 25% of the data. Upon unblinding on the full dataset an oscillatory behavior was seen in the significance plot, shown in the bottom panel of Figure 7.1, leading to a low p-value for the fit. The 5 parameter fit function performed better on the full dataset and was taken as a systematic uncertainty on the background prediction. In 13 TeV MC studies it is similarly seen that low luminosity distributions below 5 fb^{-1} require only 3 parameters, while higher luminosity samples require 4 or even 5 parameters.

To account for this behavior an unbiased procedure is developed to choose the appropriate fit function as luminosity is collected. The Wilks procedure is repeated as data is collected and the number of parameters required in Eq. 7.1 is reassessed. This procedure has been tested on both MC simulation and pseudo-data derived from the fit function itself. Pseudo-data generated by four or five parameter functions have their extra parameters set sufficiently far from zero while maintaining the total number of events seen in MC simulation. MC and pseudo-data is generated at various luminosities, and Poisson noise is simulated in the distributions to be coherent across luminosities for each generated seed.

When fitting 3 parameter pseudo-data the performance of the 4 parameter fit is equivalent

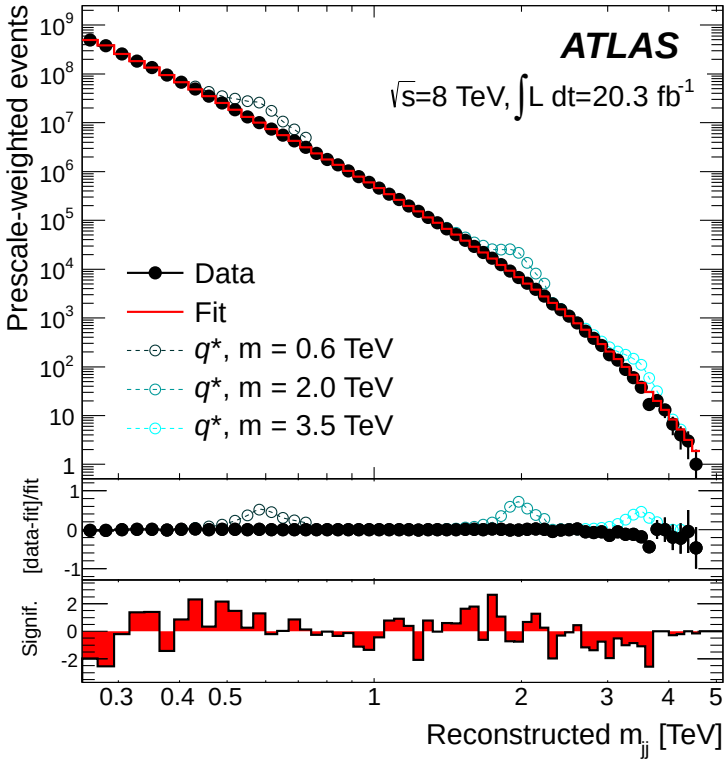

Figure 7.1: The dijet invariant mass spectrum from the 8 TeV dijet resonance analysis [16]. A fit to the data is shown in red alongside the expected size of q^* signals of various masses. A residual plot is shown in the middle panel and the single bin significance of the difference is shown in the bottom panel. The oscillatory pattern seen in the significance plot is an indication of a poor fit.

to the 3 parameter fit regardless of luminosity, as expected. The Wilks statistic for the 4 vs 3 parameter functions, as shown in Figure 7.2(a) in brown, therefore stays well above the 0.05 p-value threshold. The same is true when comparing the 5 vs 3 parameter functions, shown in blue. However when fitting the 4 parameter pseudo-data both the 4 and 5 parameter Wilks statistics quickly drops after 1 fb^{-1}, as shown in Figure 7.2(b), demonstrating the inadequacy of the 3 parameter fit function with respect to higher orders. This inadequacy is not apparent at low luminosities where relative bin uncertainties are large and high mass events have not appeared. Studies with MC simulation show a switch from 3 to 4 parameters between 3 and 10 fb^{-1}, though is not necessarily predictive of the behavior in data.

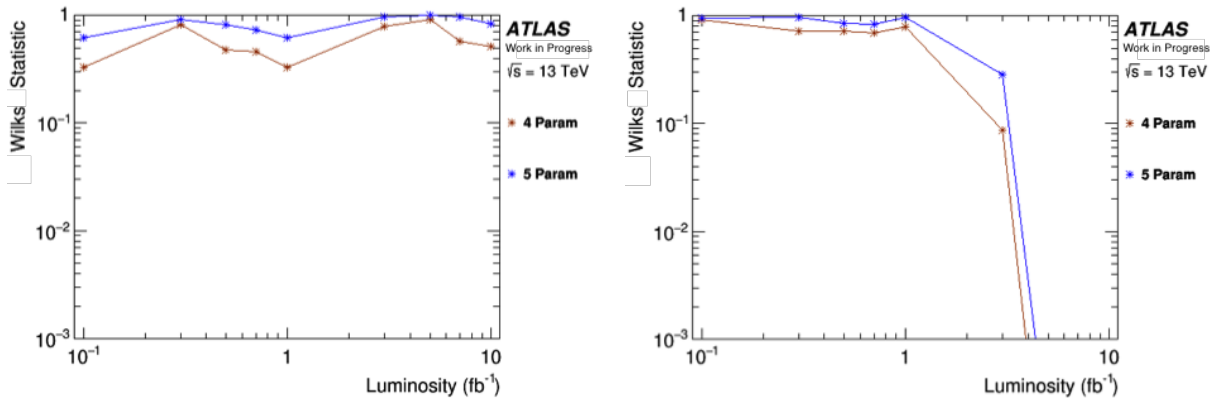

(a) 3-parameter pseudo-data

(b) 4-parameter pseudo-data

Figure 7.2: The Wilks p-value as a function of luminosity for pseudo-data generated from 3 parameter (a) and 4 parameter (a) functions. The curve in brown is the comparison between the 3 and 4 parameter fits, and indicates that the 3 parameter function is sufficient for all luminosities in (a) but only below 1 fb^{-1} in (b), as expected. The same behavior is shown in the 3 vs 5 parameter comparison in blue.

7.1.4 Systematic Uncertainties

Systematic uncertainties take into account any bias that may be introduced to the background estimation. Typical theoretical uncertainties involved in MC simulation are unnecessary on the data-driven estimate and are replaced by uncertainties on the parameterization. Jet energy scale uncertainties are also unnecessary as they are absorbed into the data-driven estimate. The impact of the JES uncertainties on the fit function choice of the Wilks procedure was found to be negligible, as shown in Figure 7.3, indicating that the fit function choice would not depend on these uncertainties below 20 fb^{-1}.

Systematic uncertainties on the background distribution are derived from the choice of fit function and from the uncertainty of the best fit parameters. Uncertainties on the parameters reflect the quality of the fit, and while they may be derived through the covariance matrix this method could suffer from strong correlations in the fitted parameters. Instead they are determined from Poisson-fluctuated pseudo-experiments generated from the background estimate. Each of the ∼10,000 pseudo-experiments are refit and an RMS is calculated from the per-bin differences in yield of the fits and the nominal fit. A 1σ confidence interval is generated from this RMS representing the region in which the majority of background estimates for repeated trials would fall.

The choice between two fit functions which both accurately describe the data is arbitrary

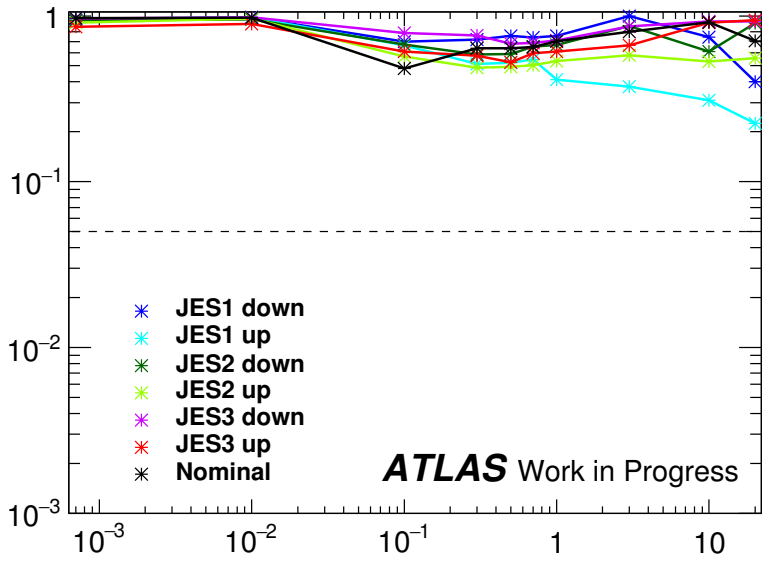

Figure 7.3: The Wilks p-value is shown as a function of luminosity using MC simulation with the various JES uncertainties applied (colored) as well as the nominal result (black). No change in the fit function choice is seen up to 20 fb^{-1}.

and their difference is taken as a systematic uncertainty. This was an important systematic in the 8 TeV dijet analysis as the nominal 4 parameter function was found to be inadequate after unblinding. Pseudo-experiments are thrown from the data distribution and the difference between the nominal and alternative fit functions is found for each. The RMS of the difference for each bin is taken as a 1σ uncertainty.

7.1.5 Spurious Signal

A poor fit could lead to spurious signals in which correlated differences persist over several bins and mirror a true signal. Oscillatory behavior in the ratio of data to the QCD prediction is an example of such behavior, as shown previously in Figure 7.1. Two methods have been used to estimate the probability of a false discovery from spurious signals. The spurious signal for both is taken as the discrepancy between the 3 parameter fit function and the MC spectrum when no Poisson fluctuations are introduced. With no fluctuations the MC simulation is found to require more than 3 parameters in the fit, and differences with the fit are correlated across bins, providing a worst-case scenario.

In the first method the size of the spurious signal is compared to the Poisson uncertainty of the background as well as the expected size of a true signal at 1 fb^{-1}. In Figure 7.4 the number of spurious signal events above the background estimate is shown in black, presenting a small effect that is spread across many bins and not localized in m_{jj} as expected of a true signal. It is significantly smaller than the Poisson uncertainty, shown in red, and the number of expected signal events from the benchmark q^* model, shown in open circles for various masses. At no point is the number of spurious signal events more than 20% of the statistical uncertainty or 20% of the number of expected signal events, such that a spurious signal would not present a false discovery.

A second method passes the spurious signal through the analysis search machinery (Section 7.2). The global p-value returned by the search machinery measures the probability of seeing the spurious signal assuming the background estimate is true. A p-value of 1 is returned, demonstrating compatibility with the background estimate and the insignificance of the spurious signal.

7.1.6 Fitting in Presence of Signals

While the fitting procedure has been shown to limit the possibility of spurious signals it still remains a question as to whether it may hide a true signal and return a false negative. The number of parameters in the fit function is kept to a minimum to prevent introducing extra degrees of freedom that can fit to a narrow signal. Any resonance will still affect the fitting procedure, potentially hiding the signal or reducing the sensitivity. A special procedure is used to ignore regions of m_{jj} with potential signal contamination.

During the search phase any regions of discrepancy between data and the background estimation are located. If a region returns a global p-value of 0.01, a loose requirement that may happen even without a true signal, that region is excluded from the fit and the search phase is repeated. The size of the exclusion region can be expanded by repeating the procedure for both sides of the mass spectrum around the exclusion region. An adjacent bin is excluded if either side returns a p-value of 0.01 and the procedure begins again. Optimization studies have shown that once the full exclusion region is found a small amount of signal contamination will likely remain on the lower m_{jj} edge of the exclusion region, and therefore an extra bin is removed from this edge. The search phase can then be repeated

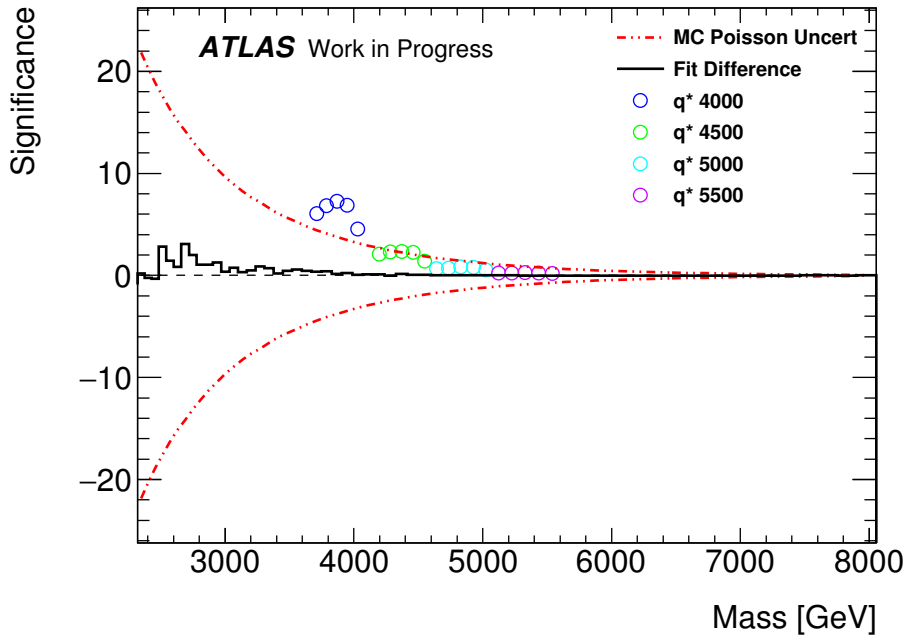

Figure 7.4: The spurious signal (solid curve), derived from a 3 parameter fit to non-Poisson fluctuated MC simulation, is compared against the QCD Poisson uncertainty (dot-dash curve) and expected q^* signal (open circles) for various mass points at 1 fb^{-1}. The spurious signal is less than 20% of both the Poisson uncertainty and expected signal yield and is unlikely to present a false discovery. The plot is limited to m_{jj} above 2.4 TeV as there are too few events simulated in MC below this region, leading to large Gaussian uncertainties that would bias the result.

with a background estimate that is unbiased by the exclusion region.

7.2 Search Strategy

The search strategy proceeds by identifying an invariant mass region in data of largest discrepancy with the background estimate. The significance of this discrepancy is compared to that of excesses expected from purely statistical fluctuations. The BumpHunter algorithm [124] is used to identify the region of largest discrepancy and provide a local p-value of its significance. The procedure using 3 fb^{-1} of MC simulation as data is presented in Figure 7.5 to provide a pictorial example of each stage of the process. This robust search procedure has been practiced under numerous conditions and is found to be insensitive to JES uncertainties as well as to the fractional contribution of gg, gq, qg, and qq processes to the QCD background.

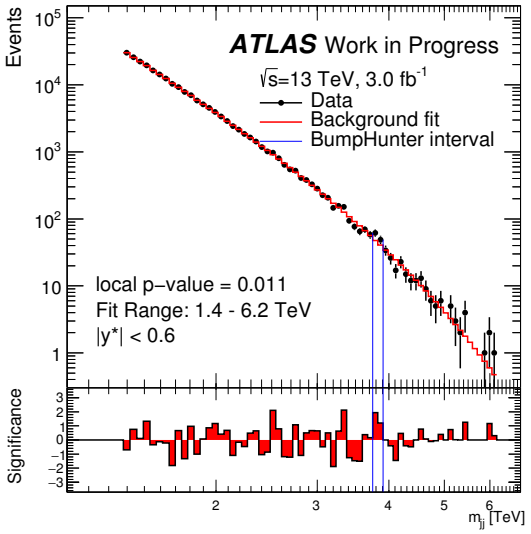

(a) Search Phase Example

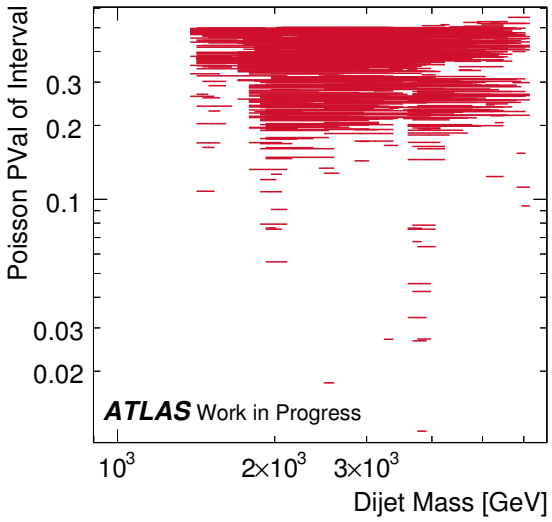

(b) P-value per Range

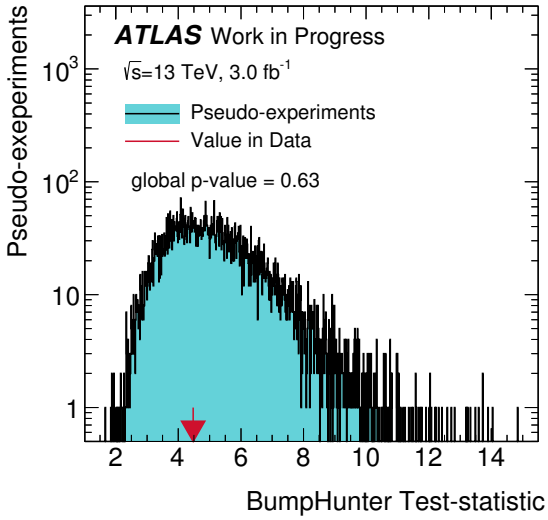

(c) Test Statistic for Toys

Figure 7.5: A set of figures from the search phase performed on 3 fb^{-1} of QCD MC simulation. These figures are an example of the search phase in practice, and the final results using 13 TeV data are presented later in Section 8.2. (a) The local p-value of each mass window is calculated, shown here for the most significant mass window bracketed in blue stripes. (b) The local p-value from all mass windows are compared, with each mass window shown spanning its corresponding range. The most significant mass window is used in the BumpHunter test statistic. (c) The BumpHunter test statistic is shown for pseudo-experiments (black and blue) and for data (red arrow). Lower values of the BumpHunter test statistic correspond to better agreement with background expectations, and the global p-value of 0.63 seen in data is compatible with Poisson fluctuations.

To locate the region of greatest significance every possible invariant mass window is checked, starting from two consecutive bins and extending to half the invariant mass spectrum of the data, and every window size in between. For each mass window a local p-value is calculated as the probability of a Poisson fluctuation of the background estimate matching the number of events seen in data, as given by Eq. 7.2. Small local p-values are given if the number of data events in the mass window, d, is much larger than the number of expected background events, b. A p-value of 1 is given if $d < b$.

$$P(d, b) = \sum_{n=d}^{\infty} \frac{b^n}{n!} e^{-b} \text{ if } d \geq b \tag{7.2}$$

This procedure is shown for a 2 bin region in Figure 7.5(a). The local p-values of all possible mass windows are calculated and are compared in Figure 7.5(b). Here the local p-value of each window is plotted as a function of its mass range. In the example the most significant local p-value, p^{min}, of 0.011 is found to be in the 2 bin region near 4 TeV. A vertical trend can be seen where the excess of the significant 2 bin region causes local excesses in included 3 or 4 bin regions, though of smaller significance.

While this local p-value may by itself be considered a significant fluctuation it is only found after scanning all possible mass ranges. Given the large number of regions there is a high probability that at least one of them has a significant Poisson fluctuation, even without the presence of signal. It is therefore important to compare our results against the expectations of finding such a significant local p-value from statistical fluctuations only. In this way a global p-value will consider the many mass regions of our search and account for the look-elsewhere effect [125].

The BumpHunter search strategy is repeated on ∼10,000 pseudo-experiments, each drawn from the background prediction and with bin-by-bin Poisson noise fluctuations applied. A distribution such as Figure 7.5(b) is generated for each pseudo-experiment, and p^{min} is identified. To facilitate comparison of p^{min} between pseudo-experiments and data, a test statistic t is calculated according to Eq. 7.3. The form of the test statistic is chosen such that $t \geq 0$ always and is increasing in magnitude as p^{min} becomes smaller and more significant.

$$t = -\log(p^{min}) \tag{7.3}$$

The test statistics derived from data and the pseudo-experiments are compared as shown in Figure 7.5(c). A global frequentist p-value is established as the fraction of times the data result would occur in repeated experiments if the background hypothesis were true. If the global p-value is found to be above 0.01, then the likelihood of the fluctuation in data occurring in repeated experiments is greater than 1%. In this scenario no discovery would be claimed and limit setting would proceed. If the global p-value is below 0.01 an exclusion region is defined, as explained previously in Section 7.1.6, and the procedure is repeated.

7.3 Limit Setting

If no evidence of new physics is found during the search phase then limits may be set on the production of new physics. A limit on a BSM model corresponds to the maximum number of signal events in data that would still be compatible with the background estimation. The limit therefore corresponds to the production cross section, proportional to the signal strength μ, of a model which cannot be rejected given the data.

A Bayesian statistical approach [126] is taken to predict the likelihood of observing the collected data given a specific hypothesis. A hypothesis consists of the data-driven background estimate with an injected signal model, and numerous hypotheses are created for each signal model at various mass points. Given a specific hypothesis H and the dataset d, the conditional probability of the hypothesis given the data is defined as

$$P(H|d) = \frac{P(d|H)\pi(H)}{\pi(d)} \tag{7.4}$$

The probability of the data given the hypothesis $P(d|H)$ can be calculated using the MC signal models with the prescription detailed below. The prior probabilities of data $\pi(d)$ and the hypothesis $\pi(H)$ reflect the prior knowledge. The $\pi(d)$ is independent of any hypothesis and therefore amounts to a normalization factor that may be ignored. The $\pi(H)$ reflects the current belief in the hypothesis and how it would appear in our detector.

7.3.1 Confidence Limit Calculation

Assuming that a hypothesis is only dependent on the μ of the signal model, the probability of the hypothesis given our data may be written as a function of the likelihood $L(d|\mu)$ as

$$P(\mu|d) \propto L(d|\mu)\pi(\mu) \tag{7.5}$$

To prevent any bias there is no assumption made on the prior of the variable of interest μ. A flat, non-informative signal prior $\pi(\mu)$ is used and limited to a large range about the predicted sensitivity. The use of a non-informative prior ensures the posterior is decided entirely by the data. The flat prior helps facilitate the comparison and reinterpretation of results and leads to identical posteriors as measured by a Frequentist CLs method.

The likelihood $L(d|\mu)$ of Eq. 7.5 is calculated between binned distributions of the data and the signal+background hypothesis, such that

$$L(d|\mu) = \prod_i \text{Pois}(N_d, N_b(\mu)) \tag{7.6}$$

where $\text{Pois}(N_d, N_b)$ is the Poisson probability of observing more than N_b background events given a Poisson distribution with event rate parameter $\lambda = N_d$. The product is taken over each m_{jj} bin i to calculate the final likelihood.

Given the posterior probability of Eq. 7.5 a Bayesian credible interval is defined as the region in which there is a 95% probability to contain the true value of μ. A confidence limit on the maximum number of expected signal events μ_{up} can be found by integrating the posterior density to the desired confidence level of 95%,

$$0.95 = \int_0^{\mu_{up}} p(\mu|d)d\mu. \tag{7.7}$$

Therefore a predicted limit on the signal strength of a model will be less than μ_{up} with a 95% probability.

7.3.2 Marginalization

Assuming a hypothesis that is solely dependent on μ, the procedure outlined above would be sufficient for setting limits. However the hypothesis is not only dependent on the μ of the signal model but also on systematic uncertainties on our dataset, MC modeling, and detector uncertainties which can vary the number of expected events. Each systematic uncertainty λ_i is treated as a nuisance parameter in our hypothesis, which may be fully described by the

parameters $\mu, \lambda_1, \lambda_2, ... = \mu, \boldsymbol{\lambda}$. Each nuisance parameter can be assumed to be independent of μ and the other nuisance parameters, either by their definition or, in the case of the jet energy scale components, by construction. Each independent nuisance parameter can therefore be integrated out of the probability defined in Eq. 7.5, giving

$$P(\mu|d) \propto \int L(d|\mu, \boldsymbol{\lambda})\pi(\mu) \prod_i \pi(\lambda_i) d\boldsymbol{\lambda} \tag{7.8}$$

Bayesian marginalization [127] is used to integrate over the nuisance parameters $\boldsymbol{\lambda}$. Each nuisance parameter represents some measurement with calculated uncertainties and are given a Gaussian prior. A numerical calculation of Eq. 7.8 is performed by finding the set of nuisance parameter values for a fixed μ which maximize the probability $P(\mu|d)$. A posterior distribution can also be calculated for each individual nuisance parameters by marginalizing over the others and μ. It can be directly compared to the assumed prior distribution. The prior and posterior distributions for the luminosity uncertainty and the fit quality uncertainty are shown in Figure 7.6 using a partial 13 TeV dataset of 80 pb^{-1}. Good agreement is shown between the assumed prior and calculated posterior for the luminosity uncertainty, while the fit quality prior is overly conservative as the fit function describes the data better than expected. In both cases the nuisance parameters prefer the central values as predicted.

The μ posterior density, shown in Figure 7.6(c), has a preference for very few signal events, as expected given the small luminosity in this example. An integration of Eq. 7.7 is performed on this distribution, with the 95% quantile shown by a vertical blue line at 6 events. A limit of six events given 80 pb^{-1} may therefore be claimed.

The marginalization is performed through the Bayesian Analysis Toolkit [128] which takes in histograms of the data, the combined signal and background, and pairs of histograms which represent $\pm 1\sigma$ systematic shifts to the signal+background. Care is taken to distinguish between systematics which

- produce a mass-dependent shift in the signal+background template,
- alter the shape of the spectrum through event migrations across bins,
- and scale the overall normalization of the spectrum.

The template shifting systematics include the uncertainty on the fit quality and the function choice. These change the inherent mass distribution but only retain their meaning if

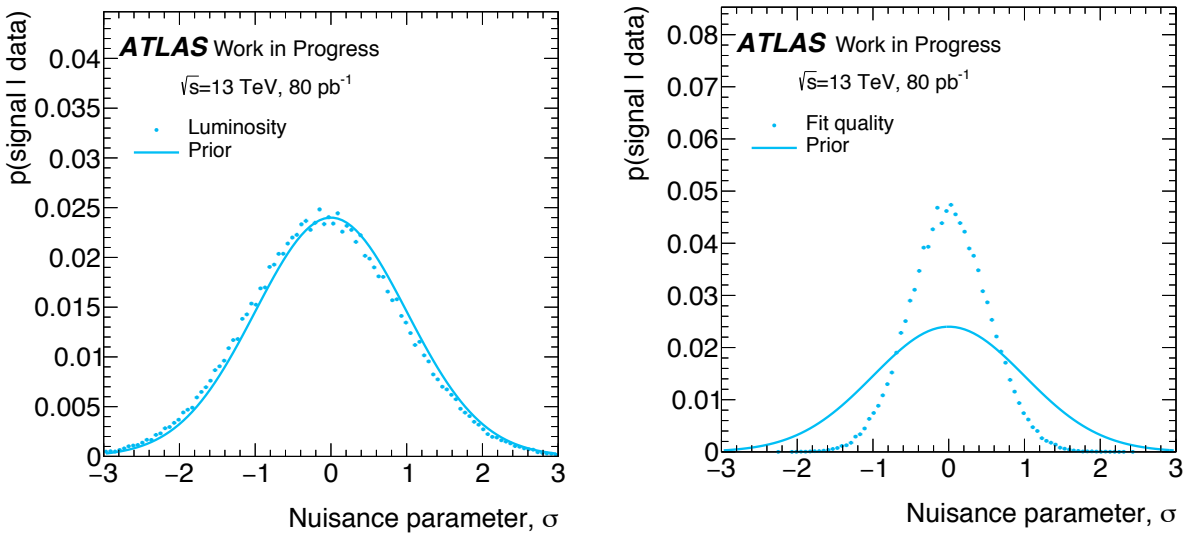

(a)

(b)

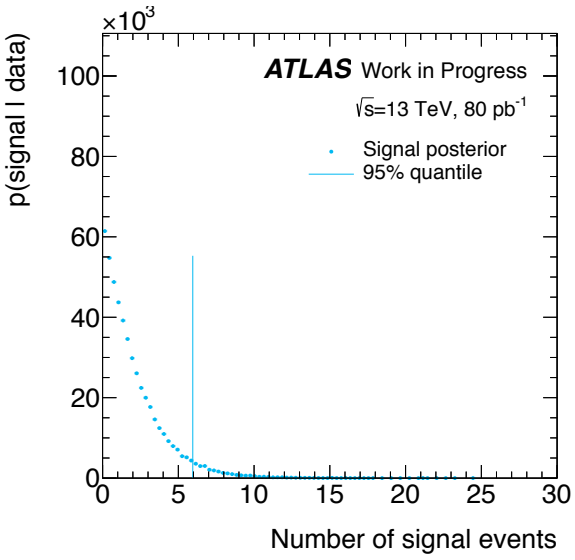

(c)

Figure 7.6: The marginalization procedure is tested on the first 80 pb^{-1} of 13 TeV data corresponding to 2% of the entire 2015 dataset. The hypothesis is taken to be the best fit background estimation using the 3 parameter fit function with an injected 4 TeV BlackMax signal model. Prior (solid) and posterior distributions after marginalization (dotted) are shown for the luminosity (a), fit quality (b), and signal strength (c). The 95% quantile of the signal strength (c) is demarcated with a vertical blue line.

applied to the nominal distribution from which they were derived. They must be applied prior to any shifting of events cause by shape-altering systematics. A new template is calculated

at every 0.5σ shift between -3.5σ and 3.5σ to allow for the proper linear extrapolation of the parameter λ_i at any value between -3σ and 3σ. At each step the nominal and varied distributions are normalized to 1 and an adjustment is calculated for each bin. The total template systematic shift is the sum of the two binning adjustments for the fit quality and function choice.

Shape-shifting systematics include the three JES nuisance parameters. They correspond to the shifting of events between bins more than the addition or subtraction of any events from the analysis. While shape-shifting systematics could also be treated with templates that simulate any horizontal shift over the parameter range, it would neglect their interference and introduce a dependency to the order in which they're applied. Instead a transfer matrix is derived for each NP to simulate the effect of the shift in each bin for various parameter values. Each transfer matrix is calculated with parameter steps of 0.5σ, with intermediate bin migrations taken by a linear extrapolation. Through MC simulation studies the product of the three transfer matrices is found to be a reliable estimate of the final bin content shifts due to the individual effects of each jet energy scale uncertainty.

The scale-changing systematics are the last to be applied and consist of the luminosity uncertainty and PDF acceptance uncertainty. These correspond to the addition or subtraction of events in a mass-independent manner and are therefore applied as a total normalization change to the entire signal+background template. The shifts are extrapolated from a single shift calculated at $+1\sigma$.

Given the above prescription a mass spectrum can be generated for any parameter value between -3σ and 3σ. The likelihood of the data given the hypothesis required by Eq. 7.6 can then be calculated as

$$L(d|\mu, \boldsymbol{\lambda}) = \prod_i \mathrm{Pois}(N_d, N_b(\mu, \boldsymbol{\lambda})) \tag{7.9}$$

for various values of $\boldsymbol{\lambda}$.

The numerical calculation of the Bayesian marginalization is performed by the Markov chain Monte Carlo method [129] within the Bayesian Analysis Toolkit. The algorithm proceeds by randomly selecting a set of initial parameters and calculating the likelihood with the input histograms. A new set of parameters is chosen through the Metropolis algorithm [129] and are accepted or rejected based on the improvement to the posterior probability $p(\theta|d)$. Through this method many parameter sets may be tested with a focus on the phase-space

of interest. The process is repeated for several different seeds using new initial parameter sets and the process is run until the seeds converge on the correct target distribution. The posterior distributions after marginalization for several parameters was shown previously in Figure 7.6.

7.3.3 Limit Representation

A limit plot describes the possible number of signal events in the data distribution that reflects a convolution of the cross section, detector acceptance, and branching ratio ($\sigma \times \mathcal{A} \times$BR). The marginalization proceeds for several mass points in a signal sample and a linear extrapolation is performed between mass points. While the observed limit is calculated with respect to the dataset, an expected limit may also be derived using Poisson fluctuated pseudo-data derived from our background estimation. The expected limit reflects the potential of the analysis to reject BSM models given a background estimate with no signal injected. By using multiple pseudo-datasets with different random fluctuations the sensitivity of the analysis to noise can also be established. The pseudo-datasets are treated identically to data and the various quantiles provide a 1 and 2σ band around the average expected limit. The observed and expected limits are shown in Figure 7.7(a) for the sample dataset of 80 pb^{-1}, assuming the benchmark q^* model.

The observed and generated limits on $\sigma \times \mathcal{A} \times$BR are compared to curves of the theoretically calculated cross section as a function of mass for each BSM model. The intersection of the curves provides an upper mass limit for which that signal model is excluded.

A model-independent limit is also provided through the use of generic Gaussian resonances of various width. These model-independent limits do not reflect the shape or width assumptions of specific models and are useful for recasting limits for new theoretical models which were not explicitly checked by the analysis. Gaussian resonances are generated at various widths of 7%, 10%, and 15% of the mean, and at the detector resolution, as shown in Figure 7.7(b). The detector resolution is taken to be the width of each bin, reflecting the resolution calculated in Section 6.2. The limit generally degrades as the resonance width increases and the signal is spread across multiple bins, and the effect of statistical fluctuations is similarly reduced. As no branching ratio is assumed the limits are presented as $\sigma \times \mathcal{A} \times$BR.

The Gaussian resonances are trimmed to the central 95% of their distribution to remove

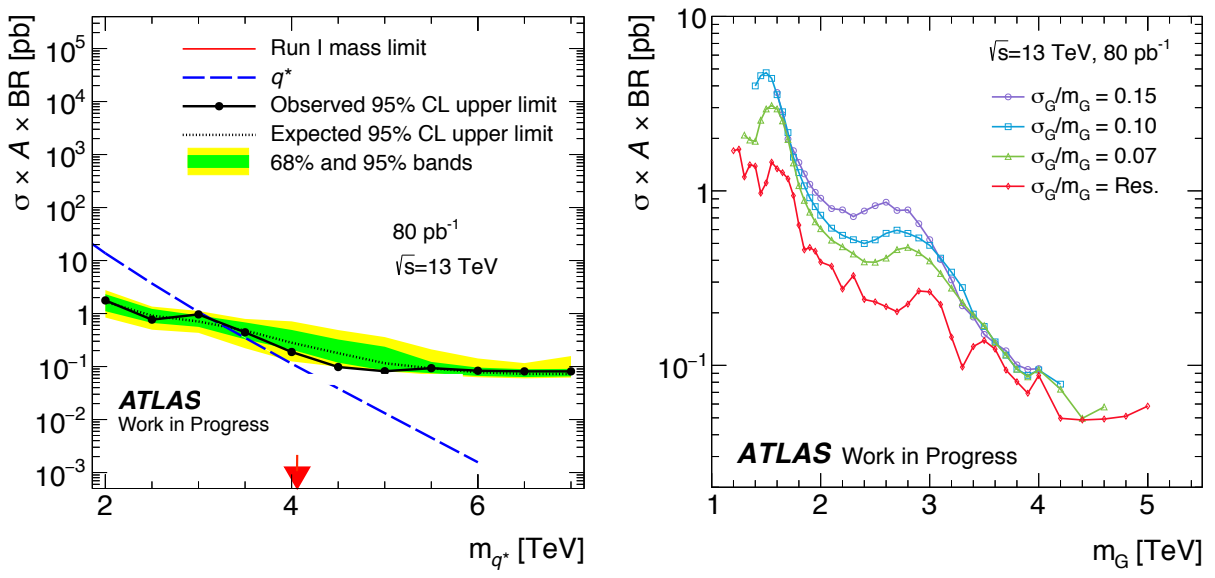

(a) (b)

Figure 7.7: Example limits are set using the first 80 pb^{-1} of 13 TeV data corresponding to 2% of the entire dataset. (a) For the q^* benchmark model the observed (solid) and average expected (dotted) limit curves agree within the 68% (dark) and 95% (light) confidence interval bands on the expected limit. The intersection of the observed limit and the theoretical cross section curve (dotted blue) presents a lower mass limit on q^* of about 3.2 TeV, compared against the Run 1 mass limit (red arrow). (b) Model-independent limits are set using Gaussian resonances generated with widths of 7%, 10%, and 15% of the mean, as well as at the detector resolution (Res.) derived in the binning procedure of Section 6.2.

undesirable effects in the tails. They are passed into the limit setting machinery and treated identically to the MC signal templates. The minor acceptance uncertainties associated with the PDF are ignored in favor of the larger luminosity uncertainty.

The Gaussian resonances are only a representation of mass resonances and are not calculated through jet four-vector objects. They therefore can not have the nominal jet energy uncertainties applied. Instead a single simplified jet energy scale nuisance parameter is estimated. At each point the q^* template of the nearest mass point is chosen and a 3σ jet energy scale variation is applied to all jets. The shift in the mean of the q^* peak is taken as the uncertainty to be applied to the Gaussian resonance. The effect on the width of the resonance is not considered. This procedure corresponds to the variation bracketing of the full jet energy scale shift and reaches 9% at high masses.

The Gaussian limits may be used to infer limits on other BSM theories not explicitly tested in this analysis. The candidate BSM model must have a mass distribution approxi-

mating a Gaussian in shape after the application of jet p_{T}, m_{jj}, and y^* selections. A full prescription for recasting models is given in Ref. [16].

CHAPTER 8
RESULTS

The results of the dijet resonance search are presented below. A review of the 13 TeV data is presented in Section 8.1. The search phase, consisting of the final background estimation and the search for localized excesses in the data distribution, is presented in Section 8.2. Details of the background estimation techniques were previously presented in Section 7.1, and on the search phase in Section 7.2. The results of the limit setting procedure, described in detail in Section 7.3, is given in Section 8.3.

8.1 Run 2 Dataset

The Run 2 dataset consists of 3.6 fb^{-1} of 13 TeV collisions taken in 2015. The events have all passed the quality criteria of each ATLAS subdetector described in Section 6.1. Each run was cross-checked against MC simulation, described in Section 6.3, with event observables appearing as expected. The analysis jets were required to be of good quality and pass the cleaning criteria given in Section 5.3. Dedicated studies of high-p_{T} jets were performed, described in Section 6.3.2, and gave confidence to the calibration of TeV-scale jets.

Special attention was given to data for which the inner pixel layer IBL was turned off, the bunch-spacing was set to 50 ns, and in which an excess of muon segments caused delays in the event reconstruction. No defects were found in these data samples, each reviewed in Section 6.4, and they are included in the analysis. The high-p_{T} jets that caused the L1Calo trigger to saturate had their timing corrected and their energies validated, as described in Section 6.4.4.

The 13 TeV dataset includes dijets of larger masses than ever observed before and significantly improves the statistics of past searches for masses larger than 2 TeV. At 8 TeV the highest dijet event had a mass of less than 4.5 TeV; at 13 TeV there were tens of events in bins of a similar mass with only 1/6th of the collected luminosity. The highest mass central dijet event recorded is found at 6.9 TeV and is displayed in Figure 8.1. It consists of two well-balanced, central jets each with p_{T} of 3.2 TeV. Each jet is associated with a large number of tracks and deposits a large amount of energy in the EM and hadronic calorimeters. An alternative view given in Figure 8.2 shows the full magnitude of the energy deposited in the calorimeter by both jets, dwarfing smaller energy deposits caused by pile-up jets.

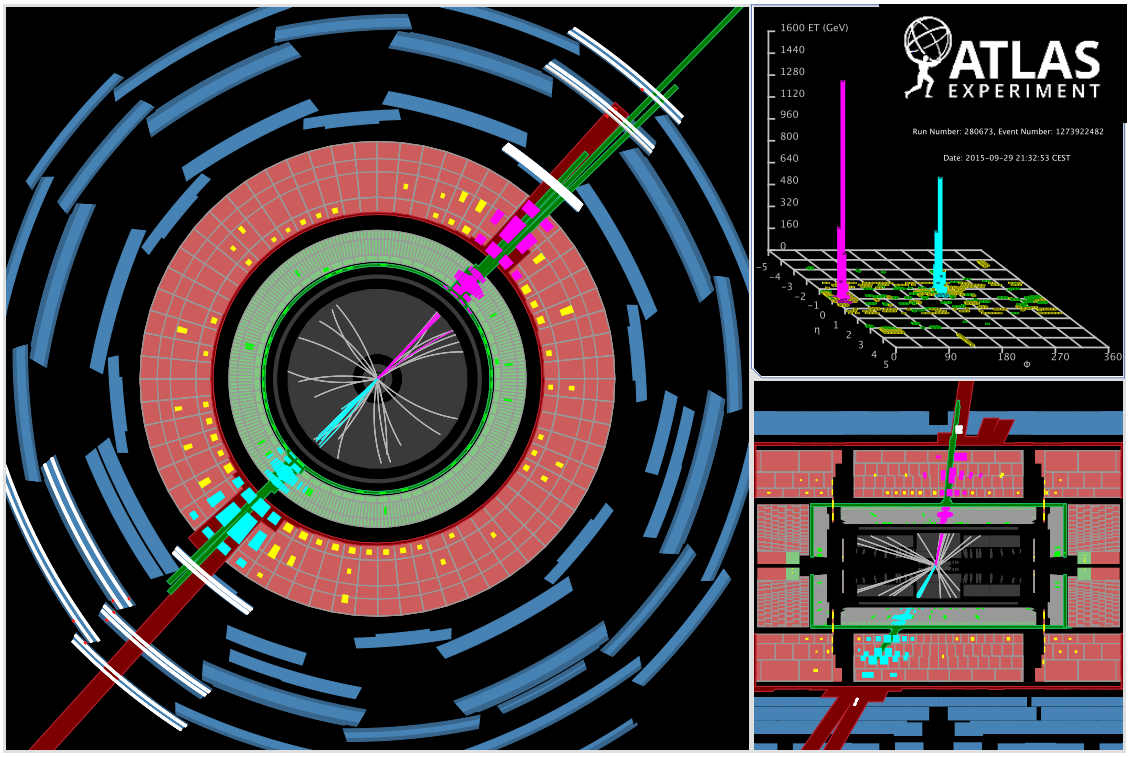

Figure 8.1: An event display of the highest mass dijet event yet to be observed within $y^* < 0.6$ as of the time of publication. The three detector views are (clockwise from left) a cross section of the ATLAS detector as seen from the beamline, the magnitude of the deposited energy in the calorimeter cells in the $\eta \times \phi$ plane, and a cross section of the ATLAS detector as seen from the x-axis. The response of various subdetectors is simulated as grey tracks in the inner detector, as green bars in the LAr calorimeter, and as yellow and red bars in the Tile Calorimeter. The size of the calorimeter bars is proportional to the amount of energy deposited in any given cell. The tracks and calorimeter cells associated with the first (second) jet are colored in purple (blue). Each jet has a p_{T} of 3.2 TeV with a combined invariant mass of 6.9 TeV. The amount of missing transverse momentum is minor at 46 GeV.

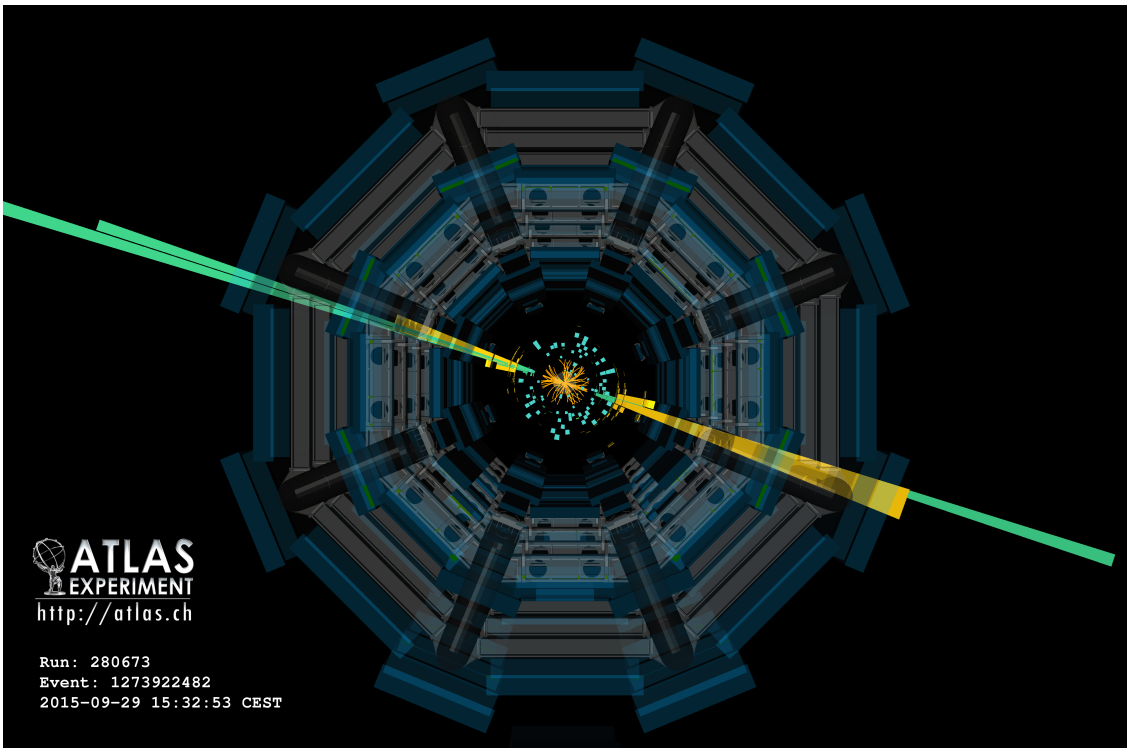

Figure 8.2: An event display of the highest mass dijet event yet to be observed within $y^* < 0.6$ as of the time of publication. The event is viewed from the beamline upstream of the detector. The response of various subdetectors is simulated as orange tracks in the inner detector, as green bars in the LAr calorimeter, and as yellow bars in the Tile calorimeter. The size of a calorimeter bar is proportional to the amount of energy deposited in the given cell. Each jet has a p_{T} of 3.2 TeV with a combined invariant mass of 6.9 TeV. The amount of missing transverse momentum is minor at 46 GeV.

8.2 Search Results

The nominal background estimate is found through the best log-likelihood fit using the three parameter function

$$f(x) = p_1(1-x)^{p_2}x^{p_3}, x \equiv m_{jj}/\sqrt{s} \tag{8.1}$$

The fit to the full 3.6 fb^{-1} dataset begins at the m_{jj} trigger threshold of 1.1 TeV and ends at the last data point of 6.9 TeV. The best fit of the nominal fit function and its fit quality errors are shown in Figure 8.3(a). The alternative 4 parameter and 5 parameter fit functions are also plotted but are nearly indetectable due to the good agreement. The deviation of the fit from the data, across the entire mass spectrum, is shown in the bottom panel of Figure 8.3(a).

The Wilks procedure is assessed after each run and is shown in Figure 8.3(b) as a function of the luminosity collected. The Wilks p-value between the nominal and 4 parameter fit functions are shown in blue and never cross the established 0.05 p-value threshold. For the final 3.6 fb^{-1} the Wilks p-value is 0.767, demonstrating that the nominal fit function sufficiently describes the data without the need for more parameters.

The nominal background estimate and its final uncertainties are shown in Figure 8.3(c). The fit function choice uncertainty is derived as the difference between the 3 and 4 parameter fits, as shown in Figure 8.3(a). The fit quality uncertainty, a measure of the total uncertainty on the 3 fit parameters, is also shown out to ∼7.1 TeV. It can be seen from the lower panel of Figure 8.3(c) that the fit quality uncertainty is dominant at masses below 4 TeV. The fit function choice is dominant at higher masses, rising to 25% at ∼7.1 TeV. While the relative uncertainty is large at higher masses the number of expected events is small, such that absolute uncertainties on the number of events is less than one.

The search phase is performed with BumpHunter using the final background estimate. The most significant deviation of the data from the fit is found to be the two bins between 1.53 and 1.61 TeV, with a local p-value 0.01 as shown in Figure 8.4. The expected signals from a 4 TeV q^* (with cross section σ scaled by a factor of 3) and a 6.5 TeV quantum black hole are also shown.

Two additional plots are given in the bottom panels of Figure 8.4 to demonstrate the agreement of data with background expectations. The middle panel presents the difference, in units of standard deviation, between the data and the fit, considering only statistical

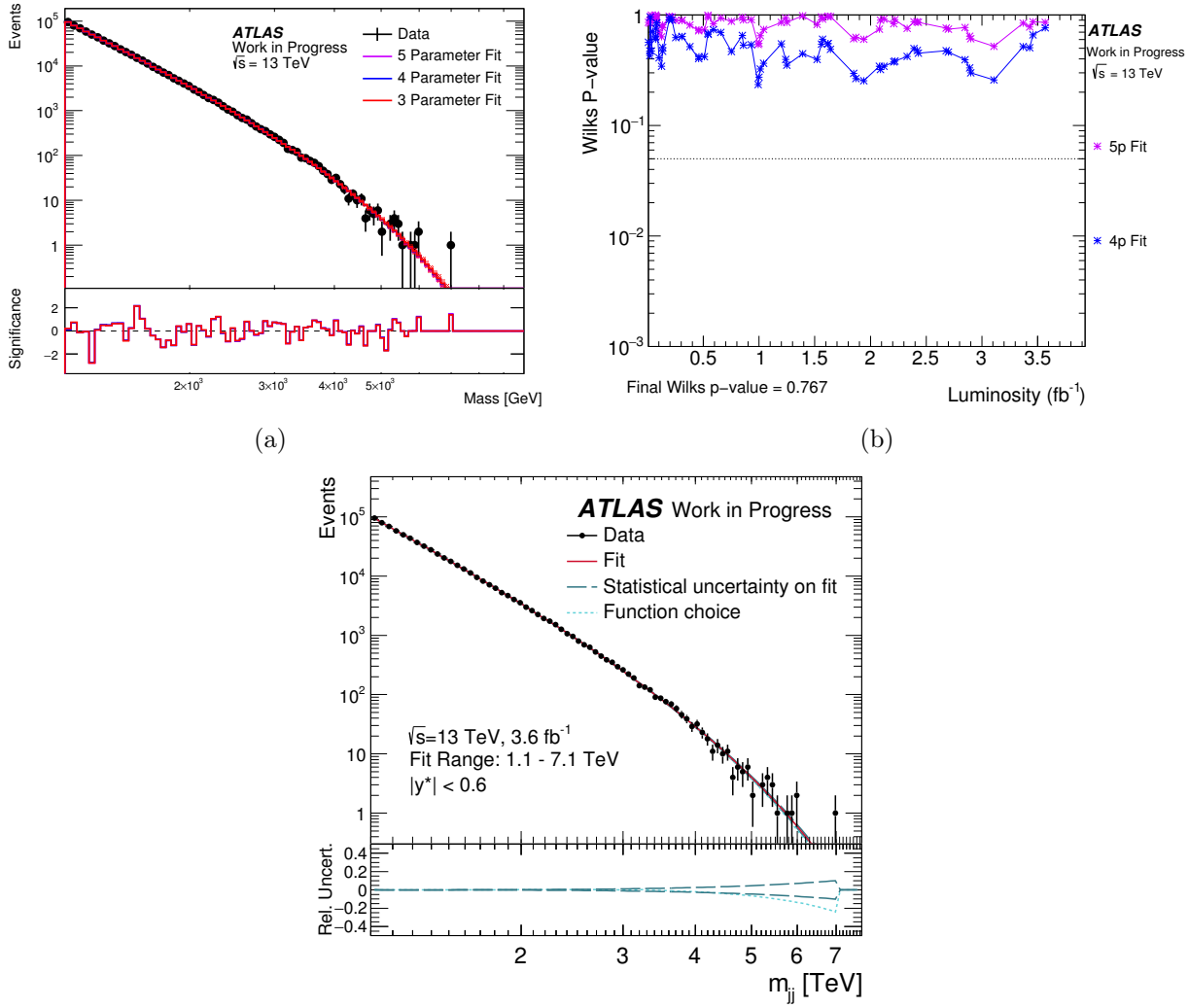

(a) (b)

(c)

Figure 8.3: (a) A direct comparison of the nominal 3 parameter fit function (red) against the alternative 4 (blue) and 5 (purple) parameter fit functions with hashed error bars corresponding to the fit quality uncertainty. The alternative fits are nearly indetectable due to the good agreement with the 3 parameter fit. The bin-by-bin significance between the data and the fits is shown in the lower panel. (b) The Wilks p-value of the 4 (dark blue) and 5 (light purple) parameter fits as a function of collected luminosity is always above the 0.05 threshold, suggesting that 3 parameters is sufficient to describe the data. (c) The nominal 3 parameter fit (red) is compared against data with its fit quality uncertainty (dashes) and the alternative fit function uncertainty (dots). The relative uncertainty is shown in the lower panel.

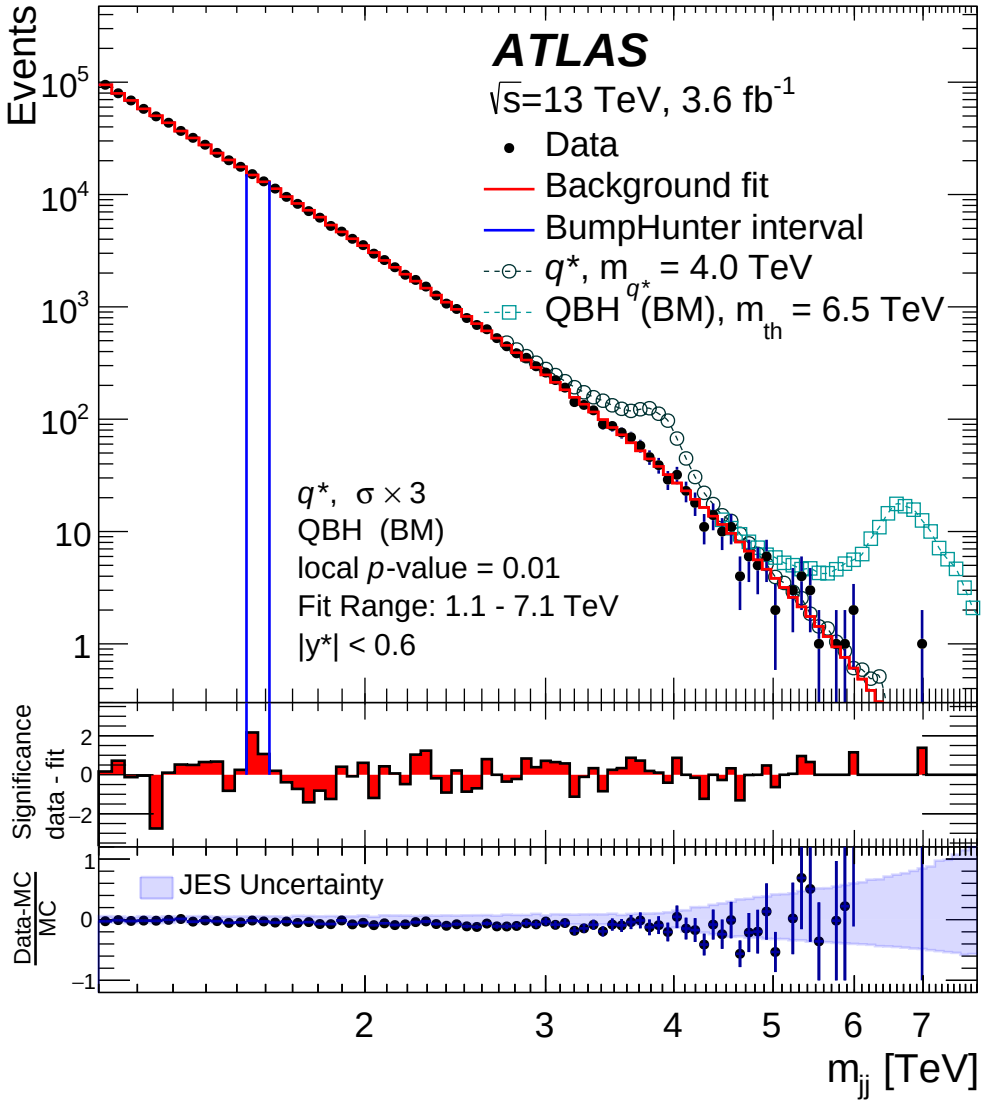

(a) Search Phase

Figure 8.4: The mass spectrum of the full 3.6 fb^{-1} dataset is shown alongside the best fit background estimation (red) and two signal models, a 4 TeV q^* resonance with σ scaled by a factor of three (open circles) and a 6.5 TeV BlackMax quantum black hole resonance (open squares). The most discrepant region found by BumpHunter is shown between two vertical blue bars with a local p-value of 0.01. The middle panel shows a bin-by-bin significance plot between the data and the fit, visually demonstrating the accuracy of the fit. Shown in the bottom panel is a data-MC comparison plot using next-to-leading-order (NLO) and electroweak corrected Pythia 8.1, demonstrating good agreement within JES uncertainties.

uncertainties. Good agreement is shown across the mass spectrum with no systematic differences observed. The lower panel of Figure 8.4 shows a comparison of the data to the leading order PYTHIA 8.1 MC simulation with corrections applied for NLO and electroweak effects. A small downward trend is seen across the mass spectrum but agrees within the JES uncertainties shown by the light blue band. The mass-dependent NLO corrections are derived by reweighting to the NLO predictions of NLOJet++ [130, 131]. The mass-dependent electroweak corrections are independently derived in Ref. [132]. Both corrections are nearly unity at low mass and increase to a few percent above 3.4 TeV.

The BUMPHUNTER results are shown for all mass windows in Figure 8.5(a). The local p-value of 0.01 is greatly reduced when including bins adjacent to the discrepant region. The BUMPHUNTER test statistic, a reinterpretation of the minimum local p-value according to Eq. 7.3, is shown in Figure 8.5(b) for data as a red arrow and for many Poisson-fluctuated pseudo-experiments as a black and blue spectrum. The BUMPHUNTER test statistic in data falls in the bulk of the pseudo-experiment spectrum, indicating that the most discrepant excess in data is no more discrepant than expected from Poisson fluctuations in a background-only hypothesis. The global p-value of the excess is found to be 0.67, with no evidence of a localized excess caused by BSM resonances.

8.3 Limit Setting

As no excesses are found in the mass distribution the limit setting is performed on the q^*, sequential SM W', quantum black hole, dark matter mediator Z', and generic Gaussian resonance models. Observed limits are calculated using the procedure outlined in Section 7.3. Expected limits represent the average limit from many pseudo-experiments assuming the background-only hypothesis is true. Uncertainty bands of 68% and 95% on the expected limits reflect the sensitivity to statistical fluctuations in the data. A theoretical cross section curve is derived for each BSM model reflecting possible cross sections and their dependence on mass.

The observed and expected limits for the q^* model are shown in Figure 8.6. Limits on $\sigma \times \mathcal{A} \times \mathrm{BR}$ are set between masses of 2 and 6.5 TeV, with the strongest limits set at higher masses. The observed limit intersects with the theoretical cross section curve at 5.2 TeV, presenting a 95% confidence-level lower bound on the mass of potential q^* resonances. The

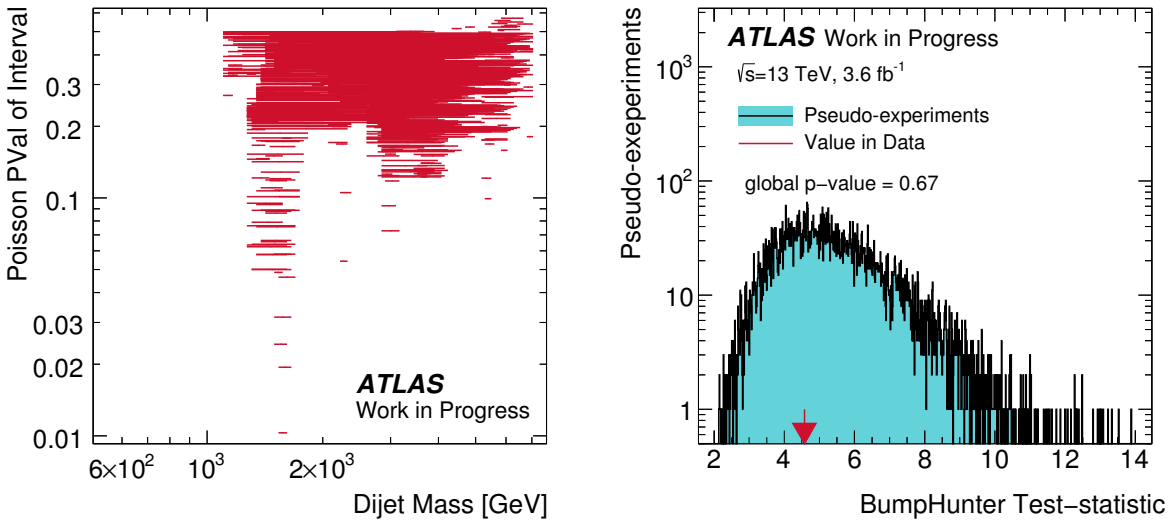

(a) P-value per range

(b) Test Statistic for Toys

Figure 8.5: Results of the BumpHunter search phase on the full 3.6 fb^{-1} dataset. (a) A comparison of local p-values for every mass window, with a minimum local p-value of 0.01 between 1.53 and 1.61 TeV. (b) The comparison of the BumpHunter test statistic in data (arrow) with pseudo-experiments (black and blue) gives a global p-value of 0.67, demonstrating compatibility of the data with the QCD background-only hypothesis.

observed limit is slightly stronger than the expected limit of 4.9 TeV.

The observed and expected limits for the sequential SM W' model are shown in Figure 8.7. Limits on $\sigma \times \mathcal{A} \times$BR are set between masses of 1 and 6.5 TeV, with the limit strengthening with mass up to 4.5 TeV. Limits are fairly flat after 4.5 TeV due to the lower mass tails caused by PDF effects, as explained in Section 4.2.2. The observed limit intersects with the theoretical cross section curve at 2.6 TeV, presenting a 95% confidence-level lower bound on the mass of potential W' resonances. The observed limit is identical to the expected limit.

The observed and expected limits for the various quantum black hole models are shown in Figure 8.8. Limits on $\sigma \times \mathcal{A}$ are set between masses of 4 and 9.5 TeV, with the strongest limits set at higher masses. For the QBH models the branching ratio to partons is dominant and assumed to be 1. Limits are fairly flat after the last data point at 6.8 TeV due to the predicted dominance of quantum black hole production after the production threshold mass. Limits are set at 8.1 TeV for the $n_{\text{dim}} = 6$ theory generated with BlackMax, at 8.3 TeV for the $n_{\text{dim}} = 6$ theory generated with QBH, and at 5.3 TeV for the $n_{\text{dim}} = 1$ theory generated with QBH. The observed limits are identical to the expected limits for the $n_{\text{dim}} = 6$ theory,

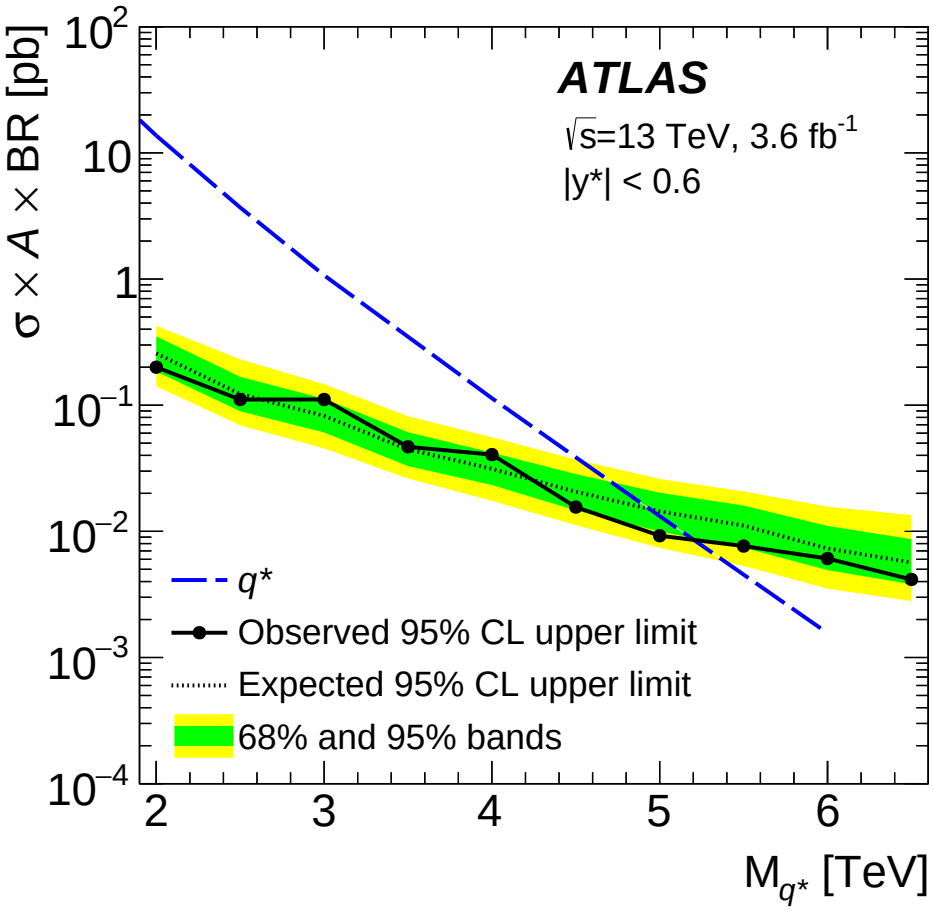

Figure 8.6: The 95% credibility-level upper limits on $\sigma \times \mathcal{A} \times$BR is shown as a function of mass for the q^* model. The observed limit (solid) intersects the theoretical cross section curve (dashed blue) at 5.2 TeV, presenting a lower limit on the mass of potential q^* resonances. The average expected limit (dotted) is shown with its 68% (dark green) and 95% (light yellow) uncertainty bands.

and slightly higher than the expected 5.1 TeV limit for the $n_{\text{dim}} = 1$ theory.

The observed and expected limits for the dark matter mediator Z' model is shown in Figure 8.6 for an assumed SM coupling of $g_q = 30\%$. Limits on $\sigma \times \mathcal{A} \times$BR are set between masses of 1.5 and 3.5 TeV, with the strongest limits set at higher masses. The observed limit intersects with the theoretical cross section curve at 2.6 TeV, presenting a 95% confidence-level lower bound on the mass of potential Z' resonances with $g_q = 30\%$. Cross section limits with respect to theory are also shown in Figure 8.10 for the Z' model as a function of both the dark matter mediator mass and the coupling to SM particles. Values below 1

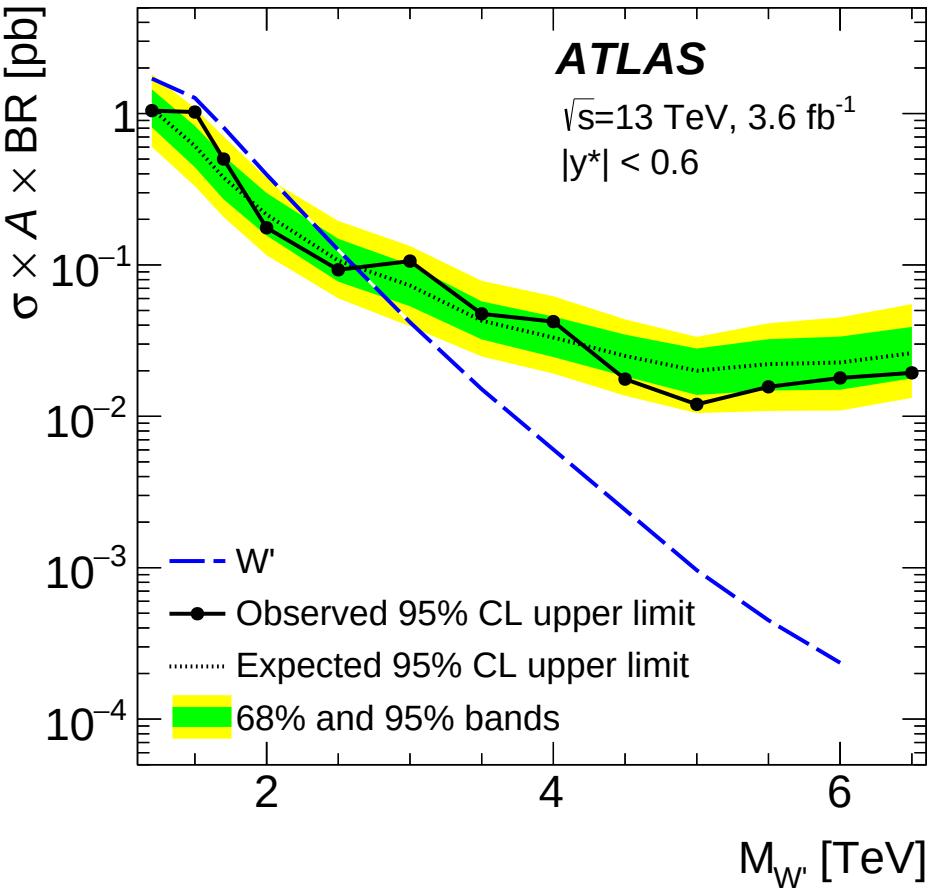

Figure 8.7: The 95% credibility-level upper limits on $\sigma \times \mathcal{A} \times$BR is shown as a function of mass for the sequential SM W'. The observed limit (solid) intersects the theoretical cross section curve (dashed blue) at 2.6 TeV, presenting a lower limit on the mass of potential W' resonances. The average expected limit (dotted) is shown with its 68% (dark green) and 95% (light yellow) uncertainty bands.

correspond to excluded regions. No signal samples were generated for regions in white which are implicitly excluded due to their lower mediator mass and larger couplings to the SM.

The expected and observed 95% credibility-level limits on mass for signal models are collected in Table 8.1, alongside the corresponding limits set at 8 TeV. Increases in the excluded masses with respect to 8 TeV vary between quantum black hole models and generators, with gains of up to 2.6 TeV. Improvements to q^* and sequential SM W' limits are 1.1 and 0.1 TeV, respectively. The large improvements in mass exclusion are derived with only 1/6th of the luminosity collected at 8 TeV during Run 1, demonstrating the large increase in sensitivity

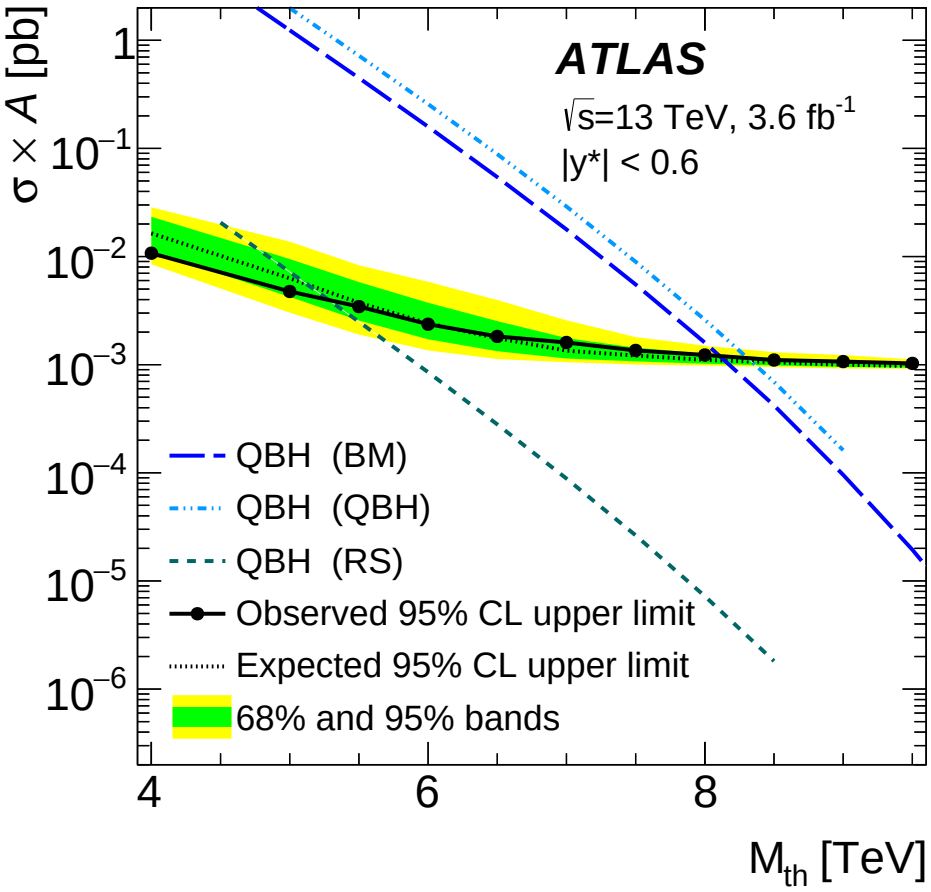

Figure 8.8: The 95% credibility-level upper limits on $\sigma \times \mathcal{A}$ is shown as a function of mass for quantum black holes. Theoretical cross section curves are provided for the $n_{\text{dim}} = 6$ theory generated with BlackMax (BM, dashes) and QBH (QBH, dot-dashes) as well as for the $n_{\text{dim}} = 1$ theory generated with QBH (RS, dots). The observed limit (solid) intersects the theoretical cross section curves at 8.1 (BM), 8.3 (QBH), and 5.3 (RS) TeV. The average expected limit (dotted) is shown with its 68% (dark green) and 95% (light yellow) uncertainty bands.

provided by the large increase in center-of-mass energy. The smaller gain in the W' limits is primarily due to the low mass tails arising from PDF effects, as detailed in Section 4.2.3.

Limits on $\sigma \times \mathcal{A} \times$BR are also shown for generic Gaussian resonances of widths equal to 7%, 10%, and 15% of the Gaussian mean as well as for a resonance with width equal to the detector resolution. Gaussian resonances provide useful limits that may be reinterpreted for any theoretical BSM model, as described in Section 7.3.3. Theoretical BSM signals must have an approximately Gaussian shape after event selections are applied and their distribution

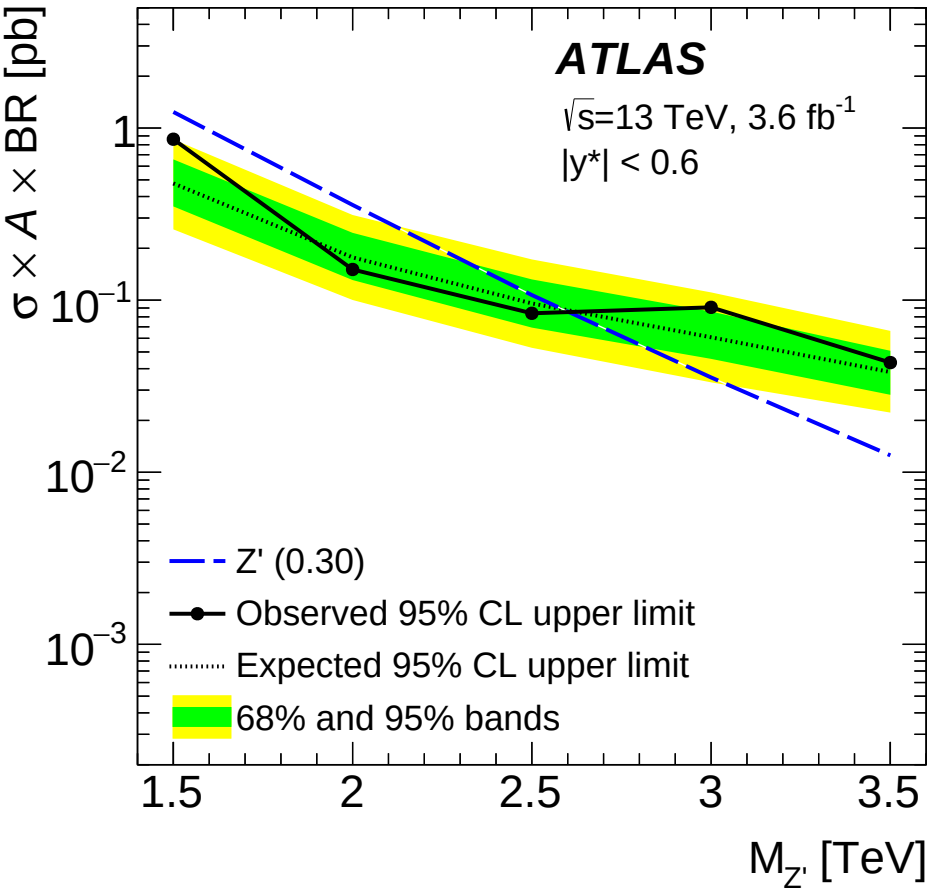

Figure 8.9: The 95% credibility-level upper limits on $\sigma \times \mathcal{A} \times$BR is shown as a function of mass for the dark matter mediator Z' model, assuming a SM coupling of $g_q = 30\%$. The observed limit (solid) intersects the theoretical cross section curve (dashed blue) at 2.6 TeV, presenting a lower limit on the mass of potential Z' resonances. The average expected limit (dotted) is shown with its 68% (dark green) and 95% (light yellow) uncertainty bands.

should be limited to masses within ∼20% of the mean. Signals with long tails should be avoided.

Gaussian limits are provided only when the mean of the Gaussian is at least two widths away from end points established at 1.1 and 6.9 TeV. Generic resonances are excluded below 2 TeV for cross sections of 50 to 300 fb^{-1} and below 4 TeV for cross sections of 2 to 20 fb^{-1}.

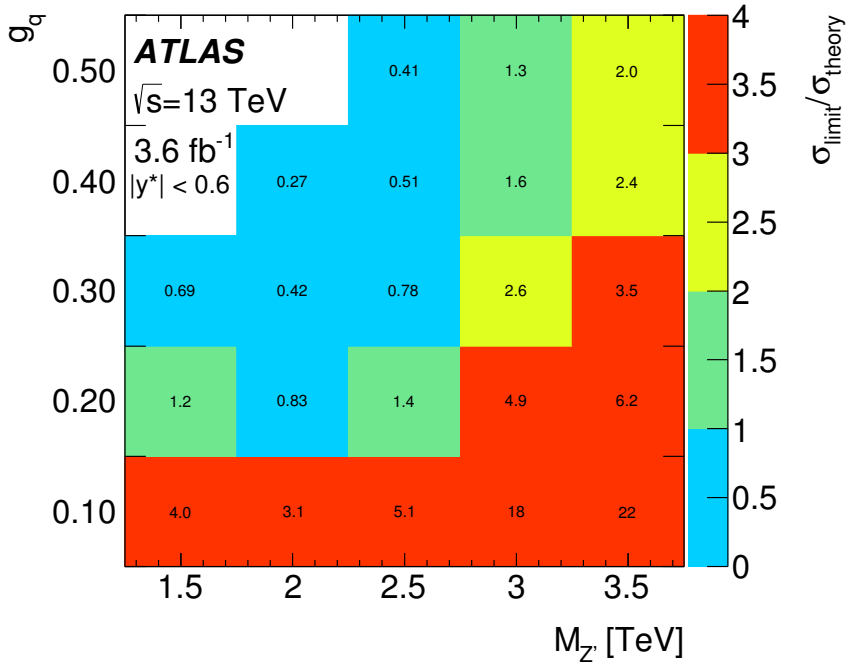

Figure 8.10: The ratio of the 95% credibility-level upper limits to the theoretical cross section is shown for the dark matter mediator Z' model as a function of the mediator mass $M_{Z'}$ and standard model coupling g_q. Mass-coupling points labelled as below 1 (light blue) are excluded. Limits are not calculated for signal points at low masses and large couplings which are implicitly excluded.

Model	95% Exclusion Limits		
	Run 1 Observed	Run 2 Observed	Run 2 Expected
Quantum black holes, $n_{\text{dim}} = 6$ (BLACKMAX generator)	5.6 TeV	8.1 TeV	8.1 TeV
Quantum black holes, $n_{\text{dim}} = 6$ (QBH generator)	5.7 TeV	8.3 TeV	8.3 TeV
Quantum black holes, $n_{\text{dim}} = 1$ (QBH generator)	-	5.3 TeV	5.1 TeV
Sequential SM W'	2.5 TeV	2.6 TeV	2.6 TeV
Excited quark q^*	4.1 TeV	5.2 TeV	4.9 TeV

Table 8.1: Lower limits on the mass of signal models derived from the intersection of the 95% credibility-level limits and the theoretical cross section curves. Expected and observed mass limits are shown for quantum black holes, sequential SM W', and q^* alongside the observed Run 1 limits, taken from [16].

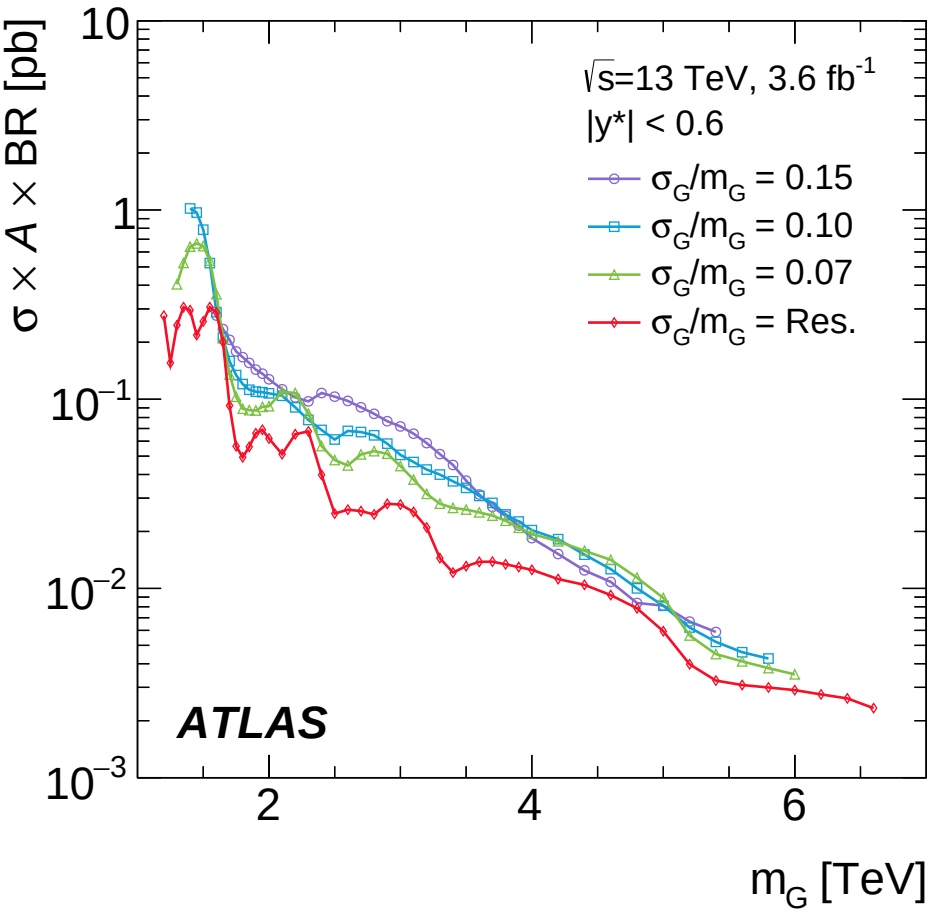

Figure 8.11: The 95% credibility-level upper limits on $\sigma \times \mathcal{A}\times$BR for generic Gaussian resonances of various widths. Widths of 7%, 10%, and 15% are calculated with respect to the mean Gaussian mass. The detector resolution width (Res.) varies from 3% at low mass to 2% at high mass, as determined in Figure 6.3.

8.4 Conclusion

The first 13 TeV dijet resonance search performed by the ATLAS experiment during Run 2 has found no evidence of new physics beyond the standard model. The QCD dijet system was explored for potential new s-channel resonances using both MC simulation and data-driven modeling. With only 3.6 fb^{-1} of data collected large improvements were made to the 95% credibility-level limits of well-known theoretical models. Model-independent limits were also derived assuming generic Gaussian resonances that allow limits to be recast for any theoretical signal model.

This analysis was the first ATLAS publication to utilize high-p_{T} jets at 13 TeV, exploring their reconstruction, calibration, and performance. New methods for jet cleaning and calibration were utilized by this analysis and novel validation techniques were developed that have since become standard in jet-based ATLAS analyses. This analysis has identified and studied the highest p_{T} dijet event yet observed by any collider experiment, as shown in Figures 8.1 and 8.2. New techniques for background estimation and validation were developed leading to large improvements in the fitting performance over previous analyses. Subsequent analyses which directly benefited from the work of this analysis include the strong-gravity multijet search [133], the low mass and high mass b-tagged dijet searches [134,135], the dijet with initial state radiation search [136], and the trigger level analysis [137].

Large increases in center-of-mass energies at hadron colliders will not be seen again for at least several decades. Nonetheless the ATLAS experiment and the LHC will continue to collect data at 13 and 14 TeV, providing a great potential for the discovery of any new physics with cross sections beyond the reach of this early analysis. Sensitivity studies produced in association with this analysis [138] have shown the discovery potential of the q^* model to increase roughly 1 TeV with 30 fb^{-1} and 2 TeV with 300 fb^{-1}. Whether new physics is discovered or the limits presented here are merely strengthened, future iterations will further our understanding of the standard model beyond the significant gains made by this analysis.

REFERENCES

[1] Lyndon Evans and Philip Bryant, LHC Machine, *JINST*, 3:S08001, 2008.

[2] **ATLAS** Collaboration, The ATLAS Experiment at the CERN Large Hadron Collider, *JINST*, 3:S08003, 2008.

[3] **ATLAS** Collaboration, Georges Aad et al., Search for new phenomena in dijet mass and angular distributions from pp collisions at $\sqrt{s} = 13$ TeV with the ATLAS detector, *Phys. Lett.*, B754:302–322, 2016.

[4] **UA1** Collaboration, G. Arnison et al., Angular Distributions and Structure Functions from Two Jet Events at the CERN SPS $p\bar{p}$ Collider, *Phys. Lett.*, B136:294, 1984.

[5] **UA1** Collaboration, C. Albajar et al., Two Jet Mass Distributions at the CERN Proton - Anti-Proton Collider, *Phys. Lett.*, B209:127–134, 1988.

[6] **UA2** Collaboration, P. Bagnaia et al., Measurement of jet production properties at the CERN $\overline{p}p$ collider, *Phys. Lett. B*, 144(CERN-EP-84-74):283–290. 19 p, Jun 1984.

[7] **CDF** Collaboration, T. Aaltonen et al., Search for new particles decaying into dijets in proton-antiproton collisions at $\sqrt{s} = 1.96$ TeV, *Phys. Rev.*, D79:112002, 2009.

[8] **D0** Collaboration, V. M. Abazov et al., Measurement of dijet angular distributions at $\sqrt{s} = 1.96$ TeV and searches for quark compositeness and extra spatial dimensions, *Phys. Rev. Lett.*, 103:191803, 2009.

[9] **ATLAS** Collaboration, G. Aad et al., Search for New Particles in Two-Jet Final States in 7 TeV Proton-Proton Collisions with the ATLAS Detector at the LHC, *Phys. Rev. Lett.*, 105:161801, 2010.

[10] **CMS** Collaboration, Vardan Khachatryan et al., Search for Dijet Resonances in 7 TeV pp Collisions at CMS, *Phys. Rev. Lett.*, 105:211801, 2010.

[11] **CMS** Collaboration, Vardan Khachatryan et al., Search for Quark Compositeness with the Dijet Centrality Ratio in pp Collisions at $\sqrt{s} = 7$ TeV, *Phys. Rev. Lett.*, 105:262001, 2010.

[12] **CMS** Collaboration, Serguei Chatrchyan et al., Search for Resonances in the Dijet Mass Spectrum from 7 TeV pp Collisions at CMS, *Phys. Lett.*, B704:123–142, 2011.

[13] **ATLAS** Collaboration, Georges Aad et al., Search for New Physics in Dijet Mass and Angular Distributions in pp Collisions at $\sqrt{s} = 7$ TeV Measured with the ATLAS Detector, *New J. Phys.*, 13:053044, 2011.

[14] **ATLAS** Collaboration, Georges Aad et al., Search for New Physics in the Dijet Mass Distribution using 1 fb^{-1} of pp Collision Data at $\sqrt{s}$ =7 TeV collected by the ATLAS Detector, *Phys. Lett.*, B708:37–54, 2012.

[15] **ATLAS** Collaboration, Georges Aad et al., ATLAS search for new phenomena in dijet mass and angular distributions using pp collisions at $\sqrt{s} = 7$ TeV, *JHEP*, 01:029, 2013.

[16] **ATLAS** Collaboration, Georges Aad et al., Search for new phenomena in the dijet mass distribution using pp collision data at $\sqrt{s} = 8$ TeV with the ATLAS detector, *Phys. Rev.*, D91(5):052007, 2015.

[17] **CMS** Collaboration, Serguei Chatrchyan et al., Search for narrow resonances using the dijet mass spectrum in pp collisions at $\sqrt{s} = 8$ TeV, *Phys. Rev.*, D87(11):114015, 2013.

[18] Andrew Purcell, Go on a quest at the first particle cern webfest, (BUL-NA-2012-269. 35/2012):10, Aug 2012.

[19] Stefan Hoche, Introduction to parton-shower event generators, In *Theoretical Advanced Study Institute in Elementary Particle Physics: Journeys Through the Precision Frontier: Amplitudes for Colliders (TASI 2014) Boulder, Colorado, June 2-27, 2014*, 2014.

[20] J C Collins and D E Soper, The theorems of perturbative QCD, *Annual Review of Nuclear and Particle Science*, 37(1):383–409, 1987.

[21] Guido Altarelli and G. Parisi, Asymptotic Freedom in Parton Language, *Nucl. Phys.*, B126:298–318, 1977.

[22] Richard D. Ball et al., Parton distributions with LHC data, *Nucl. Phys.*, B867:244–289, 2013.

[23] Stefano Carrazza, Stefano Forte, and Juan Rojo, Parton Distributions and Event Generators, In *Proceedings, 43rd International Symposium on Multiparticle Dynamics (ISMD 13)*, pages 89–96, 2013.

[24] B. R. Webber, Fragmentation and hadronization, *Int. J. Mod. Phys.*, A15S1:577–606, 2000.

[25] Bo Andersson, G. Gustafson, G. Ingelman, and T. Sjostrand, Parton Fragmentation and String Dynamics, *Phys. Rept.*, 97:31–145, 1983.

[26] T. S. van Albada, J. N. Bahcall, K. Begeman, and R. Sancisi, Distribution of dark matter in the spiral galaxy NGC 3198, *ApJ*, 295:305–313, August 1985.

[27] N. Kaiser and G. Squires, Mapping the dark matter with weak gravitational lensing, *ApJ*, 404:441–450, February 1993.

[28] **Planck** Collaboration, R. Adam et al., Planck 2015 results. I. Overview of products and scientific results, 2015.

[29] Daniel Abercrombie et al., Dark Matter Benchmark Models for Early LHC Run-2 Searches: Report of the ATLAS/CMS Dark Matter Forum, 2015.

[30] Nima Arkani-Hamed, Savas Dimopoulos, and G. R. Dvali, The Hierarchy problem and new dimensions at a millimeter, *Phys. Lett.*, B429:263–272, 1998.

[31] Lisa Randall and Raman Sundrum, A Large mass hierarchy from a small extra dimension, *Phys. Rev. Lett.*, 83:3370–3373, 1999.

[32] G. Arnison et al., Experimental observation of isolated large transverse energy electrons with associated missing energy at $s = 540$ GeV, *Physics Letters B*, 122(1):103 – 116, 1983.

[33] M. Banner et al., Observation of single isolated electrons of high transverse momentum in events with missing transverse energy at the cern *pp* collider, *Physics Letters B*, 122(5 - 6):476 – 485, 1983.

[34] G. Arnison et al., Experimental observation of lepton pairs of invariant mass around 95 GeV/c^2 at the cern sps collider, *Physics Letters B*, 126(5):398 – 410, 1983.

[35] P. Bagnaia et al., Evidence for Z0$\rightarrow e^+e^-$ at the cern *pp* collider, *Physics Letters B*, 129(1):130 – 140, 1983.

[36] Guido Altarelli, B. Mele, and M. Ruiz-Altaba, Searching for New Heavy Vector Bosons in $p\bar{p}$ Colliders, *Z. Phys.*, C45:109, 1989, [Erratum: Z. Phys.C47,676(1990)].

[37] U. Baur, M. Spira, and P. M. Zerwas, Excited quark and lepton production at hadron colliders, *Phys. Rev.*, D42:815–825, 1990.

[38] *LEP design report*, CERN, Geneva, 1984, Copies shelved as reports in LEP, PS and SPS libraries.

[39] **ALICE** Collaboration, The ALICE experiment at the CERN LHC, *JINST*, 3:S08002, 2008.

[40] **CMS** Collaboration, The CMS experiment at the CERN LHC, *JINST*, 3:S08004, 2008.

[41] **LHCb** Collaboration, The LHCb detector at the LHC, *JINST*, 3:S08005, 2008.

[42] Fabienne Marcastel, CERN's Accelerator Complex. La chaine des accelerateurs du CERN, (OPEN-PHO-CHART-2013-001), Oct 2013, General Photo, https://cds.cern.ch/record/1621583.

[43] **ATLAS** Collaboration, Morad Aaboud et al., Luminosity determination in *pp* collisions at $\sqrt{s} = 8$ TeV using the ATLAS detector at the LHC, 2016.

[44] **ATLAS** Collaboration, Nitesh Soni, ATLAS Forward Detectors and Physics, In *Lake Louise Winter Institute: Celebrating 25 years (LLWI 2010) Lake Louise, Alberta, Canada, February 15-20, 2010*, 2010.

[45] **CMS Collaboration** Collaboration, CMS Luminosity Measurement for the 2015 Data Taking Period, Technical Report CMS-PAS-LUM-15-001, CERN, Geneva, 2016.

[46] Werner Herr and B Muratori, Concept of luminosity, 2006, https://cds.cern.ch/record/941318.

[47] **ATLAS** Collaboration, Track Reconstruction Performance of the ATLAS Inner Detector at $\sqrt{s} = 13$ TeV, Technical Report ATL-PHYS-PUB-2015-018, CERN, Geneva, Jul 2015.

[48] **ATLAS** Collaboration, Alignment of the ATLAS Inner Detector and its Performance in 2012, Technical Report ATLAS-CONF-2014-047, CERN, Geneva, Jul 2014.

[49] M Capeans, G Darbo, K Einsweiller, M Elsing, T Flick, M Garcia-Sciveres, C Gemme, H Pernegger, O Rohne, and R Vuillermet, ATLAS Insertable B-Layer Technical Design Report, Technical Report CERN-LHCC-2010-013. ATLAS-TDR-19, CERN, Geneva, 2010.

[50] G. Aad et al., Charged-particle distributions in pp interactions measured with the ATLAS detector at the LHC, *Physics Letters B*, 758:67 – 88, 2016.

[51] Commissioning of the ATLAS b-tagging algorithms using $t\bar{t}$ events in early Run-2 data, Technical Report ATL-PHYS-PUB-2015-039, CERN, Geneva, Aug 2015.

[52] Bartosz Mindur, ATLAS Transition Radiation Tracker (TRT): Straw Tubes for Tracking and Particle Identification at the Large Hadron Collider, Technical Report ATL-INDET-PROC-2016-001, CERN, Geneva, Mar 2016.

[53] **ATLAS** Collaboration, G. Aad et al., The ATLAS Inner Detector commissioning and calibration, *Eur. Phys. J.*, C70:787–821, 2010.

[54] Glenn F Knoll, *Radiation detection and measurement; 4th ed.*, Wiley, New York, NY, 2010.

[55] W. E. Cleland and E. G. Stern, Signal processing considerations for liquid ionization calorimeters in a high rate environment, *Nucl. Instrum. Meth.*, A338(2-3):467–497, 1994.

[56] H. Abreu et al., Performance of the electronic readout of the atlas liquid argon calorimeters, *Journal of Instrumentation*, 5(09):P09003, 2010.

[57] **ATLAS Tile Calorimeter** Collaboration, Giulio Usai, Signal reconstruction of the ATLAS Hadronic Tile Calorimeter: implementation and performance, *J. Phys. Conf. Ser.*, 293:012056, 2011.

[58] P. Adragna et al., Testbeam studies of production modules of the ATLAS tile calorimeter, *Nuclear Instruments and Methods in Physics Research Section A: Accelerators, Spectrometers, Detectors and Associated Equipment*, 606(3):362 – 394, 2009.

[59] A. Artamonov et al., The ATLAS forward calorimeters, *JINST*, 3:P02010, 2008.

[60] F. Bauer et al., Construction and test of MDT chambers for the ATLAS muon spectrometer, *Nucl. Instrum. Meth.*, A461:17–20, 2001.

[61] Theodoros Argyropoulos et al., Cathode strip chambers in ATLAS: Installation, commissioning and in situ performance, *IEEE Trans. Nucl. Sci.*, 56:1568–1574, 2009.

[62] G. Aielli et al., The RPC first level muon trigger in the barrel of the ATLAS experiment, *Nucl. Phys. Proc. Suppl.*, 158:11–15, 2006.

[63] S. Majewski, Georges Charpak, A. Breskin, and G. Mikenberg, A thin multiwire chamber operating in the high multiplication mode, *Nucl. Instrum. Meth.*, 217:265–271, 1983.

[64] **ATLAS** Collaboration, Georges Aad et al., Muon reconstruction efficiency and momentum resolution of the ATLAS experiment in proton-proton collisions at $\sqrt{s} = 7$ TeV in 2010, *Eur. Phys. J.*, C74(9):3034, 2014.

[65] S. Artz et al., Upgrade of the ATLAS central trigger for LHC run-2, *Journal of Instrumentation*, 10(02):C02030, 2015.

[66] Carlo Schiavi, ATLAS High-Level Trigger algorithms for Run-2 data-taking, Technical Report ATL-DAQ-PROC-2015-018, CERN, Geneva, May 2015, Not published in the proceedings.

[67] **ATLAS** Collaboration, *ATLAS Computing: technical design report*, Technical Design Report ATLAS. CERN, Geneva, 2005.

[68] **ATLAS** Collaboration, G. Aad et al., Measurement of the inclusive jet cross-section in proton-proton collisions at $\sqrt{s} = 13$ tev using 4.5 fb^1 of data with the ATLAS detector, *JHEP*, 2015(2):1–54, 2015.

[69] Torbjorn Sjostrand, Stephen Mrenna, and Peter Z. Skands, A Brief Introduction to PYTHIA 8.1, *Comput. Phys. Commun.*, 178:852–867, 2008.

[70] Guido Altarelli and G. Parisi, Asymptotic Freedom in Parton Language, *Nucl. Phys.*, B126:298–318, 1977.

[71] **ATLAS** Collaboration, ATLAS Run 1 Pythia8 tunes, Technical Report ATL-PHYS-PUB-2014-021, CERN, Geneva, Nov 2014.

[72] S. Agostinelli et al., Geant4 a simulation toolkit, *Nuclear Instruments and Methods in Physics Research Section A: Accelerators, Spectrometers, Detectors and Associated Equipment*, 506(3):250 – 303, 2003.

[73] J. Allison et al., Geant4 developments and applications, *IEEE Transactions on Nuclear Science*, 53(1):270–278, Feb 2006.

[74] **ATLAS** Collaboration, Georges Aad et al., A study of the material in the ATLAS inner detector using secondary hadronic interactions, *JINST*, 7:P01013, 2012.

[75] J. Jim Pena, Alignment of the ATLAS Inner Detector Upgraded for the LHC Run II, *J. Phys. Conf. Ser.*, 664(7):072025, 2015.

[76] **ATLAS** Collaboration, G. Aad et al., Commissioning of the ATLAS muon spectrometer with cosmic rays, *The European Physical Journal C*, 70(3):875–916, 2010.

[77] **ATLAS** Collaboration, G. Aad et al., The ATLAS Simulation Infrastructure, *Eur. Phys. J.*, C70:823–874, 2010.

[78] **ATLAS** Collaboration, Zach Marshall, Re-re-defining the Standard QCD Di-Jet Samples: Beginning to like event weights, Technical Report ATL-COM-PHYS-2015-417, CERN, Geneva, May 2015.

[79] Daniel Abercrombie et al., Dark Matter Benchmark Models for Early LHC Run-2 Searches: Report of the ATLAS/CMS Dark Matter Forum, 2015.

[80] Mikael Chala, Felix Kahlhoefer, Matthew McCullough, Germano Nardini, and Kai Schmidt-Hoberg, Constraining Dark Sectors with Monojets and Dijets, *JHEP*, 07:089, 2015.

[81] **ATLAS** Collaboration, Georges Aad et al., Search for high-mass diboson resonances with boson-tagged jets in proton-proton collisions at $\sqrt{s} = 8$ tev with the ATLAS detector, *JHEP*, 12:055, 2015.

[82] De-Chang Dai, Glenn Starkman, Dejan Stojkovic, Cigdem Issever, Eram Rizvi, and Jeff Tseng, BlackMax: a black-hole event generator with rotation, recoil, split branes, and brane tension, *Phys. Rev.*, D77:076007, 2008.

[83] Hung-Liang Lai, Marco Guzzi, Joey Huston, Zhao Li, Pavel M. Nadolsky, Jon Pumplin, and C. P. Yuan, New parton distributions for collider physics, *Phys. Rev.*, D82:074024, 2010.

[84] Douglas M. Gingrich, Quantum black holes with charge, colour, and spin at the LHC, *J. Phys.*, G37:105008, 2010.

[85] A. D. Martin, W. J. Stirling, R. S. Thorne, and G. Watt, Parton distributions for the LHC, *Eur. Phys. J.*, C63:189–285, 2009.

[86] **ATLAS** Collaboration, A. Ashkenazi et al., ATLAS search in 2012 data for new phenomena in dijet mass distributions using pp collisions at $\sqrt{s} = 8$ TeV, Technical Report ATL-COM-PHYS-2013-1518, CERN, Geneva, Nov 2013.

[87] Michiel Botje et al., The PDF4LHC Working Group Interim Recommendations, 2011.

[88] ATLAS Luminosity Group, Luminosity for physics, July 2015, https://twiki.cern.ch/twiki/bin/view/Atlas/LuminosityForPhysics.

[89] Gerald C. Blazey et al., Run II jet physics, In *QCD and weak boson physics in Run II. Proceedings, Batavia, USA, March 4-6, June 3-4, November 4-6, 1999*, pages 47–77, 2000.

[90] **ATLAS** Collaboration, ATLAS Collaboration, Topological cell clustering in the ATLAS calorimeters and its performance in LHC Run 1, Technical Report CERN-PH-EP-2015-304, CERN, Geneva, Mar 2016.

[91] Matteo Cacciari, Gavin P. Salam, and Gregory Soyez, The Anti-k(t) jet clustering algorithm, *JHEP*, 04:063, 2008.

[92] **ATLAS** Collaboration, Jet Calibration and Systematic Uncertainties for Jets Reconstructed in the ATLAS Detector at $\sqrt{s} = 13$ TeV, Technical Report ATL-PHYS-PUB-2015-015, CERN, Geneva, Jul 2015.

[93] **ATLAS** Collaboration, Georges Aad et al., Jet energy measurement and its systematic uncertainty in proton-proton collisions at $\sqrt{s} = 7$ TeV with the ATLAS detector, *Eur. Phys. J.*, C75:17, 2015.

[94] **ATLAS** Collaboration, Pile-up subtraction and suppression for jets in ATLAS, Technical Report ATLAS-CONF-2013-083, CERN, Geneva, Aug 2013.

[95] **ATLAS** Collaboration, Jet global sequential corrections with the ATLAS detector in proton-proton collisions at $\sqrt{s} = 8$ TeV, Technical Report ATLAS-CONF-2015-002, CERN, Geneva, Mar 2015.

[96] **ATLAS** Collaboration, Data-driven determination of the energy scale and resolution of jets reconstructed in the ATLAS calorimeters using dijet and multijet events at $\sqrt{s} = 8$ TeV, Technical Report ATLAS-CONF-2015-017, CERN, Geneva, Apr 2015.

[97] **ATLAS** Collaboration, Determination of the jet energy scale and resolution at ATLAS using Z/γ–jet events in data at $\sqrt{s} = 8$ TeV, Technical Report ATLAS-CONF-2015-057, CERN, Geneva, Oct 2015.

[98] **ATLAS** Collaboration, A measurement of single hadron response using data at $\sqrt{s} =$ 8 TeV with the ATLAS detector, Technical Report ATL-PHYS-PUB-2014-002, CERN, Geneva, Mar 2014.

[99] **ATLAS** Collaboration, Georges Aad et al., Single hadron response measurement and calorimeter jet energy scale uncertainty with the ATLAS detector at the LHC, *Eur. Phys. J.*, C73(3):2305, 2013.

[100] **ATLAS Collaboration** Collaboration, Morad Aaboud et al., A measurement of the calorimeter response to single hadrons and determination of the jet energy scale

uncertainty using LHC Run-1 *pp*-collision data with the ATLAS detector, Technical Report CERN-EP-2016-149. arXiv:1607.08842, CERN, Geneva, Jul 2016.

[101] A. Ribon et al., Status of Geant4 hadronic physics for the simulation of LHC experiments at the start of LHC physics program, Technical Report CERN-LCGAPP-2010-02, 2010.

[102] **ATLAS** Collaboration, Monte Carlo Calibration and Combination of In-situ Measurements of Jet Energy Scale, Jet Energy Resolution and Jet Mass in ATLAS, Technical Report ATLAS-CONF-2015-037, CERN, Geneva, Aug 2015.

[103] **ATLAS** Collaboration, A method for the construction of strongly reduced representations of ATLAS experimental uncertainties and the application thereof to the jet energy scale, Technical Report ATL-PHYS-PUB-2015-014, CERN, Geneva, Jul 2015.

[104] **ATLAS** Collaboration, Selection of jets produced in 13 TeV proton-proton collisions with the ATLAS detector, Technical Report ATLAS-CONF-2015-029, CERN, Geneva, Jul 2015.

[105] **ATLAS** Collaboration, Georges Aad et al., Monitoring and data quality assessment of the ATLAS liquid argon calorimeter, *JINST*, 9:P07024, 2014.

[106] Robert M. Harris and Konstantinos Kousouris, Searches for dijet resonances at hadron colliders, *International Journal of Modern Physics A*, 26(30n31):5005–5055, 2011.

[107] **ATLAS** Collaboration, Lydia Beresford, Jeffrey Rogers Dandoy, Gabriel John Facini, Meghan Frate, Kevin Hildebrand, David Miller, Mats Joakim Robert Olsson, Mark Oreglia, Jiahang Zhong, Brian Lee Clark, and Brian Tuan, Properties of Jets and Inputs to Jet Reconstruction and Calibration with the ATLAS Detector Using Proton-Proton Collisions at $\sqrt{s} = 13$ TeV, Technical Report ATL-PHYS-PUB-2015-036, CERN, Geneva, Aug 2015.

[108] **ATLAS** Collaboration, Tagging and suppression of pileup jets with the ATLAS detector, Technical Report ATLAS-CONF-2014-018, CERN, Geneva, May 2014.

[109] W. T. Eadie et al., *Statistical Methods in Experimental Physics*, pages 269–270, North-Holland Pub. Co., 1971.

[110] J. Garvey et al., The ATLAS level-1 calorimeter trigger architecture, *IEEE Transactions on Nuclear Science*, 51(3):356–360, June 2004.

[111] **ATLAS** Collaboration, Measurement of the inclusive-jet cross section in proton-proton collisions at 13 TeV centre-of-mass energy with the ATLAS detector, Technical Report ATLAS-CONF-2015-034, CERN, Geneva, Jul 2015.

[112] G. Cowan, *Statistical Data Analysis*, Oxford science publications. Clarendon Press, 1998.

[113] Karl Pearson, On the criterion that a given system of deviations from the probable in the case of a correlated system of variables is such that it can be reasonably supposed to have arisen from random sampling, *Philosophical Magazine Series 5*, 50(302):157–175, 1900.

[114] R. A. Fisher, On the Mathematical Foundations of Theoretical Statistics, *Philosophical Transactions of the Royal Society of London Series A*, 222:309–368, 1922.

[115] Joel Heinrich, Pitfalls of Goodness-of-Fit from Likelihood, *eConf*, C030908:MOCT001, 2003, [,52(2003)].

[116] F. James and M. Roos, Minuit: A System for Function Minimization and Analysis of the Parameter Errors and Correlations, *Comput. Phys. Commun.*, 10:343–367, 1975.

[117] **CDF** Collaboration, F. Abe et al., Search for new particles decaying to dijets in $p\bar{p}$ collisions at $\sqrt{s} = 1.8$ TeV, *Phys. Rev. Lett.*, 74:3538–3543, May 1995.

[118] J. Alitti et al., A measurement of two-jet decays of the W and Z bosons at the CERN $p\bar{p}$ collider, *Zeitschrift für Physik C Particles and Fields*, 49(1):17–28, 1991.

[119] **CDF** Collaboration, F. Abe et al., Search for new particles decaying to dijets at CDF, *Phys. Rev.*, D55:5263–5268, 1997.

[120] **ATLAS** Collaboration, Georges Aad et al., Search for microscopic black holes and string balls in final states with leptons and jets with the ATLAS detector at $\sqrt{s} = 8$ TeV, *JHEP*, 2014(8):1–48, 2014.

[121] S. S. Wilks, The Large-Sample Distribution of the Likelihood Ratio for Testing Composite Hypotheses, *Annals Math. Statist.*, 9(1):60–62, 1938.

[122] A. Wald, Sequential tests of statistical hypotheses, *The Annals of Mathematical Statistics*, 16(2):117–186, 1945.

[123] George W. Snedcor, Calculation and interpretation of analysis of variance and covariance, *Ames, Ia: Collegiate Press*, 1934.

[124] G. Choudalakis, On hypothesis testing, trials factor, hypertests and the BumpHunter, 2011.

[125] Eilam Gross and Ofer Vitells, Trial factors or the look elsewhere effect in high energy physics, *Eur. Phys. J.*, C70:525–530, 2010.

[126] B.P. Carlin and T.A. Louis, *Bayesian Methods for Data Analysis, Third Edition*, Chapman & Hall/CRC Texts in Statistical Science. CRC Press, 2008.

[127] J. Heinrich, C. Blocker, J. Conway, L. Demortier, L. Lyons, G. Punzi, and P. K. Sinervo, Interval estimation in the presence of nuisance parameters. 1. Bayesian approach, *ArXiv Physics e-prints, physics/0409129*, September 2004.

[128] A. Caldwell, D. Kollár, and K. Kröninger, BAT - The Bayesian analysis toolkit, *Computer Physics Communications*, 180:2197–2209, November 2009.

[129] S. Ulam Nicholas Metropolis, The monte carlo method, *Journal of the American Statistical Association*, 44(247):335–341, 1949.

[130] Zoltan Nagy, Next-to-leading order calculation of three jet observables in hadron hadron collision, *Phys. Rev.*, D68:094002, 2003.

[131] S. Catani and M. H. Seymour, A General algorithm for calculating jet cross-sections in NLO QCD, *Nucl. Phys.*, B485:291–419, 1997, [Erratum: Nucl. Phys.B510,503(1998)].

[132] Stefan Dittmaier, Alexander Huss, and Christian Speckner, Weak radiative corrections to dijet production at hadron colliders, *JHEP*, 11:095, 2012.

[133] **ATLAS** Collaboration, Georges Aad et al., Search for strong gravity in multijet final states produced in pp collisions at $\sqrt{s} = 13$ TeV using the ATLAS detector at the LHC, *JHEP*, 03:026, 2016.

[134] **ATLAS** Collaboration, Search for resonances below 1.2 TeV from the mass distribution of b-jet pairs in proton-proton collisions at $\sqrt{s} = 13$ TeV with the ATLAS detector, Technical Report ATLAS-CONF-2016-031, CERN, Geneva, Jun 2016.

[135] **ATLAS** Collaboration, Morad Aaboud et al., Search for resonances in the mass distribution of jet pairs with one or two jets identified as b-jets in proton–proton collisions at $\sqrt{s} = 13$ TeV with the ATLAS detector, *Phys. Lett.*, B759:229–246, 2016.

[136] **ATLAS** Collaboration, Search for new light resonances decaying to jet pairs and produced in association with a photon in proton-proton collisions at $\sqrt{s} = 13$ TeV with the ATLAS detector, Technical Report ATLAS-CONF-2016-029, CERN, Geneva, Jun 2016.

[137] **ATLAS** Collaboration, Search for light dijet resonances with the ATLAS detector using a Trigger-Level Analysis in LHC pp collisions at $\sqrt{s} = 13$ TeV, Technical Report ATLAS-CONF-2016-030, CERN, Geneva, Jun 2016.

[138] **ATLAS** Collaboration, Dijet resonance searches with the ATLAS detector at 14 TeV LHC, Technical Report ATL-PHYS-PUB-2015-004, CERN, Geneva, Mar 2015.